Master's thesis

NTNU
Norwegian University of Science and Technology
Faculty of Engineering
Department of Structural Engineering

Håvard Hatling Anfinsen
Mads Kristoffer Waaler

Estimation of Fatigue Damage due to Buffeting of Suspension Bridges

Closed-Form Methods, Rainflow Algorithm and Gaussian Process Regression

Master's thesis in ICT, Civil and Environmental Engineering
Supervisor: Ole Andre Øiseth
Co-supervisor: Aksel Fenerci, Tor Martin Lystad
June 2021

NTNU
Kunnskap for en bedre verden

Håvard Hatling Anfinsen
Mads Kristoffer Waaler

Estimation of Fatigue Damage due to Buffeting of Suspension Bridges

Closed-Form Methods, Rainflow Algorithm and Gaussian Process Regression

Master's thesis in ICT, Civil and Environmental Engineering
Supervisor: Ole Andre Øiseth
Co-supervisor: Aksel Fenerci, Tor Martin Lystad
June 2021

Norwegian University of Science and Technology
Faculty of Engineering
Department of Structural Engineering

NTNU
Norwegian University of
Science and Technology

Department of Structural Engineering
Faculty of Engineering
NTNU – Norwegian University of Science and Technology

ACCESSIBILITY

OPEN

MASTER THESIS 2021

SUBJECT AREA:	DATE:	NO. OF PAGES:
Structural dynamics	10.06.2021	107 (18+80+9)

TITLE:

Estimation of Fatigue Damage due to Buffeting of Suspension Bridges
Closed-Form Methods, Rainflow Algorithm and Gaussian Process Regression

Estimering av utmattingsskade på grunn av buffeting av hengebruer
Lukket-form metoder, rainflow algoritme og Gaussisk prosess regresjon

BY:

Håvard Hatling Anfinsen
Mads Kristoffer Waaler

SUMMARY:
This thesis includes a comparison of methods for calculating the fatigue damage from buffeting response on simple shear frames and the planned Langenuen bridge. The primary goal of the thesis is to evaluate the accuracy of closed-form methods in the frequency domain against the widely accepted rainflow method in the time domain. The fatigue damages were calculated by creating surrogate models with a sequential updating process using Gaussian process regression. The Dirlik method along with the method proposed by Tovo and Benasciutti proved to give the most consistent estimations overall. However, due to the unpredictable non-conservative results, they should be used with care.

RESPONSIBLE TEACHER: Professor Ole Andre Øiseth

SUPERVISORS: Professor Ole Andre Øiseth, Researchers Aksel Fenerci and Tor Martin Lystad

CARRIED OUT AT: Department of Structural Engineering, NTNU

Abstract

Several closed-form methods for calculating accumulated fatigue damage have been proposed in the last 50 years. The primary goal in this thesis is to compare some popular closed-form methods to the rainflow counting algorithm combined with Miner's rule. The methods were tested on realistic stress spectrums generated by buffeting wind loading. A theoretical foundation is presented for stochastic processes, Gaussian process regression and fatigue damage accumulation. The comparisons were performed on multi-degree of freedom systems presented as shear frames in steel and a model of the planned Langenuen bridge in aluminum. Both models were exposed to buffeting wind loading represented by a joint probability distribution between the mean wind velocity and the standard deviation of the turbulence along-wind. Surrogate models were created using an updating approach where points were sequentially added to the training data set. Finally, a numerical integration of the surrogate models was performed to find the rate of fatigue damage accumulation for each method, which is the foundation for the comparison.

Three different models of the shear frame were analyzed with one, three and five degrees of freedom as a proof of concept for the procedure to estimate fatigue damage. The models were studied both with and without background response to make further alterations to the stress spectrums. In addition, the methods were applied to four different linear SN-curves to compare the sensitivity towards the slopes. The relative error was found to increase for all methods with larger m-values or a more gentle slope of the SN-curve. Results showed that the closed-form methods proposed by Dirlik along with Tovo and Benasciutti gave the best estimations for the shear frame models with relative errors around $5-35\%$, depending on the type of stress spectrum. When the background response was excluded from the stress spectrums, several methods gave non-conservative results. The single-moment method often gave a low relative error but showed a pattern of non-conservativity for increased bandwidth of the stress spectrum.

For the Langenuen bridge, the displacement and force modes were extracted from an Abaqus model. A comparison of the closed-form methods was performed on stress spectrums from two cross section details obtained from nine sections along the span of the bridge. Non-conservativity was observed for all methods except for the narrow band method and the method proposed by Jiao and Moan, which presented conservative estimations with high relative error. The single-moment method gave the most non-conservative results with underestimations up to 30%. The method proposed by Dirlik in addition to the method proposed by Tovo and Benasciutti gave a relative error of around 10% at the Langenuen bridge. They proved to give the most consistent estimations overall on the stress spectrums analyzed in this thesis. They should, however, be used with care due to their unpredictable non-conservative estimations.

Sammendrag

I løpet av de siste 50 årene har mange frekvensbaserte metoder for å estimere utmattingsskader blitt presentert. Hovedmålet med denne avhandlingen er å sammenligne noen av de mest populære frekvensbaserte metodene mot rainflow-telling kombinert med den lineære Miners regel. Metodene er testet på realistiske spenningsspektre generert fra vindlaster. Et teoretisk grunnlag presenteres for stokastiske prosesser, Gaussisk prosess regresjon samt utmattingsanalyse. Sammenligningene ble utført på et flerfrihetsgradsystem i form av en skjærramme i stål og en modell av den planlagte Langenuen bru i aluminium. Begge modellene ble utsatt for vindlaster beskrevet gjennom en simultanfordeling mellom middelvindhastighet og standardavviket til turbulensen i vindretningen. Surrogatmodellene ble generert gjennom en oppdateringsprosess hvor punkter ble sekvensielt lagt til i treningsdataen. Til slutt utføres en numerisk integrasjon av surrogatmodellene for å finne utviklingen til utmattingsskaden, som danner grunnlaget for sammenligningen.

Tre ulike modeller av skjærrammen ble analysert med en, tre og fem frihetsgrader. Modellene ble analysert med og uten bakgrunnsrespons for å gi ytterligere variasjoner i spenningsspektrene. I tillegg ble metodene testet på fire ulike SN-kurver for å sammenligne sensitiviteten i forhold til stigningstallet på kurvene. Den relative feilen økte i takt med slakere SN-kurver for alle metoder. Metodene presentert av Dirlik samt Tovo og Benasciutti oppnådde best resultater for skjærrammene med relativ feil mellom 5−35% avhengig av type spenningsspekter. Da bakgrunnsresponsen ble ekskludert i spenningsspektrene estimerte flere metoder ikke-konservative resultater. Single-moment metoden gav generelt lav relativ feil, men viste et tydelig mønster med å produsere ikke-konservative resultater for økt båndbredde.

Forskyvnings og kraftmodene til Langenuen bru ble hentet ut fra en modell i Abaqus. De ulike frekvensbaserte metodene ble testet på spenningsspektre fra to tverrsnittsdetaljer over ni ulike snitt langs brua. Alle metoder produserte ikke-konservative resultater, med unntak av narrow band metoden og metoden presentert av Jiao og Moan som oppnådde estimater med stor relativ feil. Single-moment gav de mest ikke-konservative resultatene hvor utmattingsskaden ble underestimert med opp mot 30%. Metoden utarbeidet av Dirlik i tillegg til metoden fra Tovo og Benasciutti resulterte i en relativ feil rundt 10% for Langenuen bru. De viste seg å gi de mest konsistente estimatene ut ifra alle spenningsspektre som ble analysert i denne avhandlingen. Metodene burde uansett bli brukt med forsiktighet på grunn av uforutsigbare ikke-konservative estimeringer.

Preface

This thesis is the result of 20 weeks of work during the final semester of our master's degree programs at the Norwegian University of Science and Technology (NTNU), Department of Structural Engineering.

Several different fields were combined to write the content of this thesis. We have increased our knowledge within known fields from subjects at NTNU, like buffeting wind theory and modal analysis. At the same time, we had to use a fair amount of time to understand fatigue and Gaussian process regression. Looking back, the diversity of fields has been the most challenging and interesting aspect of the past few months.

We want to thank our main supervisor, Professor Ole Øiseth, for his guidance and feedback. We would also thank our co-supervisors, Researchers Aksel Fenerci and Tor Martin Lystad and Associate Professor Gunnstein Thomas Frøseth, for their support throughout the semester.

Håvard Hatling Anfinsen and Mads Kristoffer Waaler
June 10, 2021

Contents

Figures

Tables

Acronyms

AL $\alpha_{0.75}$.

CF closed-form.

DK Dirlik.

DOF degree of freedom.

EOM equation of motion.

FDA fatigue damage accumulation.

FE finite element.

GPR Gaussian process regression.

HF high frequency.

JM Jiao and Moan.

LF low frequency.

MC Monte Carlo.

NB narrow band.

PDF probability density function.

PSD power spectral density.

RE relative error.

RF rainflow.

SC shear center.

SM single moment.

TB Tovo and Benasciutti.

WL Wirsching and Light.

Chapter 1

Introduction

1.1 Langenuen Bridge

The E39 Coastal Highway Route is the largest transport project in Norwegian history. The long-term goal is to cut the travel time by half from Kristiansand in the south to Trondheim in the north. This reduction in travel time is obtained by improving the roads and replacing ferries with some sort of fixed connection [1]. Langenuen bridge, as illustrated in Fig. 1.1, is a planned suspension bridge connecting Stord in the west and Tysnes in the east over the fjord Langenuen. After evaluating several possible crossing locations, the Storting opted for the southern crossing, also called alternative F. To reduce the total cost of the project, a research team consisting of Dr.techn.Olav Olsen, Hydro, Leirvik AS and NTNU have evaluated aluminum as a possible material for the deck. Even though aluminum is seldom used as material in suspension bridges, it has several advantages over regular steel, such as reduced weight and maintenance cost as aluminum does not rust. The material can also be produced locally in Norway, which can reduce transportation costs [2]. During analyses of how well-suited aluminum is for use in suspension bridges, fatigue has been named as a potential issue [3].

Fig. 1.1: Langenuen bridge as presented by Norconsult and The Norwegian Public Roads Administration.

1.2 A Brief History of Fatigue

Incidents related to fatigue have been reported from as early as 1838, when a servant in the mines performed the first known fatigue tests. He tested conveyor chains used in mines, which had failed. Just a few years later, in 1842, the axle of a locomotive broke in Versailles due to fatigue which killed 60 people [4]. Since then, there have been numerous failures related to railways, airplanes, bridges and offshore structures. W. Shütz refers to an English newspaper from 1887 with the headline "Most serious railway accident of the week" [4, p. 265]. This clearly explained the need to gain knowledge about the topic to reduce or avoid future failures. It has been reported that around 80 - 90% of all failures in mechanical and structural components are caused by fatigue [5].

Fatigue is still a topic of research and is continuously developed to fit new designs and different materials. Still, concepts first introduced over 150 years ago are an essential part of fatigue design today. August Wöhler was a railway engineer considered to be the founder of fatigue strength research. He implicitly suggested a design for a finite fatigue life by testing the life of axles. The design suggested that a material can fail through several stress cycles, even when the stresses are under the static strength. He tested this for several materials and presented the results in tables, giving the probability of failure. Finally, in 1910, the American Basquin used Wöhler's tables and established a log-log relationship between the number of cycles before failure ($\log N$) and stress amplitude ($\log \sigma$) [4]. This relationship is still in use today and is known as Wöhler curves or SN-curves.

Another rule which still exists today is the linear damage accumulation first presented by the Swede Palmgren in 1924. Miner further developed the concept in 1945 and it is today known as the Palmgren-Miner's rule, or just Miner's rule. This formulation described the stress process by discrete stress cycles, making it possible to create a spectrum of the different amplitudes [5]. Though a straightforward formulation, the law made it possible to estimate the fatigue damage with varying stress amplitudes. Each block of stress amplitudes was related to an SN-curve, thus building upon the work of Wöhler. There are limitations regarding this law, and there have been several attempts to improve the formulation. None have, however, consistently outperformed the formulation of Palmgren-Miner, which is why most design codes in the world use the original linear damage accumulation [5].

1.3 Fatigue of Bridges

Fatigue is among the most critical forms of failure occurring in bridges. An event that shows the importance of the fatigue assessment is the collapse of the three span Point Pleasant suspension bridge in the United States. After 39 years of operation, the bridge collapsed without warning in December 1967 which resulted in the death of 46 persons [6]. The failure was a direct cause of

fatigue damage accumulation due to vehicle and wind loads on the structure. Occurrences of this type, along with longer main span of modern bridges to meet the community's social and economic requirements are two important reasons why the fatigue damage problem of bridges becomes an even more crucial topic in the design process.

Many highway and railway bridges built in the 19th century have experienced fatigue problems in various details [7]. This information is useful for evaluating the behavior with increased traffic intensity and higher traffic loads along with wind-induced actions on the bridge. Besides the observations from existing structures, numerical analyses of structures exposed to fatigue have increased the knowledge about the fatigue process. In light of the increased computational capacity and increased interest in wind-induced fatigue in the last decades, more analyses such as fatigue life of long-span bridges due to buffeting wind loads have been published [8].

1.4 Existing Literature and Motivation for Research

Fatigue has been a popular topic of research as around 100,000 papers related to fatigue have been published until the year 2000 [9]. However, a large part of the research performed on fatigue is related to cyclic loading with constant stress amplitudes. Most fatigue tests are also performed under constant stress amplitudes. This thesis is concerned with fatigue damage under random wind loading, which is a less developed field of research [10]. Random loading includes not being able to describe a load in an exact manner, but instead using statistical properties.

There have been several attempts to create closed-form expressions for fatigue damage with a wide-banded stress spectrum [5, 11–14]. This removes the need to perform a simulation to obtain a stress-time series, where the stress cycles have to be counted. Most of the authors of proposed closed-form methods test their formulas on various spectrums designed for testing purposes only. We want to perform a comparison of these methods with stress spectrums obtained by buffeting wind loading. We intend to test these closed-form methods against a combination of the rainflow algorithm and Palmgren-Miner's rule on simple shear frames and the planned Langenuen bridge.

Testing these methods on different systems can be quite a complex computational operation if the wind load is modeled accurately. Gaussian process regression can be utilized to reduce the computational time by using a sequential updating process. Similar analyses have been performed by Lystad et al. [15] and Gramstad et al. [16], where the process was applied to estimate the extreme structural response of a structure. Gaussian process regression has been a popular class within machine learning problems since Carl Edward Rasmussen wrote *Gaussian Processes for Machine Learning* in 2006, which in combination with the analyses by Lystad et al. and Gramstad et al. form the foundation for the theory and procedure related to the topic in this thesis.

1.5 Scope of Thesis

The primary goal of this thesis is to compare some of the most popular closed-form methods with the rainflow method for calculating the fatigue damage in buffeting wind loading, using a sequential updating approach with Gaussian process regression. The procedure for calculating fatigue damage is first applied to simple shear frame models as a proof of concept and finally tested on a long suspension bridge. Other fields such as finite element analysis, wind modeling and modal response are also included to perform this comparison in a sufficiently accurate manner. Even though this thesis includes a theoretical foundation for these topics, the fatigue comparison is the most important and thus most prioritized in terms of theoretical background and analysis.

We would also like to specify that although fatigue damage is the most important topic, the comparisons are the primary goal, not the expected life of the structure itself. The comparisons are performed for different SN-curves to determine how this affects the relative error of the closed-form methods. In a simple fatigue analysis, where the goal is to estimate the expected life, we would only need one SN-curve. Different curves give drastically different results, meaning that the expected lifetimes in years for the structures are unreliable. Also, the aluminum girder of the Langenuen bridge was taken into account by using appropriate SN-curves. Apart from this, aluminum as a material is not a central part of this thesis.

To test the different methods under realistic and physical scenarios the wind load had to be represented accurately. A substantial part of the work was put into modeling the wind and calculating the fatigue damage based on a joint probability distribution between the mean wind velocity and standard deviation of the turbulence in the along-wind direction. However, wind loading can be quite complex, and we made some assumptions to simplify the analyses. The wind was assumed to act perpendicular to the structures throughout the analyses at all times. Also, the static contribution from the wind load was disregarded, as only the zero-mean dynamic component was included. Accordingly, the mean stress was disregarded from all the fatigue analyses.

For the Langenuen bridge, a finite element model was needed to extract results. To get accurate results such as mode shapes and natural frequencies, without using much time on the modeling, an Abaqus model was provided to us by the supervisor of the master's thesis *Aerodynamic Stability of a Suspension Bridge with an Aluminum Girder* [17]. The Abaqus model is based on the panel girder concept in the report *Langenuen Suspension Bridge-Aluminum Bridge Girder Alternative* proposed by Dr.techn. Olav Olsen in 2020 [18]. It should be mentioned that Dr.techn. Olav Olsen discovered issues with this concept concerning fatigue calculations. As a consequence, Dr.techn. Olav Olsen decided to terminate the design process of the panel girder concept. Nevertheless, the model is still relevant for comparison of calculation methods for fatigue damage.

Chapter 2

Stochastic Processes

2.1 Structural Dynamics and Modal Theory

Modal analysis is a well-established procedure to identify the dynamic characteristics of any system. A mathematical model of the dynamic behavior is based on the equation of motion (EOM), which for a linear multi-degree of freedom system can be expressed as

$$\boldsymbol{M}_0\ddot{\boldsymbol{r}}(t)+\boldsymbol{C}_0\dot{\boldsymbol{r}}(t)+\boldsymbol{K}_0\boldsymbol{r}(t)=\boldsymbol{q}_{tot}(t) \tag{2.1}$$

where $\boldsymbol{M}_0$, $\boldsymbol{C}_0$ and $\boldsymbol{K}_0$ represent the mass-, damping- and stiffness-matrices in still-air, $\ddot{\boldsymbol{r}}(t)$ and $\dot{\boldsymbol{r}}(t)$ represent the double- and single-derivative of the physical response $\boldsymbol{r}(t)$, and $\boldsymbol{q}_{tot}(t)$ represents the total force vector [19]. For a line-like structure, the displacement $\boldsymbol{r}(t)$ can be expressed as a function of the longitudinal coordinate x. A modal approach represents the displacement by

$$\boldsymbol{r}(x,t)=\boldsymbol{\Phi}(x)\boldsymbol{\eta}(t) \tag{2.2}$$

Here, the natural modes $\boldsymbol{\Phi}(x)\in\mathbb{R}^{N_{DOF}xN_{mod}}$ and the generalized modal coordinates $\boldsymbol{\eta}(t)\in\mathbb{R}^{N_{mod}}$ are given as

$$\boldsymbol{\Phi}(x)=\begin{bmatrix}\boldsymbol{\phi}_1 & \boldsymbol{\phi}_2 & \dots & \boldsymbol{\phi}_{N_{mod}}\end{bmatrix},\quad \boldsymbol{\eta}(t)=\begin{bmatrix}\eta_1 & \eta_2 & \dots & \eta_{N_{mod}}\end{bmatrix}^T \tag{2.3}$$

where N_{mod} is the number of mode shapes to be included in the analysis. The EOM from Eq.(2.1) expressed in modal coordinates becomes

$$\boldsymbol{M}_0\boldsymbol{\Phi}\ddot{\boldsymbol{\eta}}(t)+\boldsymbol{C}_0\boldsymbol{\Phi}\dot{\boldsymbol{\eta}}(t)+\boldsymbol{K}_0\boldsymbol{\Phi}\boldsymbol{\eta}(t)=\boldsymbol{q}_{tot}(t) \tag{2.4}$$

Premultiplying Eq. (2.4) by $\boldsymbol{\Phi}^T$ the modal EOM becomes

$$\tilde{\boldsymbol{M}}_0\ddot{\boldsymbol{\eta}}(t)+\tilde{\boldsymbol{C}}_0\dot{\boldsymbol{\eta}}(t)+\tilde{\boldsymbol{K}}_0\boldsymbol{\eta}(t)=\tilde{\boldsymbol{Q}}_{tot}(t) \tag{2.5}$$

Assuming a proportional damping matrix, the modal mass $\tilde{\boldsymbol{M}}_0$, damping $\tilde{\boldsymbol{C}}_0$ and stiffness $\tilde{\boldsymbol{K}}_0$ matrices become

$$\tilde{\boldsymbol{M}}_0=\int_L\boldsymbol{\Phi}(x)^T\boldsymbol{M}_0\boldsymbol{\Phi}(x)dx \tag{2.6}$$

$$\tilde{\boldsymbol{C}}_0=2\tilde{\boldsymbol{M}}_0\boldsymbol{\Omega}\boldsymbol{\zeta} \tag{2.7}$$

$$\tilde{\boldsymbol{K}}_0 = \boldsymbol{\Omega}^2 \tilde{\boldsymbol{M}}_0 \tag{2.8}$$

and the modal load vector $\tilde{\mathbf{Q}}_{tot}(t)$ is defined by

$$\tilde{\mathbf{Q}}_{tot}(t) = \int_{L_{exp}} \boldsymbol{\Phi}(x)^T \boldsymbol{q}_{tot}(t) dx \tag{2.9}$$

where L and L_{exp} indicate integration over the entire structure and the force exposed part of the structure, respectively. In Eq. (2.7) and Eq. (2.8), the spectral matrix of the eigenvalue problem is given by $\boldsymbol{\Omega}^2 = diag(\omega_1^2, \omega_2^2, \ldots, \omega_{N_{mod}}^2)$ and the damping ratios read $\boldsymbol{\zeta} = diag(\zeta_1, \zeta_2, \ldots, \zeta_{N_{mod}})$, each associated with the corresponding mode.

2.2 Power Spectral Density

The power spectral density (PSD) describes how the energy of a signal in a specific point in space is distributed in the frequency domain. The auto PSD is calculated by applying a Fourier transform of the correlation function, which for a random stationary process $X(t)$ is defined by [20]

$$R_X(\tau) = E[X(t)X(t+\tau)] \tag{2.10}$$

where $E[\cdot]$ operator denotes the probabilistic expected value and τ is the timelag. By normalizing (or adjusting) the mean value $E[X(t)] = 0$ and assuming that the process $X(t)$ has no periodic components, the Fourier integral does not diverge to infinity

$$R_X(\tau \to \infty) = 0, \qquad \int_{-\infty}^{\infty} |R_X(\tau)| \, d\tau < \infty \tag{2.11}$$

Taking the Fourier transform of the autocorrelation function gives the PSD $S_X(\omega)$. The inverse Fourier transform of the PSD gives the autocorrelation function $R_X(\tau)$, making them Fourier pairs [20]

$$S_X(\omega) = \frac{1}{2\pi} \int_{-\infty}^{\infty} R_X(\tau) e^{-i\omega\tau} d\tau, \qquad R_X(\tau) = \int_{-\infty}^{\infty} S_X(\omega) e^{i\omega\tau} d\omega \tag{2.12}$$

The cross-spectral density function of a pair of random stationary processes is defined in the same way as the autocorrelation function. The cross correlation function of two stationary processes $x(t)$ and $y(t)$ is defined by

$$R_{XY}(\tau) = [X(t)Y(t+\tau)] \tag{2.13}$$

If $X(t)$ and $Y(t)$ are uncorrelated when $\tau \to \infty$ and $E[X(t)]$ or $E[Y(t)]$ is equal to zero, the Fourier transform of Eq. (2.13) and its inverse become

$$S_{XY}(\omega) = \frac{1}{2\pi} \int_{-\infty}^{\infty} R_{XY}(\tau) e^{-i\omega\tau} d\tau, \qquad R_{XY}(\tau) = \int_{-\infty}^{\infty} S_{XY}(\omega) e^{i\omega\tau} d\omega \tag{2.14}$$

where $S_{XY}(\omega)$ denotes the cross power spectral density which represents the power of two different signals $X(t)$ and $Y(t)$. The PSD defined in Eq. (2.12) and Eq. (2.14) are so-called two sided, meaning that they are defined for ω in the range $\omega \in (-\infty, \infty)$. In practical applications, a one-sided PSD where ω is limited in the range $\omega \in (0, \infty)$ is widely used [21]

$$G_X(\omega) = 2S_X(\omega), \qquad G_{XY}(\omega) = 2S_{XY}(\omega) \tag{2.15}$$

The spectral density can be written on matrix form called the cross-spectral density matrix. For $\boldsymbol{X} \in \mathbb{R}^N$ random processes, the cross-spectral density matrix at $x = x_i$ can be written as

$$\boldsymbol{S_{XX}}(x_i, \omega) = \begin{bmatrix} S_{X_1X_1} & S_{X_1X_2} & \dots & S_{X_1X_n} \\ S_{X_2X_1} & S_{X_2X_2} & \dots & \vdots \\ \vdots & \vdots & \ddots & \vdots \\ S_{X_nX_1} & \dots & \dots & S_{X_nX_n} \end{bmatrix} \tag{2.16}$$

where the diagonal terms correspond to the auto-spectrums and the off-diagonal terms are cross-spectrums [19].

2.3 Frequency Response Function

The relation between the PSD of the input $\boldsymbol{S}_Q$, and the PSD of the output $\boldsymbol{S}_R$ can be expressed as

$$\boldsymbol{S}_R(\omega) = \overline{\boldsymbol{H}}(\omega)\boldsymbol{S}_Q(\omega)\boldsymbol{H}(\omega)^T \tag{2.17}$$

Here, $\overline{(\cdot)}$ and $(\cdot)^T$ denote the complex conjugate and transpose of the matrix, respectively. The frequency response function is defined by

$$\boldsymbol{H}(\omega) = \boldsymbol{X}(\omega)\boldsymbol{Q}^{-1}(\omega) \tag{2.18}$$

where $\boldsymbol{X}(\omega)$ represents the response and $\boldsymbol{Q}^{-1}(\omega)$ the inverse load excitation in the frequency domain [20].

2.4 Spectral Moments and Bandwidth Parameters

The frequency domain distribution of a PSD can be described by a set of spectral moments M_i [7]. Given a one-sided spectral density $G_{xx}(f)$, the i^{th} moment of the spectral density is given by

$$M_i = \int_0^\infty f^i G_{xx}(f) df \tag{2.19}$$

The spectral moments represent some important properties of the process $X(t)$, for instance the variance σ_x^2 of the process $X(t)$ and its derivatives [11]

$$M_0 = \sigma_x^2 \quad , \qquad M_2 = \sigma_{\dot{x}}^2 \quad , \qquad M_4 = \sigma_{\ddot{x}}^2 \tag{2.20}$$

In order to characterize the spread of the given process, it's useful to define bandwidth parameters as a function of spectral moments. The general definition of the bandwidth parameter α_i is given by

$$\alpha_i = \frac{M_i}{\sqrt{M_0 M_{2i}}} \tag{2.21}$$

The most commonly used bandwidth parameters are α_1 and α_2. Assuming a Gaussian probability distribution of the stress, the so-called irregularity factor α_2 describes the ratio of the expected mean up-crossing rate υ_0^+ and the rate of peaks υ_p for a narrow-banded process

$$\alpha_2 = \frac{\upsilon_0^+}{\upsilon_p} \quad , \qquad \upsilon_0^+ = \sqrt{\frac{M_2}{M_0}} \quad , \qquad \upsilon_p = \sqrt{\frac{M_4}{M_2}} \tag{2.22}$$

The spectral bandwidth parameter ϵ is often used to measure the bandwidth of a process, defined by

$$\epsilon = \sqrt{1 - \alpha_2^2} \tag{2.23}$$

ϵ tends to zero for a narrow-banded process, and one for a wide-banded process.

2.5 Buffeting Wind Theory

Buffeting wind loading may be described as the load on a structure due to unsteady wind fluctuations. In order to formalize the buffeting load, a horizontal bridge type of structure is studied. The definition of the structural axes is shown in Fig. 2.1, where SC symbolizes the shear center and the x-axis represents the longitudinal direction of the structure. Neglecting the axial displacement in the spanwise direction x, the global displacement vector can be represented by the sum of a time invariant mean part $\bar{\boldsymbol{r}}(x)$ and a fluctuating part $\boldsymbol{r}(x,t)$

$$\boldsymbol{r}_{tot}(x,t) = \bar{\boldsymbol{r}}(x) + \boldsymbol{r}(x,t) \tag{2.24}$$

where

$$\bar{\boldsymbol{r}}(x) = \begin{bmatrix} \bar{r}_y & \bar{r}_z & \bar{r}_\theta \end{bmatrix}^T, \quad \boldsymbol{r}(x,t) = \begin{bmatrix} r_y & r_z & r_\theta \end{bmatrix}^T \tag{2.25}$$

Here, r_i, $i \in \{y, z, \theta\}$ describes the horizontal, vertical and torsional deformation along the bridge girder according to Fig. 2.1. The wind actions on the beam girder can be approximated by assuming that the mean wind direction coincides with the axis perpendicular to the longitudinal x-direction of the bridge. In addition to the mean wind velocity U, the turbulence in the along-wind direction

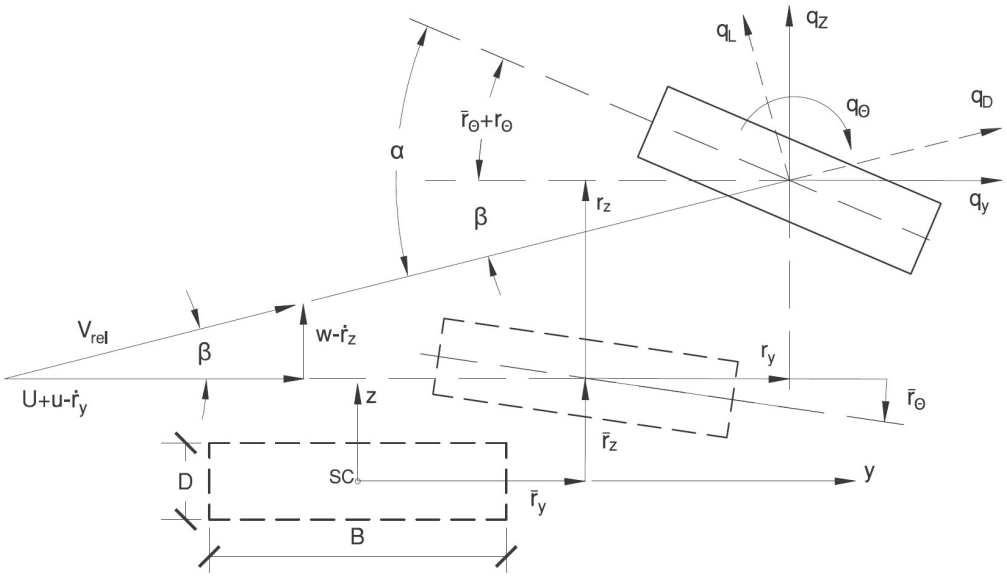

Fig. 2.1: Flow and displacement quantities for buffeting wind.

u and the vertical wind direction w expressed in global coordinates are of interest. As a result, the total wind velocity V is described by [19]

$$V = U + \boldsymbol{v}^T = U + \begin{bmatrix} u(x,t) & w(x,t) \end{bmatrix}^T \tag{2.26}$$

Assuming that the turbulences $u(x,t)$ and $w(x,t)$ are much smaller than the mean wind U, small displacements $\boldsymbol{r}(x,t)$, small relative angle of attack β and a quasi steady theory of the force components give raise to linearization of the wind loads. By these assumptions, the wind load can be expressed as

$$\boldsymbol{q}_{tot}(x,t) = \bar{\boldsymbol{q}}(x) + \boldsymbol{q}(x,t) = \bar{\boldsymbol{q}}(x) + \boldsymbol{B}_q \boldsymbol{v}(x,t) + \boldsymbol{C}_{ae} \dot{\boldsymbol{r}}(x,t) + \boldsymbol{K}_{ae} \boldsymbol{r}(x,t) \tag{2.27}$$

where $\bar{\boldsymbol{q}}(x)$ describes the mean (static) wind load of the girder with a cross sectional height D and width B

$$\bar{\boldsymbol{q}}(x) = \frac{1}{2}\rho U^2 B \begin{bmatrix} \frac{D}{B}\bar{C}_D \\ \bar{C}_L \\ B\bar{C}_M \end{bmatrix} \tag{2.28}$$

The fluctuating wind load is described by

$$\boldsymbol{B}_q = \frac{1}{2}\rho U B \begin{bmatrix} 2\frac{D}{B}\bar{C}_D & \frac{D}{B}C'_D - \bar{C}_L \\ 2\bar{C}_L & C'_L + \frac{D}{B}\bar{C}_D \\ 2B\bar{C}_M & BC'_M \end{bmatrix} \tag{2.29}$$

$$\boldsymbol{C}_{ae} = -\frac{1}{2}\rho UB \begin{bmatrix} 2\frac{D}{B}\bar{C}_D & \frac{D}{B}C'_D - \bar{C}_L & 0 \\ 2\bar{C}_L & C'_L + \frac{D}{B}\bar{C}_D & 0 \\ 2B\bar{C}_M & BC'_M & 0 \end{bmatrix} \tag{2.30}$$

$$\boldsymbol{K}_{ae} = \frac{1}{2}\rho U^2 B \begin{bmatrix} 0 & 0 & \frac{D}{B}C'_D \\ 0 & 0 & C'_L \\ 0 & 0 & BC'_M \end{bmatrix} \tag{2.31}$$

where $\boldsymbol{B}_q\boldsymbol{v}$ is the buffeting load related to the turbulence components u and w, while $\boldsymbol{C}_{ae}\dot{\boldsymbol{r}}$ and $\boldsymbol{K}_{ae}\boldsymbol{r}$ represent the motion induced loads associated to the structural velocity and displacement. The sectional admittance functions $\bar{C}_i, C'_i, i \in \{D, L, M\}$ describe the mean value and the derivative of the static force coefficient associated to the cross sectional drag D, lift L and moment M [22].

2.6 Wind Field Characteristics

2.6.1 Mean Wind Velocity Distribution

Across the lifespan of a structure exposed to wind loads, it is often necessary to know the complete distribution of wind velocities. Naturally, the wind will vary from site to site but is often described using a Weibull distribution of the random mean wind velocity U [10]

$$f(U) = \frac{kU^{k-1}}{c^k} \exp\left[-\left(\frac{U}{c}\right)^k\right] \tag{2.32}$$

where c is the scale factor usually varying between $3m/s$ and $10m/s$. k is a dimensionless shape factor and is typically in the range $1.3-2.0$ [10]. If $k = 2.0$, the distribution is known as a Rayleigh distribution. Integrating Eq. (2.32) with respect to the mean wind velocity U gives the probability of exceedance or the cumulative Weibull distribution

$$1 - F(U) = \exp\left\{\left[-\left(\frac{U}{c}\right)^k\right]\right\} \tag{2.33}$$

As illustrated in Fig. 2.2a, the Weibull function is sensitive to variations of both the shape factor k and the scale factor c. Figure 2.2b shows the cumulative Weibull distribution of $k = 2.0$ and $c = 6.0$, also known as the cumulative Rayeligh distribution. By fitting the parameters c and k, the Weibull distribution can represent the complete wind population for several different locations. The following empirical equations can be used to approximate the parameters [23]

$$k = \left(\frac{\sigma}{U}\right)^{-1.086} \quad (1 \leq k \leq 10), \quad c = \frac{U}{\Gamma(1 + 1/k)} \tag{2.34}$$

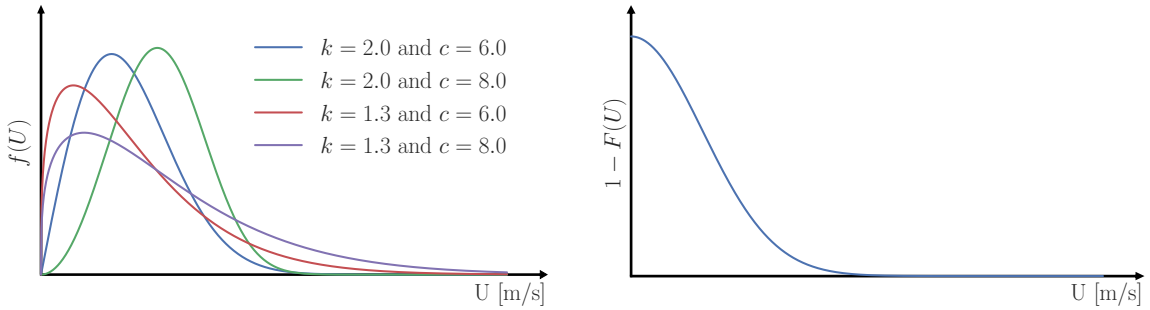

(a) Illustration of the sensitivity for the Weibull distribution. **(b)** Cumulative Rayleigh distribution for $c = 6.0$.

Fig. 2.2: Weibull distributions.

where σ is the standard deviation of the wind and Γ is the gamma function defined as

$$\Gamma(x) = \int_0^\infty t^{x-1} \exp\{(-t)\} dt \tag{2.35}$$

2.6.2 Turbulence Intensity Distribution

The turbulence intensity gives information about the turbulent energy of the wind, and it is defined by [24]

$$I_i = \frac{\sigma_i}{U}, \qquad i = u, v, w \tag{2.36}$$

where $\sigma_i, i \in \{u, v, w\}$ represents the standard deviation of the turbulence components, and U represents the mean wind velocity. The turbulence parameters will vary in time and site. Fenerci and Øiseth [25] established a probabilistic turbulence model of the Hardanger bridge in Norway using a lognormal probability distribution. The general probability density function (PDF) expression for a random variable x with lognormal distribution reads

$$f(x|\tilde{\mu}, \tilde{\sigma}) = \frac{1}{x\tilde{\sigma}\sqrt{2\pi}} exp\left(\frac{-(\ln x - \tilde{\mu})^2}{2\tilde{\sigma}^2}\right) \tag{2.37}$$

where the distribution parameters $\tilde{\mu}$ and $\tilde{\sigma}$ represent the mean value and standard deviation of the natural logarithm of the random variable x. Substituting $x = \sigma_i$ into Eq.(2.37) gives the proposed lognormal PDF of the standard deviation of turbulence component i.

2.6.3 Wind Field Spectrum

The wind field for a horizontal line-like structure, where the turbulence component v is neglected, can be described as a stationary stochastic process by a one-sided cross-spectral density matrix

equal to [25]

$$\boldsymbol{G}_V = \begin{bmatrix} G_{uu}(\Delta s, f) & G_{uw}(\Delta s, f) \\ G_{wu}(\Delta s, f) & G_{ww}(\Delta s, f) \end{bmatrix} \tag{2.38}$$

where $G_{i_1 i_2}$, $i \in \{u, w\}$ represents the cross-spectral densities for the i_1 and i_2 components of the turbulence separated by two points with distance Δs. The cross-spectral density for a single turbulence component $G_{i_1 i_2}$ for wind separation perpendicular to the along-wind direction x, horizontally y or vertically z can be described by the auto-spectral density function $G_i(f)$ and the normalized co-spectrum $\hat{C}o_{ij}(\Delta s, f)$

$$G_{i_1 i_2}(\Delta s, f) = \sqrt{G_{i_1}(f) G_{i_2}(f)}\hat{C}o_{ij}(\Delta s, f), \quad i = u, w \quad j = y, z \tag{2.39}$$

There are several expressions to describe the cross-spectral density matrix from Eq. (2.38). The following expression for the auto-spectrum given by N400 is often used [26]

$$\frac{f G_i(f)}{\sigma_i^2} = \frac{A_i \hat{f}_i}{(1 + 1.5 A_i \hat{f}_i)^{5/3}}, \quad \hat{f}_i = \frac{f\, {}^x L_i}{U}, \quad i = u, w \tag{2.40}$$

where f represents the frequency in Hz, σ_i is the standard deviation of turbulence component i, A_i is a non-dimensional spectral parameter, ${}^x L_i$ is the integral length scale of turbulence component i in the along-wind direction x, and U represents the mean along-wind velocity. The normalized co-spectrum provides the spatial correlation of the turbulence component i along the structure, usually represented sufficiently well by an exponentially decaying curve. The co-spectrum proposed by Davenport is commonly used, which reads [25]

$$\hat{C}o_{ij}(\Delta s, f) = exp\left(- C_{ij} \frac{f \Delta s}{U} \right), \quad i = u, w \quad j = y, z \tag{2.41}$$

where C_{ij} represents the decay coefficient.

2.6.4 Turbulence Length Scale

The turbulence length scale or the integral length scale can be interpreted as the average eddy size (length) of the turbulence [27]. Nine different turbulent length scales can be defined in a spatial system. The length scale of the turbulence component i in the along-wind direction x can be written as

$${}^x L_i = \frac{1}{\sigma_i^2} \int_0^\infty R_{ii}(x) dx, \quad i = u, v, w \tag{2.42}$$

where $R_{ii}(x)$ is the cross-covariance function of the turbulence velocity component i, $i \in \{u, v, w\}$ describing the along-, cross-, and vertical-wind turbulence. By assuming that the flow disturbance travels with the mean wind U according to Taylor's hypothesis, the turbulence length scale

described in Eq. (2.42) becomes

$$^{x}L_i = \frac{U}{\sigma_i^2}\int_0^\infty R_i(\tau)d\tau, \quad i = u, v, w \tag{2.43}$$

where $R_i(\tau)$ is the auto-correlation function of the turbulence component i.

Chapter 3

Gaussian Process Regression

Regression analysis is an important topic for engineers, mathematicians, financiers and others. A simple linear or polynomial regression will update its parameters to fit newly observed data. A Gaussian process regression (GPR) is, on the other hand, non-parametric and finds a distribution over all possible functions which fit the newly observed data [28]. Sampling from such a Gaussian distribution process will result in an infinite number of function realizations. Like any other Gaussian distributed parameter, the function is not deterministic and can only be described by statistical properties before the sample realization. In practice, GPR is used to estimate unknown values based on a set of empirical data, called a training data set. Unknown values might be expensive or computational heavy to approximate through regular analysis. Some might be impossible, as enough data does not exist. The GPR does not consider the physical or mathematical underlying problem, only the statistical properties of the known data. The connection to machine learning comes from the fact that this method is trained to provide better results when it is fed with more observed data. The standard deviation of the prediction becomes smaller as the training data set increases.

3.1 Gaussian Process

A Gaussian process f is specified by its mean $m(x)$ and covariance function $k(x, x')$ defined as [28]

$$m(x) = E[f(x)] \tag{3.1}$$

$$k(x, x') = E[(f(x) - m(x))(f(x') - m(x'))] \tag{3.2}$$

and the Gaussian process is then expressed as

$$f(x) \sim \mathcal{GP}(m(x), k(x, x')) \tag{3.3}$$

Often the mean is set to zero to make notations easier. An important property of a Gaussian process is that for a finite set of points $[\boldsymbol{x}_1, \boldsymbol{x}_2 ... \boldsymbol{x}_n]$, the distribution of the functions $[f(\boldsymbol{x}_1), f(\boldsymbol{x}_2) ... f(\boldsymbol{x}_n)]$ are multivariate Gaussian expressed in terms of the mean values $[m(\boldsymbol{x_1}), m(\boldsymbol{x_2}) ... m(\boldsymbol{x_n})]$ and a covariance $\boldsymbol{K}$. Even when the Gaussian process is updated with observed values, the conditional distribution over the unknown values remain Gaussian [16].

3.2 Covariance Functions

Let $\boldsymbol{X}$ be a training data set with known values $\boldsymbol{f}$. Also let $\boldsymbol{X}_*$ be a new set of test points with unknown values $\boldsymbol{f}_*$. The covariance functions presented in Eq. 3.4 and Eq. 3.5 are dependent on the Euclidean distance $\boldsymbol{D}(\boldsymbol{X},\boldsymbol{X}_*)$ between $\boldsymbol{X}$ and $\boldsymbol{X}_*$. Note that the Euclidean distance $\boldsymbol{D}(\boldsymbol{X},\boldsymbol{X}_*)$ can be calculated for an arbitrary number of dimensions of $\boldsymbol{X}$, making GPR valid for multiple dimensions as well.

3.2.1 Squared Exponential

Among covariance functions, also called kernals, the squared exponential is probably the most widely used for machine learning applications [28]. The kernel is defined as [29]

$$K_{se}(\boldsymbol{D}) = \sigma_f^2 \exp\left\{\left(-\frac{1}{2l^2}\boldsymbol{D}^2\right)\right\} \tag{3.4}$$

where σ_f^2 and l are called hyperparameters and represent the signal variance and length scale, respectively. $\boldsymbol{D}$ is the Euclidean distance matrix between a training data set $\boldsymbol{X}$ and a test data set $\boldsymbol{X}_*$. l is directly related to the correlation between points in $\boldsymbol{D}$, where a larger value of l indicates a higher correlation.

3.2.2 Matérn

The Matérn kernel is a generalization of the squared exponential. It has a parameter ν that controls how smooth the prediction becomes. The kernel is given as [30]

$$K_{Mat}(\boldsymbol{D}) = \frac{\sigma_f^2}{\Gamma(\nu)2^{\nu-1}}\left(\frac{\sqrt{2\nu}}{l}\boldsymbol{D}\right)^{\nu} K_\nu\left(\frac{\sqrt{2\nu}}{l}\boldsymbol{D}\right) \tag{3.5}$$

where $K_\nu(\cdot)$ is a modified Bessel function. If $\nu \to \infty$ the kernel equals the squared exponential. Also, note that if $\nu = p + 1/2$, where p is an integer, the expression will be considerably simplified. The expressions for $\nu = 3/2$ and $\nu = 5/2$ become [28]

$$K_{Mat,\nu=3/2}(\boldsymbol{D}) = \sigma_f^2(1 + \frac{\sqrt{3}\boldsymbol{D}}{l})\exp\left\{(-\frac{\sqrt{3}\boldsymbol{D}}{l})\right\} \tag{3.6}$$

$$K_{Mat,\nu=5/2}(\boldsymbol{D}) = \sigma_f^2(1 + \frac{\sqrt{5}\boldsymbol{D}}{l} + \frac{5\boldsymbol{D}^2}{3l^2})\exp\left\{(-\frac{\sqrt{5}\boldsymbol{D}}{l})\right\} \tag{3.7}$$

3.3 Observation Prediction

Before the training data set is applied to the algorithm, the Gaussian process has a prior distribution. Drawing functions from prior are usually not interesting since the uncertainties are large

(Fig. 3.1a). In the posterior distribution, the functions that do not agree with the new observations are disregarded. The known values $\boldsymbol{f}$ and the unknown values $\boldsymbol{f}_*$ are expressed as a joint multivariate Gaussian distribution [28]

$$\begin{bmatrix} \boldsymbol{f} \\ \boldsymbol{f}_* \end{bmatrix} \sim \mathcal{N}\left(\begin{bmatrix} \boldsymbol{M}_X \\ \boldsymbol{M}_{X_*} \end{bmatrix}, \begin{bmatrix} K(\boldsymbol{X},\boldsymbol{X}) + \sigma_n^2 \boldsymbol{I} & K(\boldsymbol{X},\boldsymbol{X}_*) \\ K(\boldsymbol{X}_*,\boldsymbol{X}) & K(\boldsymbol{X}_*,\boldsymbol{X}_*) \end{bmatrix} \right) \tag{3.8}$$

where $\mathcal{N}$ means Gaussian distribution, and $\boldsymbol{M}_X$ and $\boldsymbol{M}_{X_*}$ represent the mean values of the training data set $\boldsymbol{X}$ and the test data set $\boldsymbol{X}_*$. Then, the conditional distribution is given as

$$\boldsymbol{f}_* | \boldsymbol{X}, \boldsymbol{f}, \boldsymbol{X}_* \sim \mathcal{N}\left(\bar{\boldsymbol{f}}_*, cov(\boldsymbol{f}_*)\right) \tag{3.9}$$

where the predictive mean $\bar{\boldsymbol{f}}_*$ and covariance matrix $cov(\boldsymbol{f}_*)$ are [16]

$$\bar{\boldsymbol{f}}_* = \boldsymbol{M}_{X_*} + K(\boldsymbol{X}_*,\boldsymbol{X})\left[K(\boldsymbol{X},\boldsymbol{X}) + \sigma_n^2 \boldsymbol{I}\right]^{-1}(\boldsymbol{f} - \boldsymbol{M}_X) \tag{3.10}$$

$$cov(\boldsymbol{f}_*) = K(\boldsymbol{X}_*,\boldsymbol{X}_*) - K(\boldsymbol{X}_*,\boldsymbol{X})\left[K(\boldsymbol{X},\boldsymbol{X}) + \sigma_n^2 \boldsymbol{I}\right]^{-1} K(\boldsymbol{X},\boldsymbol{X}_*) \tag{3.11}$$

where σ_n^2 is the noise variance for an equally distributed Gaussian noise. A predictive mean $\bar{\boldsymbol{f}}_*$ is illustrated when drawn from prior (Fig. 3.1a) and posterior (Fig. 3.1b).

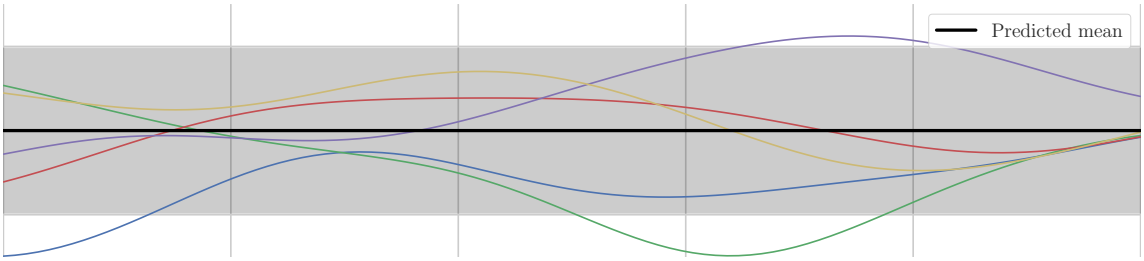

(a) Prior distribution with 95th percentile

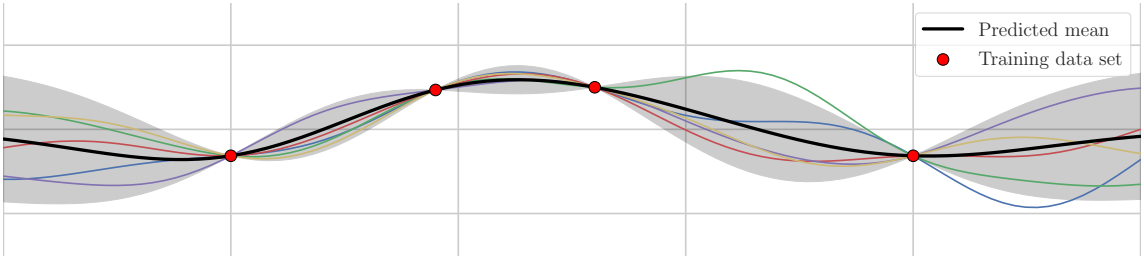

(b) Posterior distribution with 95th percentile

Fig. 3.1: Prior and posterior distribution of a random Gaussian process with the squared exponential kernel. Random samples are illustrated as colored lines, and the 95th percentile is shaded gray.

Chapter 4

Fatigue Damage Accumulation

4.1 Physical Process of Fatigue

Fatigue is a failure mechanism that occurs when a structural material is subjected to cyclic loading over time. A cyclic loading of sufficient magnitude will cause gradual propagation of cracks, and eventually, failure of the material [5]. Fatigue damage is classified into low- and high-cycle fatigue. Fatigue life below 10^5 cycles is referred to as low-cycle fatigue, and will mainly occur when the material accumulates plastic deformations. The high-cycle fatigue process involves fatigue life above 10^5 cycles where the strain is essentially elastic. The fatigue history may be separated into the three stages: initiation, crack growth and final failure [31]. The total fatigue life is the sum of the cycles that occur in the first two stages, the initiation of a crack and the stable crack growth.

4.2 Narrow- and Wide-Banded Processes

Structures such as suspension bridges will be affected by both narrow- and wide-banded load processes. A narrow-banded process is a process where the spectral density $G(\omega)$ has significant values only in a band of frequencies which is small compared to the center frequency. A wide-banded process has significant power over a wide range of frequencies [13]. Fig. 4.1 shows both a narrow- and wide-banded process with the corresponding time domain representation, illustrated in Fig. 4.2. Wind loading may produce narrow-banded vibrations for vortex-shedding-induced vibrations in low turbulence conditions, while a random wide-banded response often occurs for along-wind loading.

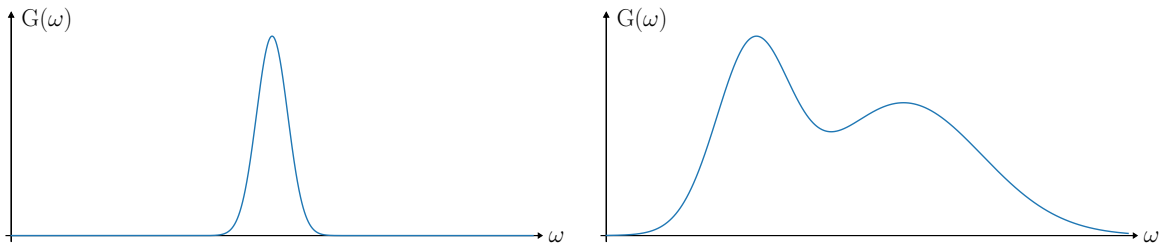

(a) Narrow-banded spectral density.

(b) Wide-banded spectral density.

Fig. 4.1: Spectral density plots.

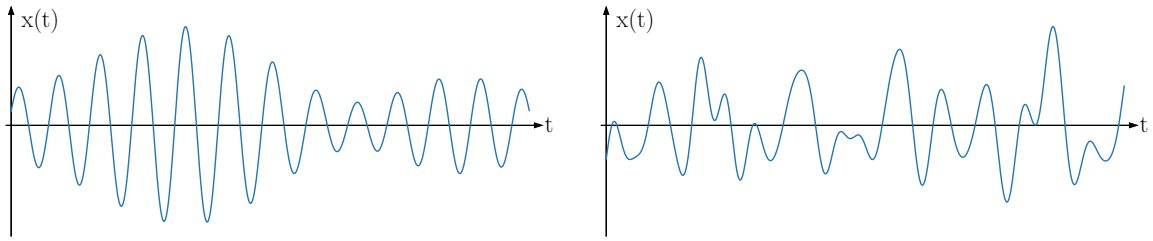

(a) Time domain representation narrow-banded process. **(b)** Time domain representation wide-banded process.

Fig. 4.2: Time domain representation of spectral density.

4.3 Approaches to Fatigue Assessment

Fatigue is a challenging failure mode due to several uncertainties in the design process. Uncertainties such as translating the laboratory data into on-site predictions, model the environmental load effects on the system over an entire lifetime, determine critical details exposed for fatigue failure and correct prediction of the fatigue initiation makes the failure mode challenging [5]. Different approaches are used based on where in the design process the analyst is, type of component and loading.

4.3.1 Fracture Mechanics

In a structural component, there will always be some imperfections, such as cracks. These cracks can develop into dangerous cracks through cyclic loading. The term fracture mechanics involves designing components to reduce the possibility of fatigue failure [32]. In contrast to other methods, fracture mechanics relies on inspection to find cracks. The inspection can be both time-consuming and expensive. The parameter that affects the growth rate of a crack the most is the stress intensity factor, defined as

$$\Delta K = F \Delta S \sqrt{\pi a} \tag{4.1}$$

where F is a dimensionless geometry parameter, ΔS is the stress range and a is the crack depth. The stress intensity factor can quantify the severity of a crack and can be directly connected to the growth of a crack through the Paris law [32]

$$\frac{da}{dN} = C(\Delta K)^m \tag{4.2}$$

where C is a material constant and m is the slope in the log-log plot of this equation. A fitting curve is applied after several experimental tests with different ΔK - values.

4.3.2 Stress-Based Approach

The stress-based approach assumes that the material does not experience plastic yielding [5]. Through numerous fatigue tests, where a specimen experiences oscillatory stress, the strength of the material can be computed. Higher cyclic stress requires fewer cycles before failure. Plotting these tests in a diagram and fit a line gives nominal stress versus life (SN-curves) as seen in Fig. 4.3. Due to the rapid reduction of life when the stress is increased, the diagram is often displayed with a logarithmic scale. There are large variations in observed cycles to failure for most materials and at several stress levels. The coefficient of variation for cycles to failure can range from 50% to 150% [5]. As a conservative approach, the curve used is often set as a lower bound design curve instead of the median curve. Both are shown in Fig. 4.3. If the line is linear in the logarithmic plot, the expression can be written as

$$NS^m = K \tag{4.3}$$

where K is the fatigue strength coefficient and m, called the fatigue strength exponent, is the slope of the logarithmic curve. S is the stress range or amplitude. The use of a linear curve in logarithmic scale simplifies further calculations and is widely used for fatigue analysis today. Other approaches include bi- and tri-linear design curves where the slope of the curve decrease when the stress amplitudes are lower.

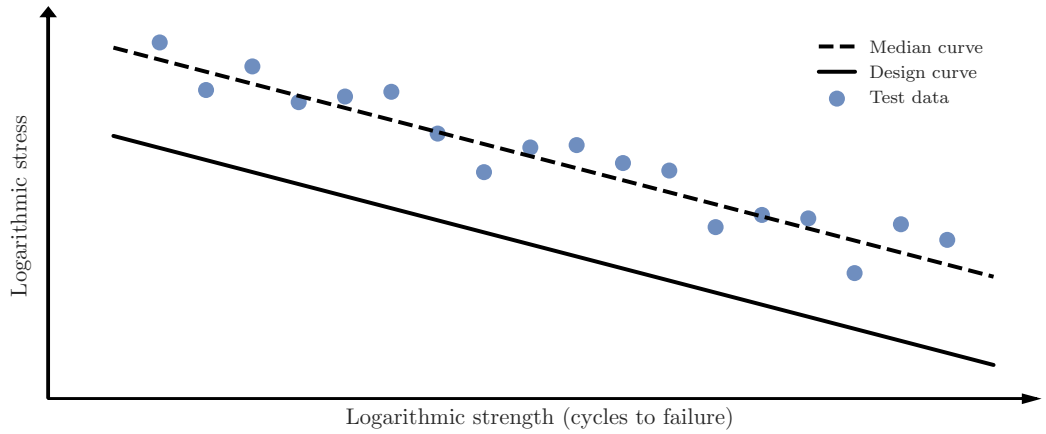

Fig. 4.3: Linear SN-curve in a logarithmic scale.

4.3.3 Strain-Based Approach

The strain-based approach to fatigue considers plastic deformation at regions where fatigue cracks are most likely to occur. Detailed information about the regions is required as the local stresses and strains are analyzed as a basis for fatigue-life predictions [32]. This approach makes use of the material's cyclic stress-strain and strain-life curves from axial test specimens to calculate the life expectancy. The use of local stresses instead of nominal or average stresses is an important

distinction between the strain- and stress-based approach. In addition, the strain-based approach considers local yielding, whereas the stress-based approach assumes elasticity. The involvement of local yielding gives improved estimates for ductile materials with short lives [32]. Apart from these two differences, they share certain concepts such as stress (or strain) versus cycles to failure curves to make life estimates. Neither approach includes analysis about crack growth, such as fracture mechanics.

4.4 Miner's Rule

SN-curves and most fatigue data are based on constant stress amplitudes. However, in practice, most fatigue stresses are random or have varying stress amplitudes. There exist several methods to estimate fatigue life based on varying stress amplitudes. However, the method named Palmgren-Miner's rule or simply Miner's rule is by far the most common approach. The method was first proposed by Palmgren in 1924 to estimate the life of roller bearers and later developed by Miner in 1945 to be applied to other structural components [13]. The method assumes that a component can withstand a given number of cycles N_i for a given stress level S_i. If the component experiences n_i cycles at this stress level, then the damage is the fraction n_i/N_i. Add all k stress levels together to receive the cumulative damage [5]

$$D = \sum_{i=1}^{k} \frac{n_i}{N_i} \tag{4.4}$$

Failure occurs when D reaches a given value. Often this value is set to 1 for simplicity. Note that with such a method of calculating the fatigue damage, the order of the cycles does not matter. An arbitrary order of cycles as shown in Fig. 4.4a will give the same damage as a sorted order of cycles with stress amplitude S_i, illustrated in Fig. 4.4b.

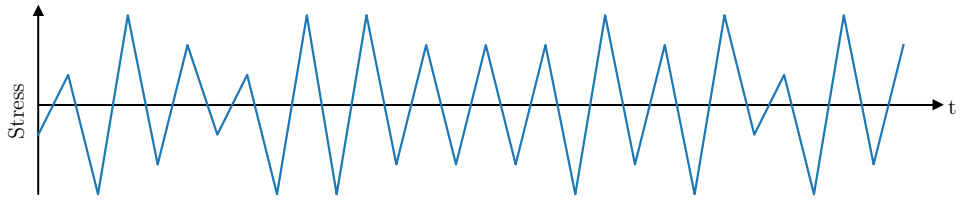

(a) Unsorted varying stress history.

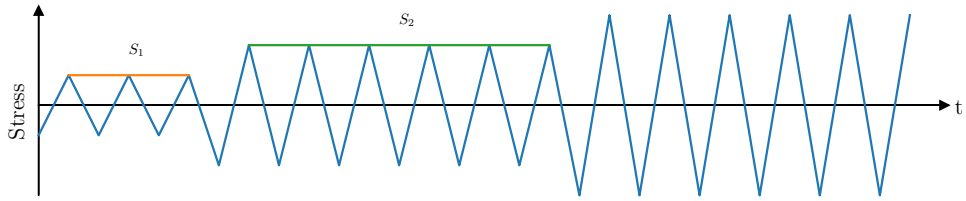

(b) Sorted varying stress history.

Fig. 4.4: Stress history for an arbitrary component.

4.5 Rainflow Counting

For a random process, such as wind or waves, the stress cycles are generally wide-banded and unsorted, as illustrated in Fig. 4.2b and Fig. 4.4a, respectively. Counting cycles in such an environment is not necessarily straightforward. Some different methods to count the cycles exist today, but the rainflow (RF) algorithm is considered to be the most accurate [33]. The rules described in this section form an algorithm that counts cycles such that they correspond to closed hysteresis loops in the stress-strain diagram [34]. The RF-algorithm can be illustrated by considering a stress history with time axis downward as shown in Fig. 4.5. The algorithm follows a set of rules to identify the cycles [5]:

1. The rain initiates from the inside of each valley and will continue until it encounters a valley more negative than the origin. In Fig. 4.5 the flow from 1 ceases since valley 3 is more negative.
2. A rainflow will cease when it meets a flow from above. The flow from 5 ceases when it encounters flow from 3 in Fig. 4.5.
3. A new path starts after the previous path has been terminated.
4. Valley generated half-cycles and the corresponding stress range S_i are logged for the record analyzed.
5. The process is repeated in reverse, but now the rainflow initiates from peaks. For a sufficiently long sample, each half-cycle will match another and form a full stress cycle.

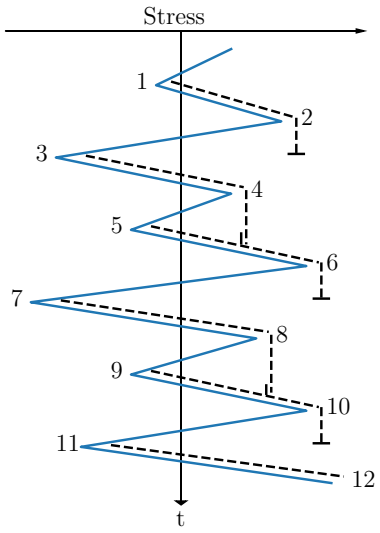

Fig. 4.5: Illustration of the rainflow algorithm.

4.6 Frequency Domain Calculation of Fatigue

Frequency domain methods for calculating the fatigue damage are more computationally efficient compared to time domain approaches. For a random fatigue analysis in the time domain, a sufficiently long time series of the structural response is needed. This can be time-consuming, especially for structures subjected to random loadings, like those produced by buffeting wind. So-called spectral methods or closed-form (CF) methods in the frequency domain have been proposed to calculate the fatigue damage directly from a stress spectrum.

In the CF-methods, the buffeting load is modeled as a wide-banded stationary Gaussian random process which is described by a spectral density. An advantage of the spectral methods is the possibility to use exact or approximate analytical formulas to relate the fatigue damage directly to the spectral density of the random process [34].

Since the rainflow algorithm is considered the most accurate counting procedure of irregular cycles, spectral methods try to find the best expression to relate the spectral density of the process to the rainflow algorithm. Due to the complexity of the rainflow algorithm, the exact expression of the probability density of rainflow cycles and the correlation between this distribution and the spectral density of the process are not present for wide-banded processes [34]. Therefore, different approaches are presented in the literature to address this problem. Some methods completely approximate the algorithm based on best fitting procedures on many simulations [13, 35, 36], while other methods use more theoretical considerations [11].

4.6.1 Regular Narrow-Banded Process

For a narrow-banded random stress $s(t)$, the total number of cycles with an amplitude in the range $(s, s+\delta s)$ is given by [10]

$$n(s) = \upsilon_0^+ T f_p(s)\delta s \tag{4.5}$$

where υ_0^+ represents the mean-upcrossing rate defined in Eq. (2.22), T is the time period and $f_p(s)$ is the probability density of peaks. Combining Eq. (4.4) and Eq. (4.5) gives the fractional damage at stress level s

$$\frac{n(s)}{N(s)} = \frac{\upsilon_0^+ T f_p(s) s^m \delta s}{K} \tag{4.6}$$

which by summation gives the total expected fractional damage over all stress amplitudes

$$D = \sum_0^\infty \frac{n(s)}{N(s)} = \frac{\upsilon_0^+ T \int_0^\infty f_p(s) s^m ds}{K} \tag{4.7}$$

Assuming a Gaussian probability distribution for the narrow-banded stress process s implies that the probability distribution of the peak $f_p(s)$ has a Rayleigh distribution equal to [20, 37]

$$f_p(s) = \frac{s}{\sigma^2} exp\left(-\frac{s^2}{2\sigma^2}\right) \tag{4.8}$$

where σ represents the standard deviation of the entire stress history. Substituting Eq. (4.8) into Eq. (4.7) gives the total damage for a strictly narrow-banded process s

$$D_{NB} = \frac{\upsilon_0^+ T}{K\sigma^2} \int_0^\infty s^{m+1} exp\left(-\frac{s^2}{2\sigma^2}\right) ds = \frac{\upsilon_0^+ T}{K} \left(\sqrt{2}\sigma\right)^m \Gamma\left(\frac{m}{2}+1\right) \tag{4.9}$$

Here, Γ represents the Gamma function given in Eq (2.35) and the stress $s(t)$ is based on amplitude. Rewriting Eq. (4.9) in terms of damage rate (i.e. damage per time unit) and stress range instead

of amplitude gives the rate of fatigue damage accumulation (FDA)

$$\overline{D}_{NB} = \frac{\upsilon_0^+}{K}\left(2\sqrt{2}\sigma\right)^m \Gamma\left(\frac{m}{2}+1\right) \tag{4.10}$$

Eq. (4.10), which provides the rate of FDA for a narrow-banded process (NB), is a valid CF-method for a single slope SN-curve. It is widely accepted that the narrow-banded approximation applied to wide-banded processes tends to overestimate the rate of FDA achieved from the RF-method [34]. Spectral methods considering wide-banded procedures are therefore presented in the following.

4.6.2 Wirsching and Light (1980)

In contrast to a narrow-banded random process, the wide-banded random process consists of contributions over a large range of frequencies [10]. Hence, Wirching and Light (WL) proposed that the rate of FDA for a wide-banded random stress variation can be estimated by [5]

$$\overline{D}_{WL} = \lambda_{WL}\overline{D}_{NB} \tag{4.11}$$

where $\overline{D}_{NB}$ represents the rate of FDA obtained by Eq. (4.10) and λ_{WL} is an empirical correction factor obtained by simulating various wide-banded processes, followed by a rainflow counting of the cycles. The correction factor λ_{WL} is given by

$$\lambda_{WL} = a(m) + (1-a(m))(1-\epsilon)^{b(m)} \tag{4.12}$$

Here, ϵ represents the spectral bandwidth parameter defined by Eq. (2.23), and the best-fitting parameters $a(m)$ and $b(m)$ are obtained by least-squares fitting

$$a(m) = 0.926 - 0.033m, \quad b(m) = 1.587m - 2.323 \tag{4.13}$$

4.6.3 Dirlik (1985)

Dirlik (DK) used a combination of an exponential and two Rayleigh distributions to fit a CF-method for the PDF of effective rainflow stress ranges [13]. By applying a large set of numerical simulations with different spectrums, Dirlik developed the following expression for the PDF of rainflow ranges r by a best-fitting procedure

$$f_{DK}(r) = \frac{1}{2\sigma}\left[\frac{D_1}{Q}exp\left(\frac{-Z}{Q}\right) + \frac{D_2 Z}{R^2}exp\left(\frac{-Z^2}{2R^2}\right) + D_3 Z exp\left(\frac{-Z^2}{2}\right)\right] \tag{4.14}$$

where the normalized parameter Z is defined by $Z = r/2\sigma$, and the parameters D_1, D_2, D_3, Q and R are given as

$$\begin{aligned} D_1 &= \frac{2(X_M - \alpha_2^2)}{1+\alpha_2^2} \quad , \quad D_2 = \frac{1-\alpha_2-D_1+D_1^2}{1-R} \quad , \quad D_3 = 1-D_1-D_2 \\ Q &= \frac{1.25(\alpha_2 - D_3 - D_2 R)}{D1} \quad , \quad R = \frac{\alpha_2 - X_M - D_1^2}{1-\alpha_2-D_1+D_1^2} \quad , \quad X_M = \frac{M_1}{M_0}\sqrt{\frac{M_2}{M_4}} \end{aligned} \tag{4.15}$$

The rainflow rate of FDA under the Palmgren-Miner rule is obtained by substituting $f_{DK}(r)$, $T = 1$ and $\upsilon_0^+ = \upsilon_p$ into Eq. (4.7), along with a simple variable transformation. The closed-form of the method becomes [7]

$$\overline{D}_{DK} = \frac{\nu_p}{K}(2\sigma)^m \left(D_1 Q^m \Gamma(1+m) + \left(\sqrt{2}\right)^m (D_2|R|^m + D_3)\Gamma\left(1+\frac{m}{2}\right)\right) \tag{4.16}$$

4.6.4 Single-Moment (1990)

Lutes and Larsen developed a single-moment method (SM) for calculating the rate of FDA. Examination of simulation data and rainflow analysis led to the following expression [14]

$$\overline{D}_{SM} = \frac{2^{3m/2}}{K}\Gamma\left(1+\frac{m}{2}\right)(M_{2/m})^{m/2} \tag{4.17}$$

which can be expressed in terms of $\overline{D}_{NB}$ and the corresponding correction factor

$$\overline{D}_{SM} = \lambda_{SM}\overline{D}_{NB}, \quad \lambda_{SM} = \frac{\left(\frac{M_{2/m}}{M_0}\right)^{m/2}}{\upsilon_0^+} \tag{4.18}$$

Here, the spectral moment $M_{2/m}$ is defined by Eq. (2.19).

4.6.5 Jiao and Moan (1990)

A bimodal Gaussian process is a special wide-banded process with a combination of a low frequency (LF) and a high frequency (HF) Gaussian process. The method proposed by Jiao and Moan (JM) is computed by applying a correction factor to the narrow-banded estimation. The estimated rate of FDA is given by [12]

$$\overline{D}_{JM} = \lambda_{JM}\overline{D}_{NB} \tag{4.19}$$

where the narrow-banded estimation $\overline{D}_{NB}$ is defined by Eq. (4.10) and the correction factor λ_{JM} is established by the sum of the HF-component and the envelope of the Gaussian process $Y(t)$. The HF-component includes all the smaller stress oscillations, while the envelope $Y(t)$ is defined by the sum of the LF-component $X_1(t)$ and the HF-component $X_2(t)$

$$Y(t) = X_1(t) + X_2(t) \tag{4.20}$$

The envelope of $Y(t)$ includes all the large stress cycles, and is approximated by

$$P(t) = X_1(t) + R_2(t) \tag{4.21}$$

where $R_2(t)$ represents the Cramer-Leadbetter envelope of $X_2(t)$ [12]. The rate of FDA due to the large cycles generated by $P(t)$ can be approximated as

$$\overline{D}_P = \frac{\upsilon_{0,P}^+}{K}(2\sqrt{2})^m \Gamma\left(1+\frac{m}{2}\right)\left[M_1^{*(\frac{m}{2}+2)}\left(1-\sqrt{\frac{M_2^*}{M_1^*}}\right)+\sqrt{\pi M_1^* M_2^*}\frac{m\Gamma\left(\frac{1}{2}+\frac{m}{2}\right)}{\Gamma\left(1+\frac{m}{2}\right)}\right] \tag{4.22}$$

The mean up-crossing rate $\upsilon_{0,P}^+$ is defined by

$$\upsilon_{0,P}^+ = M_1^* \upsilon_{0,1}^+ \sqrt{1+\frac{M_2^*}{M_1^*}\left(\frac{\upsilon_{0,2}^+}{\upsilon_{0,1}^+}\sqrt{1-\alpha_{1,2}^2}\right)^2} \tag{4.23}$$

where $\upsilon_{0,1}^+$ and $\upsilon_{0,2}^+$ represent the mean up-crossing rate of the LF- and HF-process, respectively, defined by Eq. (2.22). The bandwidth parameter $\alpha_{1,2}$ is defined by Eq. (2.21), where the subscript $(1,2)$ refers to α_1 of the HF-process. M_i^* is the normalized variance of component $X_i(t)$ defined by the variance components $M_{0,i}$

$$M_i^* = \frac{M_{0,i}}{M_{0,1}+M_{0,2}}, \quad i = 1,2 \tag{4.24}$$

The rate of FDA due to small cycles generated by the HF-process is calculated by the narrow-banded approximation

$$\overline{D}_{HF} = \frac{\upsilon_{0,2}^+}{K}(2\sqrt{2})^m M_2^{*\frac{m}{2}} \Gamma\left(1+\frac{m}{2}\right) \tag{4.25}$$

Furthermore, the correction factor λ_{JM} can then be calculated as the ratio of the approximated rainflow rate of FDA to the conservative narrow-banded approximation $\overline{D}_{Y,NB}$

$$\lambda_{JM} = \frac{\overline{D}_{Y,WB}}{\overline{D}_{Y,NB}} = \frac{\overline{D}_P + \overline{D}_{HF}}{\overline{D}_{Y,NB}} \tag{4.26}$$

where $\overline{D}_{Y,NB}$ is defined by substituting the zero upcrossing rate $\nu_{0,Y} \approx \sqrt{M_1^* {\upsilon_{0,1}^+}^2 + M_2^* {\upsilon_{0,2}^+}^2}$ and $\sigma^2 = 1$ into Eq. (4.10).

4.6.6 The Empirical $\alpha_{0.75}$ (1984)

The empirical $\alpha_{0.75}$ method (AL) was proposed by Lutes et al. [35]. On a purely empirical basis, they suggested the following simple formulation to calculate the rate of FDA

$$\overline{D}_{AL} = \alpha_{0.75}^2 \overline{D}_{NB} \tag{4.27}$$

The correlation factor is only a function of the bandwidth parameter $\alpha_{0.75}$, defined by Eq. (2.21).

4.6.7 Tovo and Benasciutti (2002)

Tovo and Benasciutti (TB) proposed a formula for calculating the wide-banded rate of FDA by using a linear combination of the narrow-banded approximation $\overline{D}_{NB}$ and the range counting method $\overline{D}_{RC}$ [11]. The method tries to accomplish an appropriate intermediate point between the lower- and upper-bound approximation of the rate of FDA, respectively $\overline{D}_{RC}$ and $\overline{D}_{NB}$. The formula is given by

$$\overline{D}_{TB} = c\overline{D}_{NB} + (1-c)\overline{D}_{RC} = (c + (1-c)\alpha_2^{m-1})\overline{D}_{NB} = \lambda_{TB}\overline{D}_{NB} \tag{4.28}$$

The weighting parameter c is based on a combination of theoretical framework and extensive numerical simulations of wide-banded processes. As a result, c is defined by

$$c = \frac{(\alpha_1 - \alpha_2)(1.112(1 + \alpha_1\alpha_2 - (\alpha_1 + \alpha_2))exp(2.11\alpha_2) + (\alpha_1 - \alpha_2))}{(\alpha_2 - 1)^2} \tag{4.29}$$

where the spectral parameters α_1 and α_2 are defined by Eq. (2.21).

Chapter 5

Procedure of Fatigue Analysis

5.1 Introduction

The theoretical foundation presented in Chapter 2-4 was combined to create a procedure for calculating fatigue damage. The procedure was applied to simple shear frames meant as a proof of concept. The models in Fig. 5.1 were studied independently in order to compare fatigue damage estimations between CF-methods in the frequency domain and the RF-algorithm combined with Miner's rule in the time domain. The procedure presented in this Chapter is used as a framework for the Langenuen bridge presented in Chapter 6.

5.2 System Description of Shear Frame

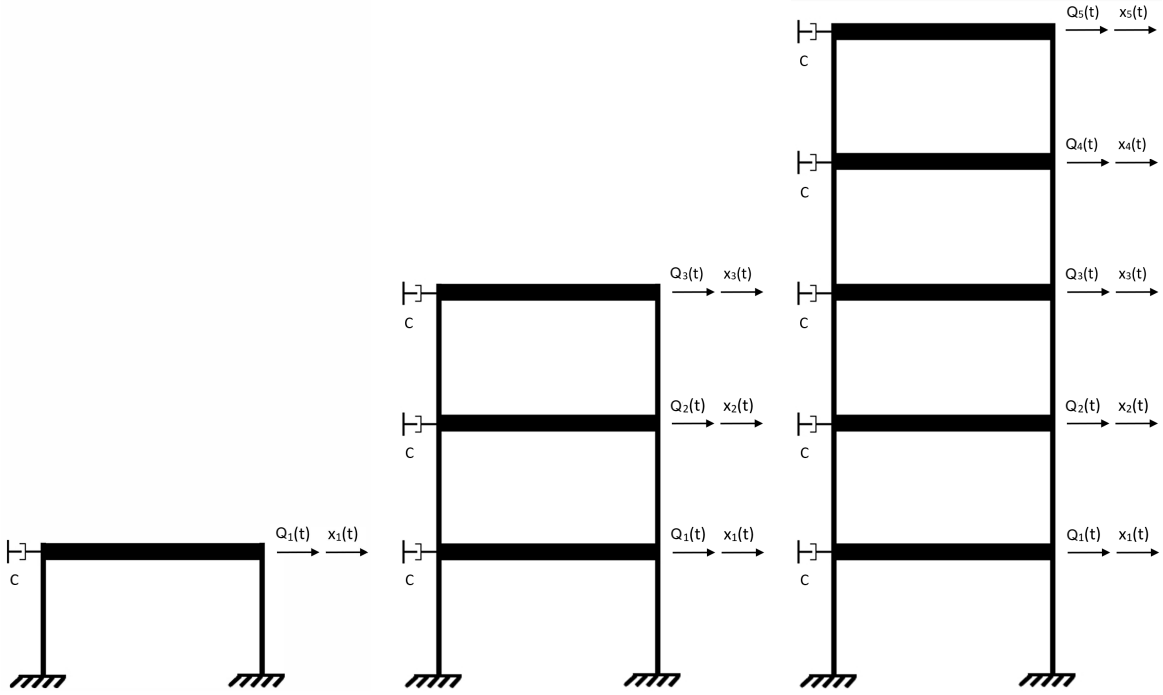

(a) 1-DOF **(b)** 3-DOF **(c)** 5-DOF

Fig. 5.1: Shear frame models.

Each model was subjected to a stochastic wind load $Q_i(t)$ in DOF i, $i \in \{1, \ldots, N_{DOF}\}$. The shear frame was modeled with N_{DOF} rigid floors between two RHS 120x120x8.0 columns of length L

and stiffness k. Each floor was modeled with lumped mass m and damping c. Only the maximum nominal stress due to bending moment was considered at the base of the structure. The parameters used to model the geometry of the shear frames are provided in Table 5.1. The SN-curve used in this analysis was based on a single slope curve with varying fatigue strength component m. Detail category 36 from Eurocode 3:1-9:2005 table 8.5 was chosen for the connection at the base of the shear frames [38]. This implies an endurance of $N = 2.0 \times 10^6$ cycles for a constant amplitude stress range $\Delta\sigma_c = 36.0N/mm^2$.

L $[m]$	m $[kg]$	c $[Ns/m]$	E $[GPa]$	I $[m^4]$	W $[m^3]$	k $[N/m]$
5.00	10000	1000	210	7.38×10^{-6}	123×10^{-6}	$12EI/L^3$

Table 5.1: Parameters used in the simplified geometry of the shear frame.

5.3 Procedure and Analysis

5.3.1 Stress Spectrum

The spectrum recommendation from the Norwegian handbook for bridge design, N400 [26], was used to provide the auto- and cross-spectral density for the stochastic wind turbulence. The auto-spectrum used in this analysis is given by Eq. (2.40), where the along-wind direction u with identical auto-spectrums $G_u(f)$ for each DOF have been studied. The cross-spectral density $G_{uu}(\Delta s, f)$ for the 3- and 5-DOF shear frame in Fig. 5.1b and 5.1c was modeled according to Eq. (2.39), with the normalized co-spectrum function $\hat{Co}_{uz}(\Delta s, f)$ proposed by Davenport. As a result, the cross-spectral density reads

$$G_{uu}(\Delta s, f) = G_u(f) exp\left(-C_{uz} \frac{f \Delta s}{U} \right) \tag{5.1}$$

where an increase in frequency f and distance Δs decreases the correlation. The decay coefficient C_{uz} and the spectral parameter A_u were assumed to be constant. The distance $\Delta s = L = 5.00m$ represents the vertical distance z between each DOF, u the turbulence component in the along-wind direction x, and U represents the mean along-wind velocity. An illustration of the normalized auto-spectrum and cross-spectrum with input parameters according to Table 5.2 in addition to mean wind velocity $U = 10.0m/s$ is shown in Fig. 5.2.

ρ $[kg/m^3]$	C_D $[-]$	${}^xL_u$ $[m]$	A_u $[-]$	C_{uz} $[-]$	A $[m^2]$
1.25	1.00	150	6.80	10.0	5.00

Table 5.2: Wind parameters for the shear frame.

The concentrated wind load in DOF i was modeled as a function of air density ρ, relative velocity

$v_{i,rel}$, exposed area A and drag coefficient C_D

$$Q_i(t) = \frac{1}{2}\rho v_{i,rel}^2 A C_D \tag{5.2}$$

where the relative velocity is given by

$$v_{i,rel} = U + u(t) - \dot{x}_i(t) \tag{5.3}$$

The mean wind U and the along-wind turbulence $u(t)$ were assumed equally distributed along the shear frame, whereas the velocity $\dot{x}_i(t)$ varies in time and DOF i. Neglecting higher order terms and disregarding the static term the equation of motion reads

$$\boldsymbol{M}\ddot{\boldsymbol{x}}(t) + (\boldsymbol{C} + \rho U A C_D \boldsymbol{I})\dot{\boldsymbol{x}}(t) + \boldsymbol{K}\boldsymbol{x}(t) = \rho U A C_D \boldsymbol{u}(t) \tag{5.4}$$

where $\boldsymbol{M} = \text{diag}(m_1, \ldots, m_{N_{DOF}})$, $\boldsymbol{C} = \text{diag}(c_1, \ldots, c_{n_{DOF}})$ and the identity matrix $\boldsymbol{I} = \boldsymbol{I}_{N_{DOF}}$. The along-wind turbulence vector $\boldsymbol{u}(t) \in \mathbb{R}^{N_{DOF}}$ is given by

$$\boldsymbol{u}(t) = u(t)\begin{bmatrix} 1 & \ldots & 1 \end{bmatrix}^T \tag{5.5}$$

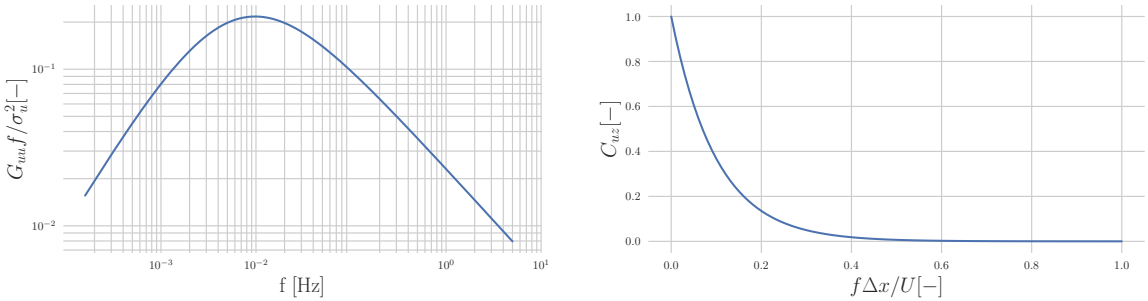

(a) Auto-spectrum with $U = 10.0m/s$. **(b)** Normalized cross-spectrum with $C_{uz} = 10.0$.

Fig. 5.2: Auto-spectrum and normalized cross-spectrum of the turbulence component u.

The correlation function of the wind load can be expressed in time domain as

$$\boldsymbol{R}_{QQ}(\tau) = E\left[\boldsymbol{Q}(t)\boldsymbol{Q}^T(t+\tau)\right] = (\rho U A C_D)^2 \boldsymbol{R}_{uu}(\tau) \tag{5.6}$$

A Fourier transform of Eq. (5.6) gives the corresponding one-sided load spectrum $\boldsymbol{G}_{QQ}(\omega)$, which in combination with the frequency response function $\boldsymbol{H}(\omega)$ expresses the response spectrum

$$\boldsymbol{G}_{xx}(\omega) = \overline{\boldsymbol{H}}(\omega)\boldsymbol{G}_{QQ}(\omega)\boldsymbol{H}(\omega)^T \tag{5.7}$$

where $\boldsymbol{H}(\omega)$ is expressed by

$$\boldsymbol{H}(\omega) = \left[-\omega^2 \boldsymbol{M} + i\omega[\boldsymbol{C} + \rho U A C_D \boldsymbol{I}] + \boldsymbol{K}\right]^{-1} \tag{5.8}$$

The stress spectrum $G_{\sigma\sigma}(\omega)$ at the base of the structure can be obtained by applying a transfer function $\boldsymbol{T} \in \mathbb{R}^{N_{DOF}}$, such that

$$G_{\sigma\sigma}(\omega) = \boldsymbol{T}\boldsymbol{G}_{xx}(\omega)\boldsymbol{T}(\omega)^T \tag{5.9}$$

where the transfer vector $\boldsymbol{T}$ is given by

$$\boldsymbol{T} = \frac{6EI}{WL^2}\begin{bmatrix}1 & 0 & \dots & 0\end{bmatrix}^T \tag{5.10}$$

An illustration of $G_{\sigma\sigma}(f)$ is shown in Fig. 5.3-5.4, where the relation $G_{\sigma\sigma}(f) = 2\pi G_{\sigma\sigma}(\omega)$ is used.

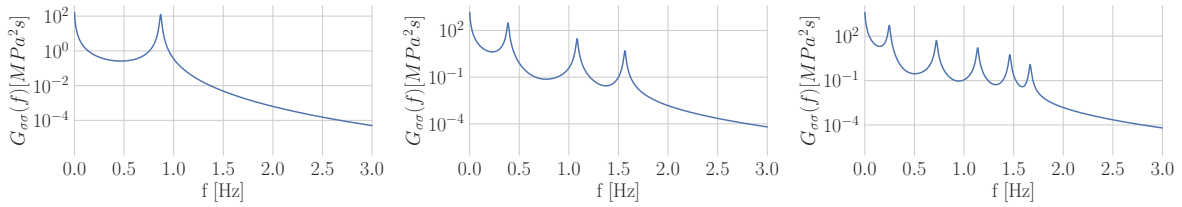

(a) 1-DOF **(b)** 3-DOF **(c)** 5-DOF

Fig. 5.3: Stress spectrums including background response for a mean wind $U = 10.0m/s$ and standard deviation of the turbulence component $\sigma_u = 2.00m/s$ at the base for the shear frames.

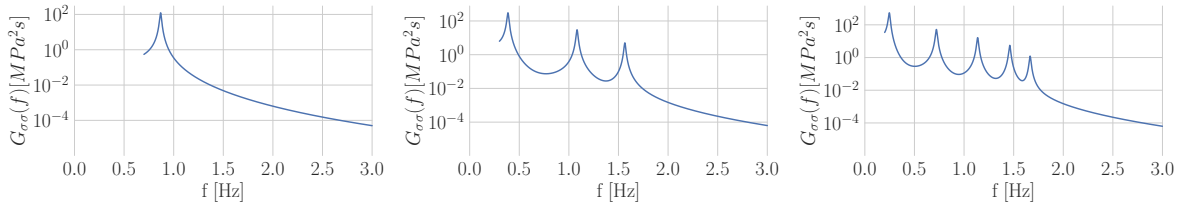

(a) 1-DOF **(b)** 3-DOF **(c)** 5-DOF

Fig. 5.4: Stress spectrums excluding background response for a mean wind $U = 10.0m/s$ and standard deviation of the turbulence component $\sigma_u = 2.00m/s$ at the base for the shear frames.

5.3.2 Wind Field Modeling

Fenereci and Øiseth [25] found an expression for the lognormal distribution of the standard deviation of the turbulence at the Hardanger bridge in Norway. For the analysis of the shear frames, the expression found from the east was used, and it is given as

$$\tilde{\mu} = 0.122 + 0.039U, \qquad \tilde{\sigma} = 0.2566 \tag{5.11}$$

where $\tilde{\mu}$ and $\tilde{\sigma}$ are the mean and standard deviation of the distribution. A Weibull distribution with $k = 1.795$ and $c = 5.194$ was used to describe the PDF for the mean wind, also fitted to measurements from the Hardanger bridge [39]. A joint PDF for mean wind U and standard deviation for the turbulence σ_u can then be established [40]

$$f(U, \sigma_u) = f(U) f(\sigma_u |\, \tilde{\mu}, \tilde{\sigma}) \tag{5.12}$$

where $f(U)$ describes the Weibull distribution of the mean wind U and $f(\sigma_u |\, \tilde{\mu}, \tilde{\sigma})$ describe the lognormal distribution of the standard deviation of the turbulence component u according to Eq. (2.32) and Eq. (2.37), respectively. The joint PDF is visualized in Fig. 5.5.

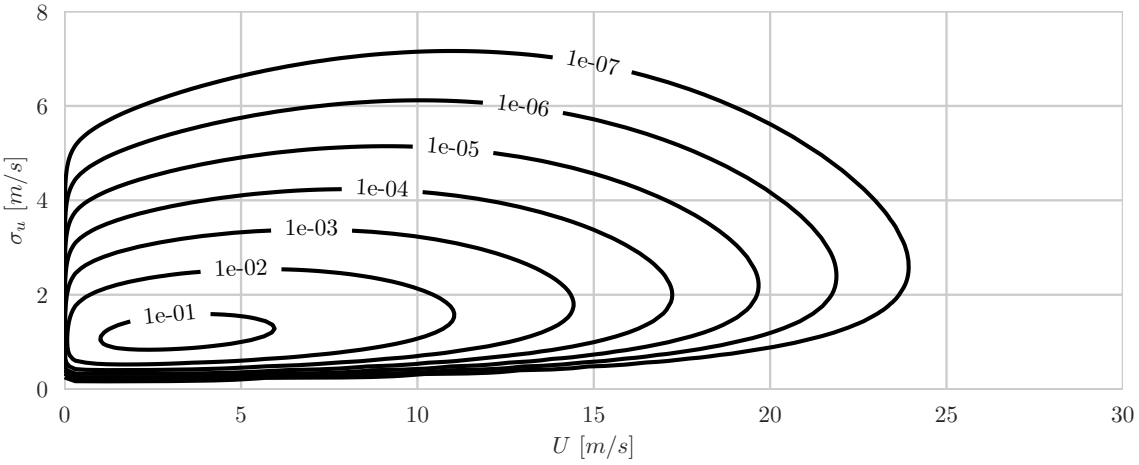

Fig. 5.5: Contour plot of the joint PDF for the mean wind velocity and the standard deviation of the turbulence along-wind.

5.3.3 Sequential Updating Approach

A Gaussian process regression was used in a sequential updating approach, as illustrated in Fig. 5.6, to estimate the rate of fatigue damage accumulation (FDA). The algorithm was given an initial training data set with only one set of the model parameters U and σ_u. The surrogate model of the Gaussian process was then improved by sequentially adding points to the training data. The learning function chose which points to add and is defined as

$$\boldsymbol{W}_{t,next} = argmax \left\{ \hat{\boldsymbol{\sigma}}^{(1-n)} \left[\hat{\boldsymbol{D}}_{pred}\, f(\boldsymbol{U}, \boldsymbol{\sigma}_u) \right]^n \right\} \tag{5.13}$$

where $\hat{\boldsymbol{D}}_{pred}$ is a normalized vector that represents the surrogate model for the fatigue damage. $\hat{\boldsymbol{\sigma}}$ is a normalized vector containing the standard deviations of the surrogate model and should not be confused with the standard deviation of the turbulence σ_u. $f(\boldsymbol{U}, \boldsymbol{\sigma}_u)$ is the joint PDF given in Eq. (5.12) and n is a parameter that can be adjusted to control the weighting between $\hat{\boldsymbol{\sigma}}$ and $\hat{\boldsymbol{D}}_{pred}$.

Larger n-value prioritizes $\hat{\boldsymbol{D}}_{pred}$ and will provide a higher density of points around the critical peak. Smaller n will, on the contrary, provide more exploration and a larger spread of the calculated points. In this analysis $n = 0.15$ was used. The learning function is based on the formulation of Gramstad et al. [16]. The most important deviance from the procedure proposed by Gramstad et al. is that the vectors $\hat{\boldsymbol{D}}_{pred}$ and $\hat{\boldsymbol{\sigma}}$ in the learning function are normalized, and the length scales in the squared exponential kernel are fixed. Also, Gramstad et al. used the sequential updating process to estimate extreme response and not fatigue. Note that the choice of the first point was not critical to achieving a satisfactory result as the algorithm quickly located the peak and prioritized points nearby. This is illustrated in Fig. 5.6 where the initial point ($U = 10.0m/s,\ \sigma_u = 2.00m/s$) is clearly not in the center of the peak and hence not the most critical.

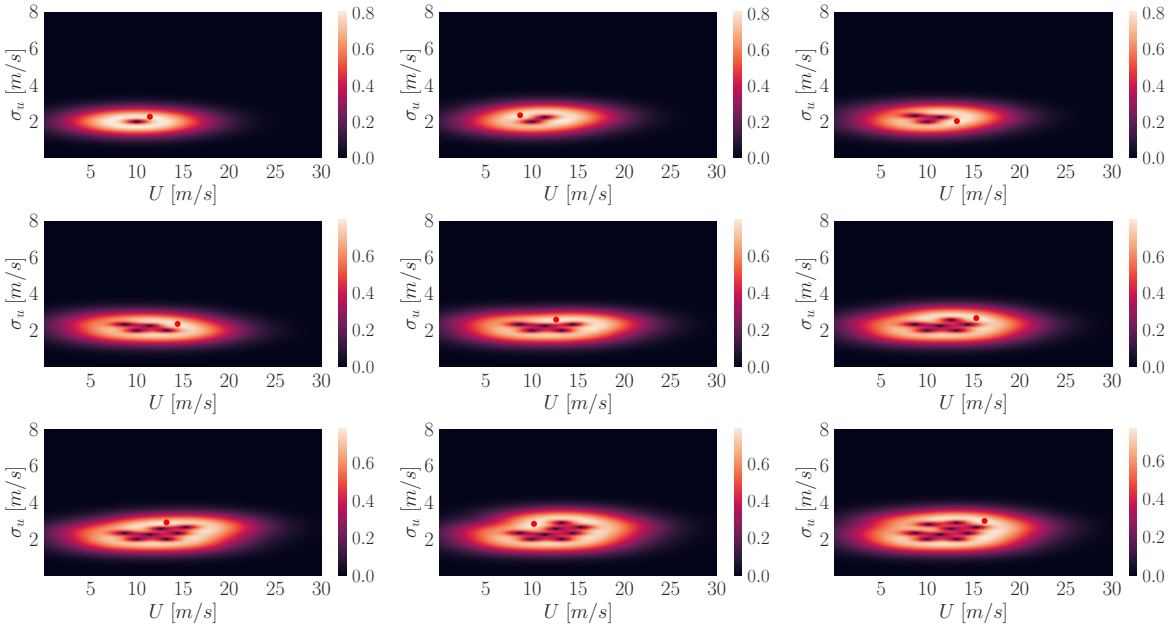

Fig. 5.6: The learning function is visualized for the first nine iterations for $m = 5$ and 1-DOF. The maximum value and next point is marked as a red dot.

5.3.4 Procedure of Fatigue Damage Evaluation

The essence of the procedure is to sequentially sample data, i.e. the fatigue damage multiplied by its probability of occurrence, and use GPR to predict the unknown values. When a sufficient amount of training data has been sampled, the rate of FDA can be calculated by a numerical integration of the surrogate model over the mean wind velocity U and the standard deviation of the turbulence σ_u as shown in Eq. (5.14).

$$\overline{FDA} = \int_U \int_{\sigma_u} D_{pred}(U, \sigma_u)\, f(U, \sigma_u) d\sigma_u dU \tag{5.14}$$

The entire procedure to estimate the rate of FDA and finally perform the comparison was implemented in Python [41]. The CF-methods were implemented directly from the equations derived in Section 4.6, while the Python library Fatpack [42] was used for the RF-algorithm and Miner's rule. The library Scikit [43] was used for implementation of the code related to the GPR. The RF-algorithm counts closed hysteresis loops in a stress-strain diagram by considering the stress history. A Monte Carlo (MC) simulation of the stress spectrum based on the inverse fast Fourier transform was used to obtain the stress history from the base of the shear frame. In this analysis, the frequency resolution was set to $\Delta\omega = 0.00010 rad/s$, whereas the stress history was simulated over 60 minutes with a resolution of $\Delta t = 0.10 s$.

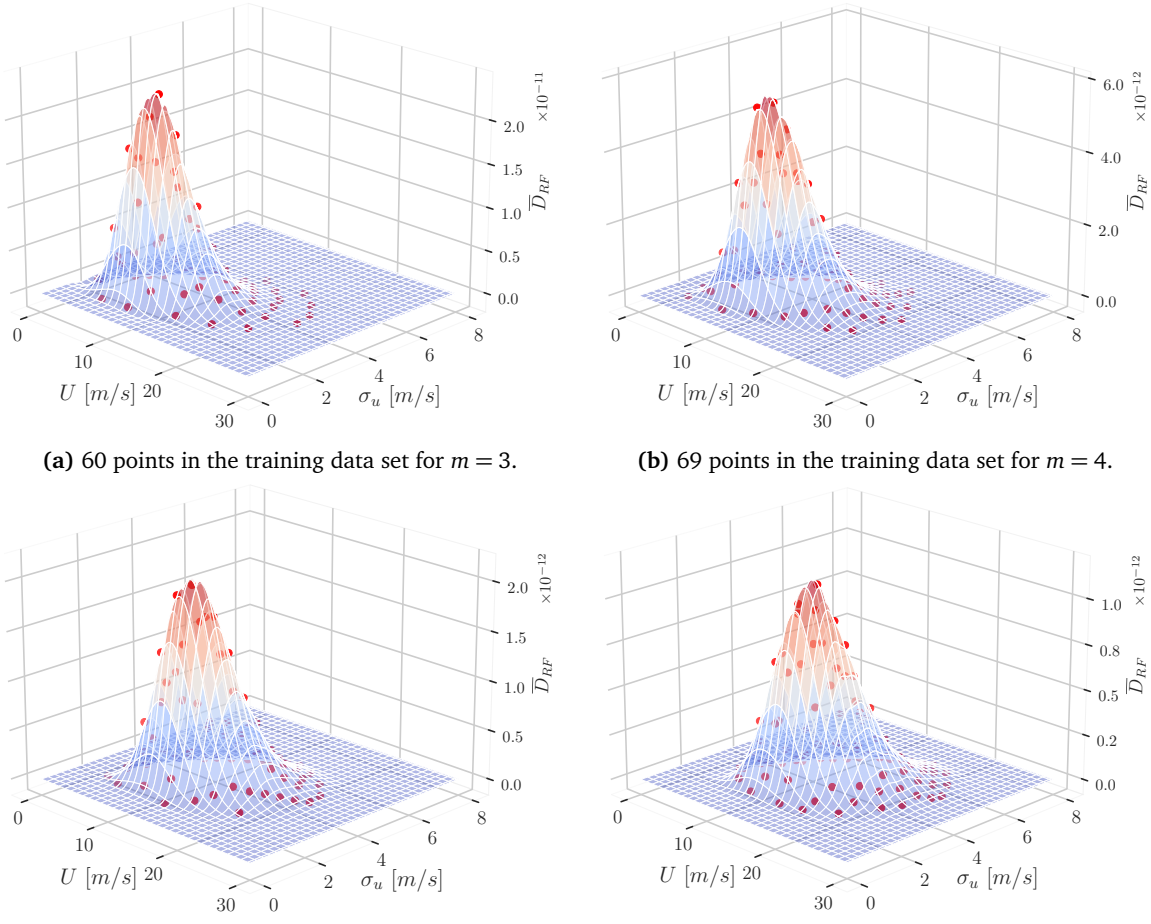

(a) 60 points in the training data set for $m = 3$.

(b) 69 points in the training data set for $m = 4$.

(c) 70 points in the training data set for $m = 5$.

(d) 87 points in the training data set for $m = 6$.

Fig. 5.7: Surrogate models for four different training data sets and m-values. The training data set is visualized as scattered red dots.

The CF-methods estimate the rate of FDA based on the stress spectrums directly. They will give the same estimation every time for a given stress spectrum. The fatigue damage obtained from the RF-algorithm and Miner's rule was averaged over 60 MC simulations to get sufficient accuracy.

However, this process had to be repeated for every point in the training data set used in the GPR. The shear frame analysis itself was computational inexpensive, making the repetitive MC simulations and RF-counting the bottleneck.

The algorithm in Section 5.3.3 will continue until terminated by a specified number of points or another termination criteria. In this analysis, the algorithm was terminated if the rate of FDA did not change more than 1‰ by performing five successive iterations of the sequential updating approach. The choice of convergence criterion and value of the n parameter is discussed and justified in Section 5.3.6. It was assumed that the training data set found by the learning algorithm could be applied to the RF-method and all the CF-methods for a given m-value and a specified number of DOFS. By this assumption, the training data set found by using the RF-method as the fatigue damage predictor could be applied to the other methods to reduce the computational cost of the analysis. This assumption was tested and is discussed in Section 5.3.5. However, for higher m-values, the critical peak seems to move towards higher values of U and σ_u, as seen in Fig. 5.7. Hence, it was necessary to repeat the sequential updating approach for all the different m-values in the analysis to find optimal training data sets for the surrogate models. A very simplified explanation of the iterative process is presented in Algorithm 1.

Algorithm 1: Calculate rate of FDA

initialize parameters
for *every m* **do**
  define kernel with fixed length scales
  initialize training data set $U = 10.0,\ \sigma_u = 2.00$
  while *surrogate model not converged* **do**
    # Using latest point $(U,\ \sigma_u)$
    create $G_{\sigma\sigma}(\omega)$
    find damage from CF-methods (D_{CF})
    for *every MC* **do**
      create stress history
      find stress ranges
      find RF damage from Miner (D_{RF})
    add D_{RF} averaged over all MC to training data values
    # Sequential updating process
    predict $\boldsymbol{D}_{pred}$ and $\boldsymbol{\sigma}$ from updated training data set
    normalize $\hat{\boldsymbol{D}}_{pred}$ and $\hat{\boldsymbol{\sigma}}$
    nextPoint $= argmax\left\{\hat{\boldsymbol{\sigma}}^{(1-n)}\left[\hat{\boldsymbol{D}}_{pred}\ f(\boldsymbol{U},\boldsymbol{\sigma}_u)\right]^n\right\}$
    add nextPoint $(U,\ \sigma_u)$ to training data set
  numerical integration to find rate of FDA for RF
  create surrogate models for all CF-methods with same training data
  numerical integration to find rate of FDA for all CF-methods

5.3.5 Damage Prediction in the Learning Function

Since the learning function in Eq. (5.13) contain a fatigue damage prediction $\hat{\boldsymbol{D}}_{pred}$, the choice of damage predictor may influence the final training data set. The sequential updating approach can be repeated for each method, creating a unique training data set to achieve the most accurate rate of FDA as possible. However, for multiple analyses, this repetitive process becomes computationally expensive. We assumed that one training data set could be used for all methods, which significantly reduced the calculations' complexity. Fig. 5.8 displays a comparison between two training data sets obtained by the use of the RF- and NB-methods as damage predictors. Some points match exactly, while others deviate depending on which method was used. Both sets seem to approximately cover the same area, indicating that the shapes of the two surrogate models are similar. The most important result for the shear frame analyses is the rate of FDA or the volume under the surrogate model. Table 5.3 displays the rate of FDA converted to years for the two data sets. The life expectancy of the CF-methods is about 0.2% lower with the NB training data set. Compared to other uncertainties such as the size of the training data set and convergence of the

MC simulations, this error was assumed small. The RF-method is around 0.65% lower with the NB data set. The increase in relative error from the CF-methods can be caused by minor differences in the MC simulations. The numbers from Table 5.3 confirm that the shapes of the surrogate models are very similar for all the methods. The scaling of the shape will separate the rate of FDA, and thus one training data set should give accurate results for all methods.

	NB	WL	DK	JM	SM	TB	AL	RF
RF data set	634.2	830.1	1122.0	593.7	997.6	1128.2	836.1	1116.1
NB data set	633.1	828.6	1120.2	592.6	995.9	1126.3	834.7	1108.8

Table 5.3: Expected life in years for data sets found by using the RF- and NB-methods as fatigue damage predictors in the sequential updating approach.

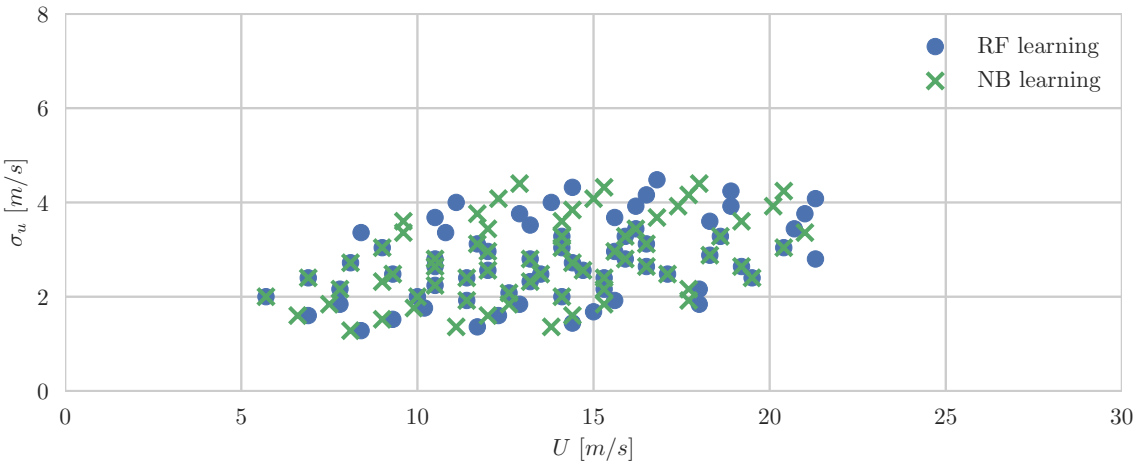

Fig. 5.8: A comparison between the training data sets found by the RF- and NB-methods as fatigue damage predictors for $m = 5$ and 1-DOF. Both sets contain 70 points.

5.3.6 Convergence of the Surrogate Model

The learning function in Eq. (5.13) determines which points are to be sampled in the next iteration. The first iterations will change the surrogate model significantly. Large changes of the surrogate model give large variations in the rate of FDA and thus the expected life of the structure. As the training data set increases, the surrogate model should provide an increasingly better estimate of the fatigue damage and finally converge. The termination criterion decides how accurate the rate of FDA has to be before the sequential updating approach is terminated. Since the exploration will increase with the n parameter, the choice of its value will also affect the rate of FDA. In Table 5.4 the 1-DOF system with $m = 5$ is simulated for several termination criteria and n-values. More iterations should provide a more accurate solution but comes at greater computational complexity than fewer iterations. The chosen values should provide a sufficiently accurate solution without

unnecessary iterations. In Table Table 5.4, the estimated life is probably most accurate with $n = 0.25$ and a termination criterion of 0.01. However, this solution has used a training data set of 150 very closely spaced points, as illustrated in Fig. 5.9b.

	n = 0.05		n = 0.10		n = 0.15		n = 0.20		n = 0.25	
Termination criteria [‰]	L	Y	L	Y	L	Y	L	Y	L	Y
0.01	83	1090	112	1086	117	1080	146	1080	150	1079
0.10	61	1092	97	1079	86	1079	121	1079	148	1079
1.00	65	1085	61	1089	86	1079	67	1085	97	1080
5.00	40	1111	38	1134	47	1111	58	1102	43	1156
10.00	36	1106	38	1124	39	1135	46	1130	38	1168
25.00	31	1140	30	1163	34	1142	37	1152	38	1177
50.00	18	1331	29	1165	31	1273	24	1296	31	1249
100.00	17	1283	21	1272	20	1318	20	1369	23	1335

Table 5.4: RF-analysis for 1-DOF with $m = 5$. L = Length of the training data set, Y = Estimated lifetime in years.

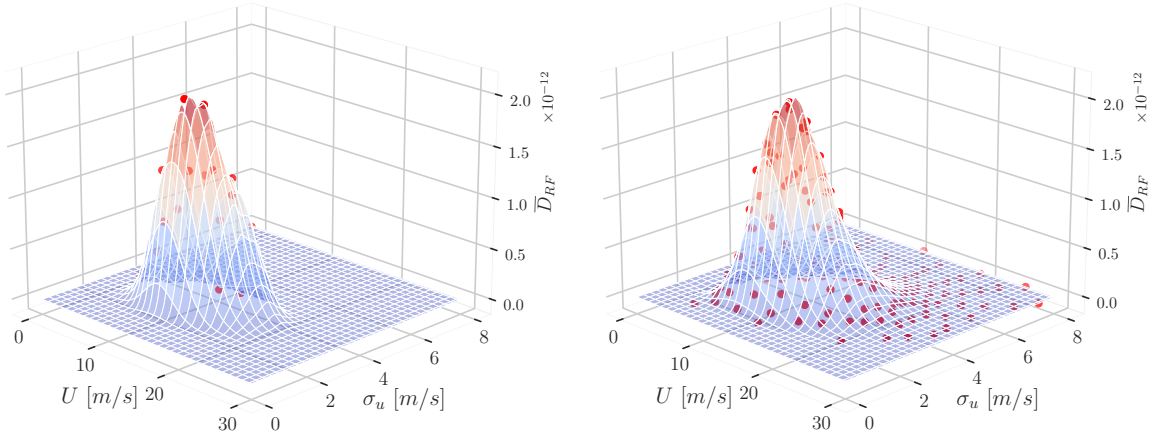

(a) 17 points as training data set

(b) 150 points as training data set

Fig. 5.9: Two different surrogate models for a RF-analysis with 1-DOF and $m = 5$.

Compared to some of the other solutions with around half the amount of points, the difference in estimated life is neglectable. However, if the training data set is too small, the estimated life is significantly overestimated. Given the assumption that the training data set of 150 points is the most accurate, all other models predict a lifetime that is non-conservative. For the analyses performed in this thesis, these non-conservative surrogate models should not affect the comparisons considerably. This is because the same training data set is used on the RF-method and all CF-methods. By using e.g. $n = 0.05$ and a termination criterion of 100‰, every method will overestimate the expected life of the structure but they are still comparable to each other. The solution for this particular choice of parameters is illustrated in Fig. 5.9a. It is obvious that by using a small training

data set, the surrogate model is not able to predict the shape of the surface sufficiently. If the goal in an analysis is to simply predict the expected life of a structure as accurately as possible, the length of the training data set is of greater importance. The choice of $n = 0.15$ and a termination criterion of 1‰ was considered accurate enough for this comparison. Table 5.4 and Fig. 5.9b indicate that extending the data set above 100 points has a negligible effect on the rate of FDA, as the model has already converged.

5.3.7 Uncertainties in the Surrogate Model

The non-conservative surrogate models discussed in Section 5.3.6 may be a source of error in estimating the expected life of the shear frame. Regarding the comparison between the RF- and CF-methods, there are other errors that may be more influential. The randomness in the MC simulation being one of them. Even with a simulation over 60 minutes and averaged over 60 MC simulations, the results will not be identical for each simulation. This will only affect the RF-method as the CF-methods estimate the fatigue damage based on the stress spectrum directly. The 60 minutes and 60 MC simulations were chosen because they provide reasonably accurate estimations without a massive computational cost.

As mentioned in Section 5.3.3, the length scales were fixed during the training process of the GPR. Automatic fitting of the length scales in Eq. (3.4) were tested in the process but gave varying results. Since the shapes of the surrogate models were very similar for every analysis, we quickly found a set of length scales that gave expected results. With too large length scales, the surrogate model underestimates the actual correlation, which gives useless results. Too small length scales may, on the other hand, cause false fluctuations to the shape. The choice of length scales also affect how closely spaced the points in the training data set are. Since this system is very simple and easy to solve, smaller length scales were used, and thus more points were added to the training data set. Since the length scales affect the training data set, the results obtained in Table 5.4 are not directly applicable for the analysis of the Langenuen bridge in Chapter 6. Naturally, a universal set of parameters that works on both the simple shear frames and the more complex Langenuen bridge would simplify the procedure. We found, however, that the length scales, n-parameter and termination criterion should be fitted for each analysis based on analytic complexity and required accuracy. We chose to fix the length scales and adjust the n-parameter and termination criterion afterwards. The choice of the length scales becomes an extra factor that can drastically change the surrogate model if not set accurately enough. Since the GPR in this thesis is performed in two dimensions, the surrogate model is very easy to visualize, and potential errors can be addressed.

Another source of error can be the choice of a suitable kernel. The squared exponential kernel from Eq. (3.4) used in this analysis is infinitely differentiable. An infinitely differentiable kernel results in a Gaussian process that has mean square derivatives of all orders and is very smooth [28].

According to Stein [44], such a smooth surrogate model is unrealistic for a physical process. Stein instead recommended the Matérn kernel, which is provided in Eq. (3.5). The ν-parameter can be adjusted to reduce the smoothness of the resulting surrogate model. In Table 5.5 and 5.6 the squared exponential kernel is compared to two Matérn kernels with smoothness $\nu = 3/2$ and $\nu = 5/2$. Apart from this, all three kernels have fixed length scales with 2.0 in U-direction and 0.2 in σ_u-direction. The signal variance σ_f^2 is automatically tuned by Scikit [43] and works as scaling for the three kernels. There are clearly some small differences in the expected life of the different systems depending on which kernel is being used. Compared to the two Matérn kernels, the squared exponential provides a more conservative estimate on the expected life of the structure for all the systems. Even though the difference between the kernels are small, this shows that the choice of the kernel can affect the rate of FDA. Table 5.6 shows how large the training set has to be to obtain a converged surrogate model. The sizes of the training data sets vary a lot more than the expected lives, but there are no clear pattern on which kernel converges faster. Since the squared exponential has been used in similar analyses [15] and provides slightly conservative estimations compared to the Matérn kernels, it was chosen for the comparisons in this thesis.

	1-DOF				3-DOF				5-DOF			
m	3	4	5	6	3	4	5	6	3	4	5	6
K_{se}	129	461	1078	1770	40.9	68.4	72.5	52.4	20.3	22.0	14.8	6.84
$K_{Mat,\nu=3/2}$	130	471	1106	1816	41.0	69.4	74.1	53.4	20.5	22.6	15.0	7.00
$K_{Mat,\nu=5/2}$	132	468	1117	1779	41.1	69.4	73.6	52.9	20.4	22.1	15.3	6.92

Table 5.5: Expected life for the three shear frames with different m-values in years with the RF-method.

	1-DOF				3-DOF				5-DOF			
m	3	4	5	6	3	4	5	6	3	4	5	6
K_{se}	59	69	79	75	53	80	85	84	71	74	87	82
$K_{Mat,\nu=3/2}$	85	70	79	78	72	82	83	82	76	58	117	81
$K_{Mat,\nu=5/2}$	46	70	62	79	66	75	80	84	74	91	63	82

Table 5.6: Size of the training data set when the convergence criterion of 1 ‰ was fulfilled with the RF-method.

5.4 Results and Discussion Shear Frame

Results presented in Section 5.4.1, 5.4.2 and 5.4.3 give an insight in the estimated rate of FDA of each shear frame from Fig. 5.1. A total of 6 different analyses have been performed. Two for each shear frame with various frequency ranges from the stress spectrum. Only 3 of the analyses will be discussed here, one for each shear frame. The selected analyses include a 1-DOF shear frame with a stress spectrum in frequency range $f \in [0.7-5.0]Hz$, a 3-DOF shear frame with $f \in [0.3-5.0]Hz$ and a 5 DOF shear frame with $f \in [0.0-5.0]Hz$. After analyzing the three specified cases, an overview of the relative error in relation to spectral bandwidth is presented in Section 5.4.4. As mentioned in Section 4.5, the RF-algorithm in combination with Miner's rule is considered to be the most accurate method to estimate the rate of FDA. The RF-method was therefore used as a benchmark in the comparison of the rate of FDA estimations obtained from CF-estimation $\overline{D}_{CF,i}$. The relative error (RE) was calculated as

$$RE = \frac{\overline{D}_{CF,i} - \overline{D}_{RF}}{\overline{D}_{RF}} \tag{5.15}$$

where the rate of FDA obtained from the CF-method $\overline{D}_{CF,i}$ and the rainflow method $\overline{D}_{RF}$ were calculated according to Eq. (5.14). The CF-estimations of $\overline{D}_{CF,i}$ are represented by narrow band (NB), Wirsching and Light (WL), Dirlik (DK), Jiao and Moan (JM), single-moment (SM), Tovo and Benascutti (TB) and $\alpha_{0.75}$ (AL).

5.4.1 Single Degree of Freedom System

The relative error of the CF-methods compared to the RF-method is illustrated in Fig. 5.10 with corresponding numerical values in Table 5.7. Any deviations of the ordinate of Fig. 5.10 indicate inaccuracies in the CF-methods. Positive values indicate an overestimation of the rate of FDA and correspond to a conservative result, while negative values signify non-conservative estimations. The results are based on a unimodal PSD as illustrated in Fig. 5.4a, evaluated over a frequency range $f \in [0.7-5.0]Hz$. In addition to the unimodal shape of the stress spectra, the narrow-banded characteristic is confirmed by a small varying spectral bandwidth parameter with a mean value equal to $\bar{\varepsilon} = 0.125$. According to Fig. 5.10, the estimations obtained by the NB-, DK-, SM-, TB- and AL-methods give comparable fatigue damage estimations, mainly in the range $RE \in [0.05, 0.11]Hz$ on the conservative side. The estimation from JM, which is based on a bimodal Gaussian process, stands out with additional conservative results while the WL-method gives non-conservative estimations relative to the RF. The relative error tends to increase along with the m-value, which is somewhat predictable because a higher m-value gives rise to a more sensitive RF-method and higher order effects of the CF-methods. Similar results were found by Benascutti and Tovo, and Mršnik et al. [34, 45].

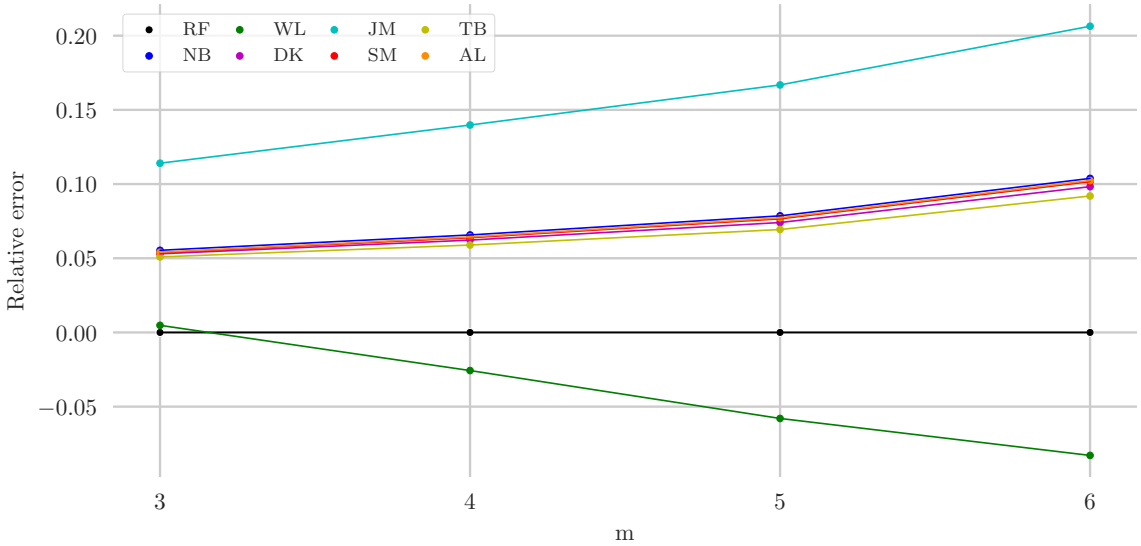

Fig. 5.10: Relative error of the rate of FDA in the 1-DOF shear frame. $f \in [0.7-5.0]Hz$.

m	NB	WL	DK	JM	SM	TB	AL
3	0.055	0.005	0.053	0.114	0.054	0.051	0.054
4	0.066	-0.026	0.062	0.140	0.064	0.059	0.064
5	0.079	-0.058	0.074	0.167	0.077	0.069	0.077
6	0.104	-0.083	0.098	0.206	0.102	0.092	0.102

Table 5.7: Relative error of the rate of FDA in the 1-DOF shear frame. $f \in [0.7-5.0]Hz$.

As mentioned in Section 4.6.5, JM estimates the fatigue damage by evaluating a LF- and HF-component of the stress spectrum. The PSD of this system consists of one peak at a frequency $f = 0.87Hz$, which corresponds to the natural frequency of the system. Due to lack of a bimodal PSD of the system, the LF-component was calculated in the frequency range $f \in [0.7, 1.5]Hz$, while the HF-component covers $f \in \langle 1.5, 5.0]Hz$. This frequency division gives raise to a large normalized variance of the LF-component, M_1^*, which in combination with small $\upsilon_{0,2}^+/\upsilon_{0,1}^+$ results in a correction factor $\lambda_{JM} > 1.0$. This coincides with the results presented in Fig. 5.10, where the JM-method overestimates the rate of FDA for all the evaluated m-values.

A $10min$ sample of a random stress simulation at the base of the 1-DOF system confirms that the process is fairly narrow-banded. As Illustrated in Fig. 5.11, about every peak of the stress simulation is followed by a new stress cycle. Here, the stress simulation was calculated with wind parameters according to Table 5.2 in addition to mean wind $U = 10.0m/s$ and a standard deviation of the turbulence component $\sigma_u = 2.00m/s$.

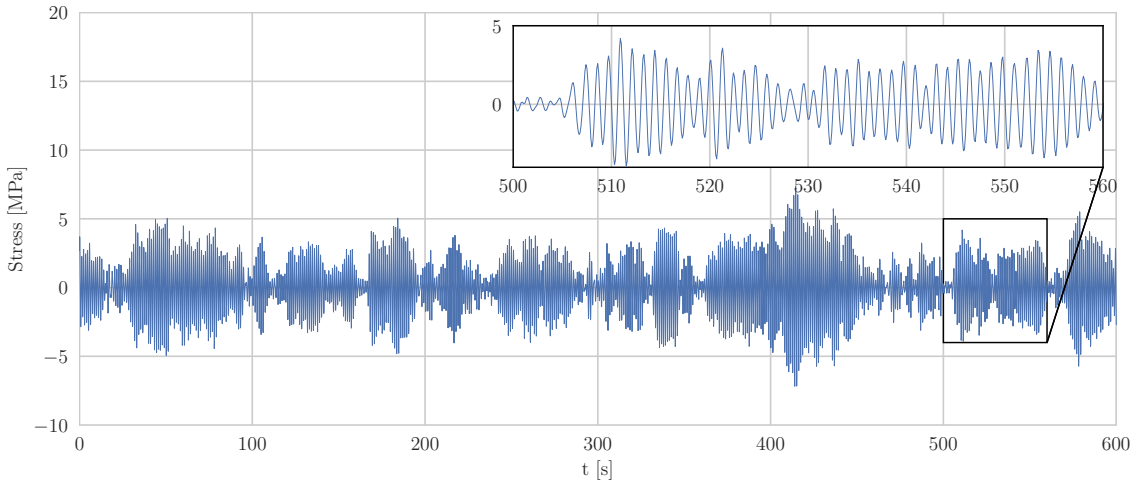

Fig. 5.11: Random stress simulation at the base in the 1-DOF shear frame, $U = 10.0m/s$. Inset axes show 60sec stress simulation.

5.4.2 3 Degree of Freedom System

The CF-estimations of the rate of FDA for the 3-DOF system excluding background response were based on the PSD illustrated in Fig. 5.4b with a frequency domain $f \in [0.3, 5.0]Hz$. The trend of the relative error between the rate of FDA obtained by the JM- and WL-method in relation to the RF-method from the previous 1-DOF system continues in this analysis. Fig. 5.12 and Table 5.8 illustrate that the JM-method overestimates the rate of FDA by a relative error in the range RE$\in [0.29, 0.60]$. On the other hand, the WL-method gives raise to non-conservative estimations with a relative error in the range RE $\in [-0.21, -0.10]$.

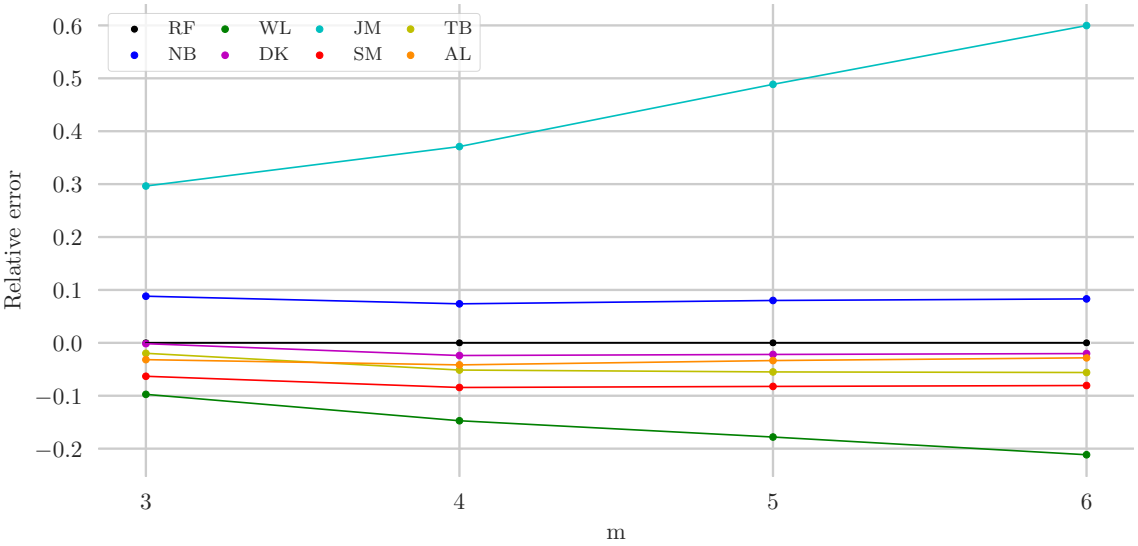

Fig. 5.12: Relative error of the rate of FDA in the 3-DOF shear frame. $f \in [0.3 - 5.0]Hz$.

m	NB	WL	DK	JM	SM	TB	AL
3	0.088	-0.097	-0.002	0.296	-0.063	-0.020	-0.032
4	0.074	-0.147	-0.024	0.371	-0.084	-0.051	-0.042
5	0.080	-0.178	-0.022	0.489	-0.082	-0.055	-0.033
6	0.083	-0.212	-0.020	0.600	-0.081	-0.056	-0.028

Table 5.8: Relative error of the rate of FDA in the 3-DOF shear frame. $f \in [0.3 - 5.0]Hz$.

The spectral bandwidth parameter ϵ of the process lies above 0.8 for all estimation points, with an average $\bar{\varepsilon} = 0.823$. The wide-banded process is confirmed by Fig. 5.13 and a greater deviation between the relative error of NB and the estimations achieved by the wide-banded methods DK, AL, TB and SM. The latter observation supports that the NB-method tends to overestimate the rate of FDA for a wide-banded process.

The LF- and HF-components used in the JM-method were divided at the frequency corresponding to the average of the first two natural frequencies of the system. This implies that the first peak of the stress spectrum in Fig. 5.4b is added to the LF-process, while the stress spectrum above the frequency limit of $f = 0.56Hz$ commit to the HF-process. For similar reasons as in the 1-DOF system, JM give raise to a too conservative rate of FDA-estimation.

A $10min$ sample of a random stress simulation along with a $60sec$ inset axes is shown in Fig. 5.13, indicating a more wide-banded process compared to the stress simulation of the 1-DOF system shown in Fig. 5.11.

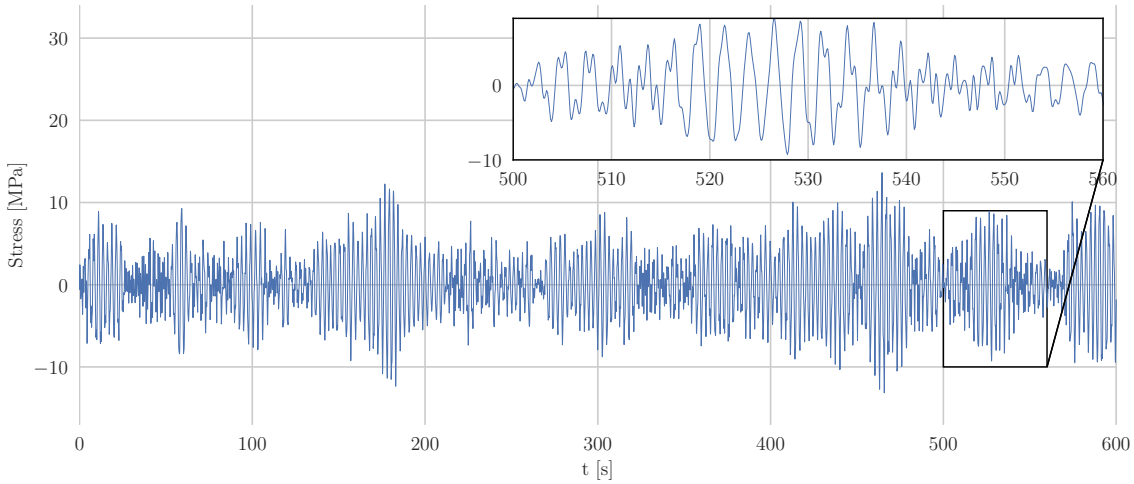

Fig. 5.13: Random stress simulation at the base for the 3-DOF shear frame, $U = 10.0m/s$. Inset axes show a $60sec$ stress simulation

5.4.3 5 Degree of Freedom System

The analysis of the 5-DOF shear frame included background response, as indicated by the associated PSD with a frequency domain $f \in [0.0, 5.0]Hz$ in Fig. 5.3c. Fig. 5.14 shows that the JM-method still presents the most conservative estimations except for $m = 3$. In contrast to the 1-DOF and 3-DOF system, the estimations obtained by WL gives raise to conservative estimations for $m > 3$. SM is the only method that proposes non-conservative estimations for all evaluated m-values. The SM-method does not include higher order spectral moments, which indicates that the method is prone to underestimating the rate of FDA in small, high frequency PSD cases relative to methods that include higher order moments. The underestimation can be observed in Fig. 5.14 and Table 5.9, where the SM-method underestimates the rate of FDA by $RE \in [-0.24, -0.13]$ for the different m-values.

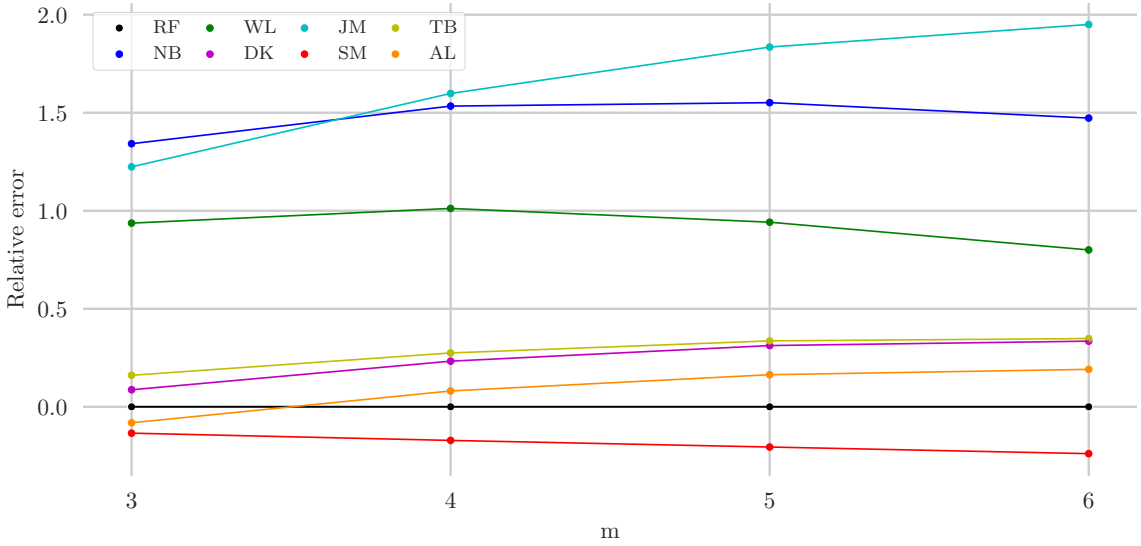

Fig. 5.14: Relative error of the rate of FDA in the 5-DOF shear frame. $f \in [0.0 - 5.0]Hz$.

m	NB	WL	DK	JM	SM	TB	AL
3	1.342	0.937	0.087	1.224	-0.134	0.161	-0.082
4	1.534	1.012	0.233	1.598	-0.172	0.275	0.081
5	1.551	0.942	0.312	1.835	-0.205	0.336	0.164
6	1.473	0.800	0.335	1.950	-0.239	0.348	0.191

Table 5.9: Relative error of the rate of FDA in the 5-DOF shear frame. $f \in [0.0 - 5.0]Hz$.

High values of spectral bandwidth ε gives raise to a chaotic stress history at the base of the shear frame. An average $\bar{\varepsilon} = 0.960$ along with the stress history in Fig. 5.15 clearly illustrates the wide-banded process, where the small oscillations occur due to the high frequency contribution.

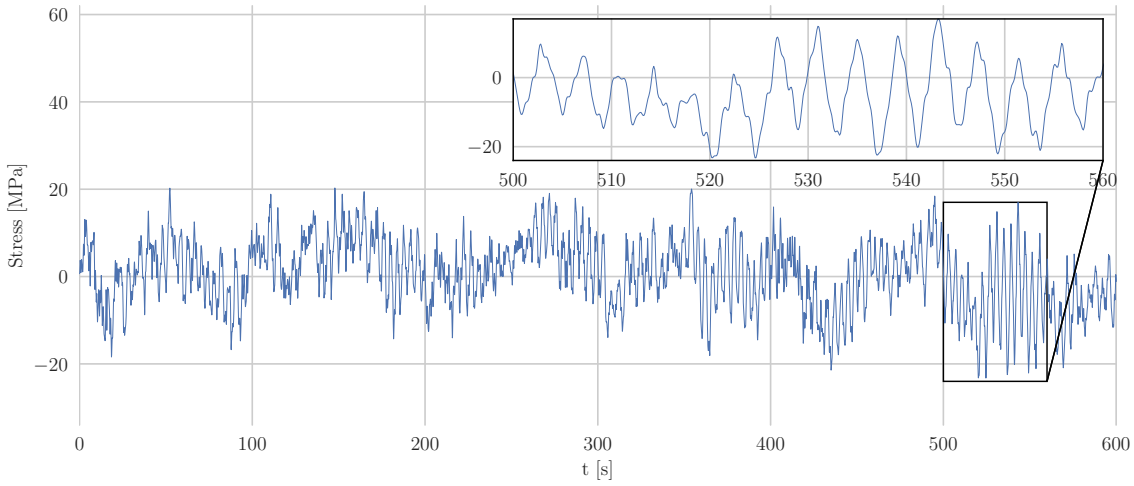

Fig. 5.15: Random stress simulation at the base for 5-DOF shear frame, $U = 10.0m/s$. Inset axes show 60sec stress simulation

5.4.4 Relative Error in Relation to Spectral Bandwidth

Fig. 5.16 illustrates the relative error for the 95th percentile of all evaluated points in the joint PDF for the six different analyses evaluated for $m = 5$. Each point shows the relative error of the CF-methods in relation to the average fatigue damage rate obtained by the RF-method. Similar plots for $m = 3,\ 4$ and 6 are presented in Appendix A. The data points in Fig. 5.16 are separated into different regions as a function of the spectral bandwidth ε, calculated according to the formula in Eq. (2.23). There are six regions, one for each of the shear frame analyses. Since ε is dependent on both the mean wind velocity U and the standard deviation of the turbulence σ_u, the points within the same region will not necessarily have the same ε. The system analyses excluding background response are indicated with a gray background in Fig. 5.16. The data points within these regions confirm less variation of the spectral bandwidth ε due to variable U and σ_u compared to spectrums including background response. One further observation is that the relative error tends to increase along with ε within each region, which coincides with the observations from the shear frame analyses. Considering all 423 estimation points for each CF-method in Fig. 5.16, DK and TB give the best estimates, followed by the AL-method.

The JM-method tends to give the most conservative estimations of the fatigue damage. As stated in Section 5.4.1, a large normalized variance of the LF component in combination with small rate of up-crossing rate $\upsilon^+_{0,2}/\upsilon^+_{0,1}$ give raise to a correction factor λ_{JM} greater than one. This observation corresponds well with observations Jiao and Moan made in their work [12]. From simulation results, Jiao and Moan concluded that the correction factor λ_{JM} gives great approximations of the rate of FDA for well-separated bimodal spectra. Their assumption that the fatigue damage due to the sum of the LF- and HF-process is the simple addition of the envelope process $P(t)$ and the

HF-process $X_2(t)$ may result in too conservative fatigue damage estimations for spectrum disparate from a well-separated bimodal spectrum. In such cases, Jiao and Moan suggested using an alternative approach for the estimation of the fatigue damage.

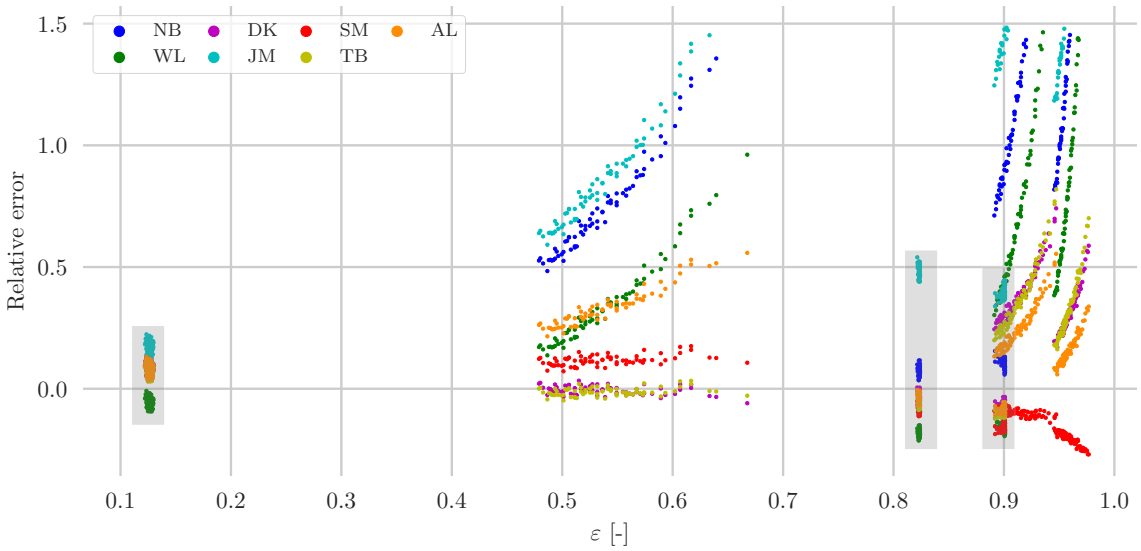

Fig. 5.16: Scatter plot of the relative error versus spectral bandwidth for the 95th percentile of points in the training data set for $m = 5$. Gray background highlight analyses excluding background response.

Dividing the comparison into 3 parts by the regions $\varepsilon \in [0.1, 0.2]$, $\varepsilon \in [0.4, 0.7]$ and $\varepsilon \in [0.8, 1.0]$ gives the method with minimum relative error within the specified range of ε. The WL-method gives the most accurate result for the 1-DOF analysis where the background response is excluded. Here $\varepsilon \in [0.1, 0.2]$ and the estimations from the WL-method has a mean absolute RE equal to 0.056. The following region $\varepsilon \in [0.4, 0.7]$ includes the analyses of the 3-DOF system without background response. The DK- and TB-methods give the best estimations for this region with mean absolute REs equal to 0.016 and 0.018, respectively. The highest range of spectral bandwidth $\varepsilon \in [0.8, 1.0]$ includes the last four analyses. The SM-method obtains the most accurate results with an absolute RE of 0.140. Here, SM provides non-conservative estimations which is not preferable in an engineering perspective. DK and TB stand out as the best methods overall, while JM gives raise to the most conservative estimations. Although DK is based on empirical simulations using MC simulations of a wide range of PSD shapes, the method provides more accurate estimations compared to methods with a more theoretical approach.

5.4.5 Effect of Background Response

As illustrated in Fig. 5.16, several CF-methods give non-conservative fatigue damage estimations, especially in the analyses without background response. By excluding the background response,

the spectral bandwidth of the stress spectrums decreases and the relative error tends to decrease for the majority of the CF-methods. The WL-method tends to give the most non-conservative estimations for the analyses without background response, which coincides with the observations in Section 5.4.1 and 5.4.2. When we include the background response, i.e. wind loading generated from low frequencies, WL gives rise to significantly more conservative fatigue damage estimations compared to observations without background response. We observe the same phenomenon in CF-methods such as DK and NB.

Chapter 6

Langenuen Bridge

6.1 Introduction

The main goal for this analysis is to compare the CF-methods with the RF-method for calculating the rate of FDA for a suspension bridge in buffeting wind loading. Several aspects of the analysis, such as wind load modeling, the creation of surrogate models through GPR and finally calculating the rate of FDA for the various methods, are very similar to what has been thoroughly explained in Chapter 5. The similar procedures will not be explained in detail for the Langenuen bridge example. The differences, such as creating a model to analyze and arrive a PSD, are explained thoroughly. Finally, the results from the Langenuen bridge are discussed separately and in accordance with the results from Section 5.4.1-5.4.3.

6.2 System Description

Cable supported bridges consist of four main elements: the bridge deck (or stiffening girder), cable system, pylons (or towers) and the anchor blocks [46]. The bridge deck is mainly exposed to bending moment generated from loading acting on the structure. The hangers, which are a part of the cable system, are exposed to tension forces and will transmit the forces to the main cable and later to the anchor blocks via the pylons.

The global design of the Langenuen bridge is based on the panel concept in the report *Langenuen Suspension Bridge-Aluminum Bridge Girder Alternative* proposed by Dr.techn. Olav Olsen in 2020 [18]. The main span of the bridge used in this analysis differs from the proposed span in the report by Dr.techn. Olav Olsen. Due to a change in the location of the bridge, the main span is set to 1220m. Fig. 6.1 illustrates the global dimensions of the Langenuen bridge, while Table 6.1 and 6.2 give an overview of analyzed sections along the girder and the section properties of the main elements, respectively.

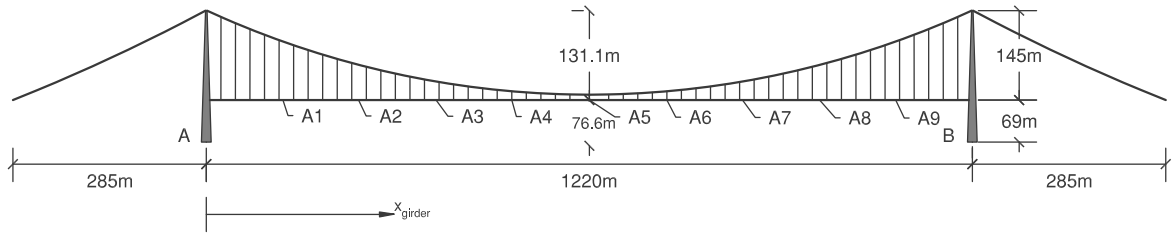

Fig. 6.1: Global dimensions of the Langenuen bridge.

Section	A1	A2	A3	A4	A5	A6	A7	A8	A9
x_{girder} [m]	120	244	364	488	608	732	852	976	1096

Table 6.1: Location of analyzed sections along the bridge girder.

	Material	Density $[kg/m^3]$	A $[m^2]$	E $[GPa]$	ν $[-]$
Girder	Aluminum	2700	2.50	70.0	0.32
Main cables	Steel	7850	0.364	200	0.30
Hangers	Steel	7850	0.00152	210	0.30
Pylons	Concrete	2650	16.0	35.0	0.20

Table 6.2: Section properties of the Langenuen bridge.

6.2.1 Abaqus Model

Modal properties from a finite element (FE) model of the Langenuen bridge have to be determined to compare the rate of FDA achieved by CF-methods in the frequency domain to the corresponding rate of FDA from the RF-method in the time domain. The modal properties have been extracted from a global FE model in Abaqus generated by a .INP-file that uses Abaqus Scripting Reference Guide [47]. The model was established by Mari Voll Dombu and Markus Gjelstad in their master's thesis from 2019, *Parametric modeling of a suspension bridge with an aluminum girder* [3]. Daniel Kjønsvik Bang and Erlend Ekern made some changes to the model in their master's thesis of 2020, *Aerodynamic Stability of a Suspension Bridge with an Aluminum Girder* [17], where they utilized wind tunnel testing to analyze the aerodynamic stability of girders with varying cross sections. Regarding stability analyses, Bang and Ekern concluded their work by selecting a girder shape with a height equal to $6.1m$ as the preferable alternative. Hence, the girder shape with a height of $6.1m$ was selected in our fatigue analyses. Fig. 6.2 shows the final FE model used in the following analyses. The global coordinate system is defined by the x-, y- and z-axis corresponding to the longitudinal-, lateral-, and vertical-direction of the bridge. The inset part of Fig. 6.2 shows the girder of the bridge with corresponding section force components $SF1$, $SM1$, $SM2$ and the displacements components of the bridge girder, respectively r_θ, r_y and r_z.

The pylons, main cables and hangers were modeled by B33 beam elements. The girder was modeled by 305 1D wire B32 Timoshenko elements, where the elements are located in the center of mass of the cross section. The cross-sectional properties of the girder are presented in Table 6.2 and 6.3, where A represents the solid material area, E is the Young's modulus, ν the Poisson ratio, $I_{i'}$, $i \in \{y,z\}$ the second moment of inertia about the local axis and $I_{t'}$ represents the torsional stiffness constant. The width and height of the girder are represented by B and D, respectively. The area A of the girder from Table 6.2 does not account for the non-structural elements attached to the girder. The components were accounted for by adding the corresponding properties separ-

ately in the Abaqus model. The master's thesis by Bang and Ekern gives a detailed overview of how these properties are added separately, in addition to a complete overview of the modeling process of the bridge.

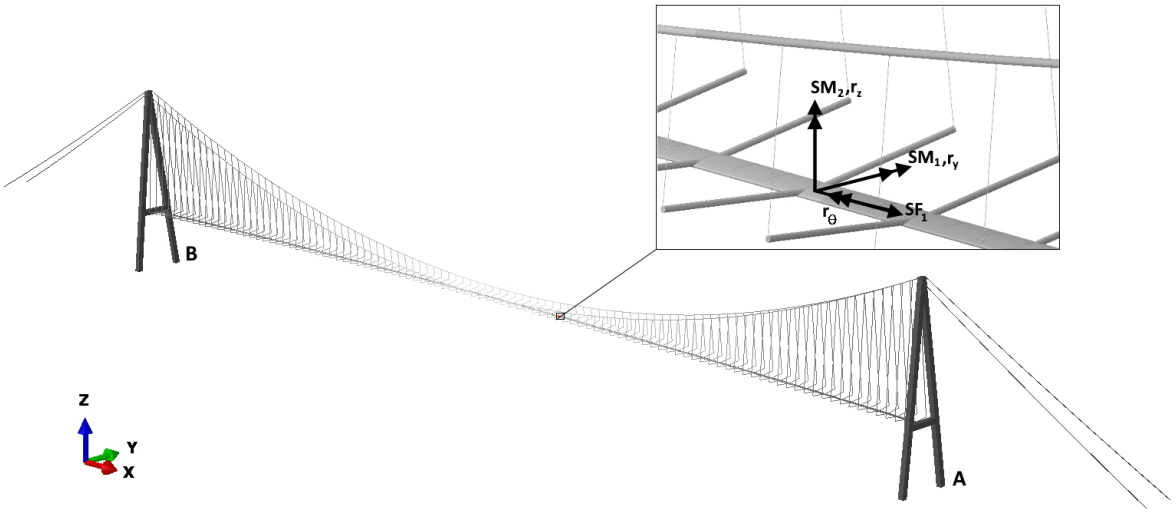

Fig. 6.2: Abaqus model of the Langenuen bridge with global coordinate system.

$I_{y'}$ $[m^4]$	$I_{z'}$ $[m^4]$	$I_{t'}$ $[m^4]$	B $[m]$	D $[m]$
12.81	248.51	28.56	35.88	6.10

Table 6.3: Cross-sectional parameters of the bridge girder.

6.3 Analysis

6.3.1 Selected Details

The cross section of the bridge was based on a panel concept built up by $12m$ long extruded aluminum sections in combination with friction stir welding. Bulkheads are included every $12m$ where the main cables are connected via the hangers [18]. The main dimensions of the bridge girder cross section are shown in Fig. 6.3. Nine girder sections equally distributed over the bridge girder have been investigated for the comparison of the rate of FDA achieved by the CF- and RF-estimations. The sections are illustrated by A1-A9 in Fig. 6.1. For each section, two points placed by the local coordinates $(y_1', z_1') = (-17.9m, 0.9m)$ and $(y_2', z_2') = (7.1m, -3.0m)$ were analyzed. The details associated with the points are illustrated in Fig. 6.3, referred to as $D1$ and $D2$. Both details are identified as transverse welds between the deck and bulkhead of the bridge girder, which by NS-EN 1999-1-3:2007 table $J.13$ is defined as detail type 13.1 with detail category $23-3.4$ [48].

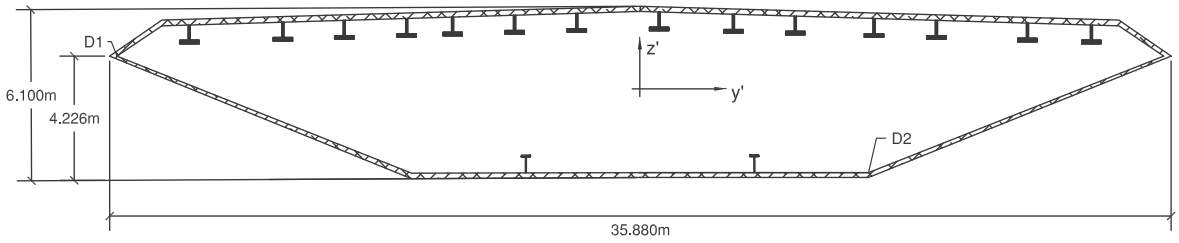

Fig. 6.3: Cross section of the bridge girder.

6.3.2 Design Curve

The SN-curves proposed by NS-EN 1999-1-3 are given as trilinear curves in a log-log scale [48]. To be able to compare the linear SN-curve applied for CF-methods and the RF-method, a linearization of the trilinear SN-curve was applied. It should be mentioned that aluminum structures are more sensitive to fatigue failure when exposed to cyclic loading compared to materials such as steel. Where steel exhibit well defined endurance curves, aluminum displays a more continuously decreasing SN-curve [49]. This effect is included in the design standard of aluminum.

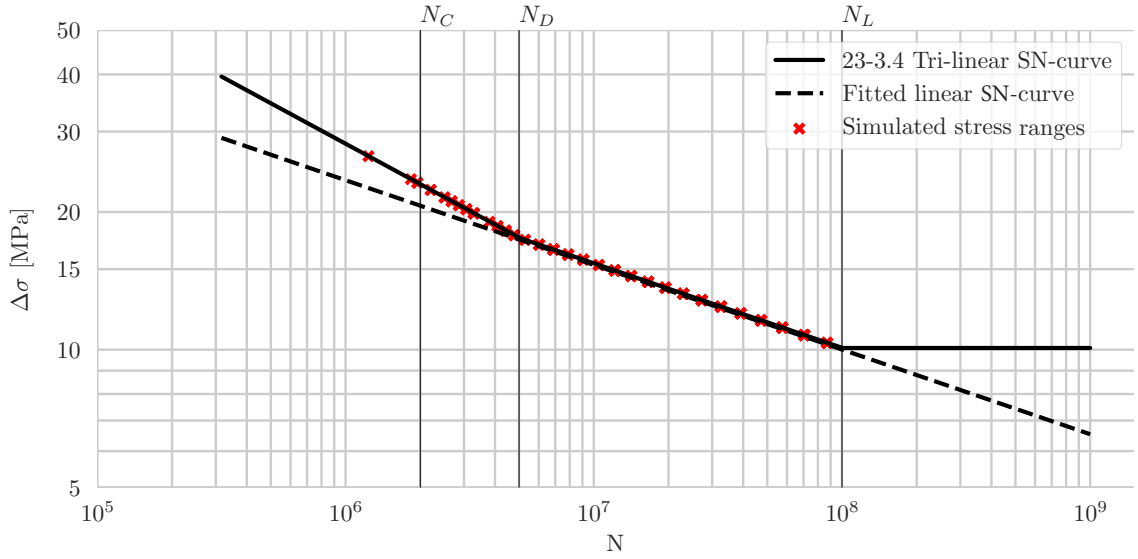

Fig. 6.4: Fatigue strength curves.

Fig. 6.4 illustrates the trilinear SN-curve for detail category 23−3.4 in NS-EN 1999-1-3:2007 [48]. As illustrated, the slope of the SN-curve coincides with $m = m_1 = 3.4$ for $N < N_C$ and $m = m_2 = 5.4$ for $N_D < N < N_L$. Here, N_C, N_D and N_L correspond to the number of cycles at which the reference fatigue strength, constant amplitude fatigue limit and the cut-off limit are defined. The simulated stress ranges in Fig. 6.4 illustrate the fatigue strength N for a given MC simulation with

a fixed mean wind U and standard deviation of the turbulence σ_u. This linearization gives the same results as the trilinear curve when $N_D < N < N_L$, and is a conservative approach elsewhere. Observe that Fig. 6.4 displays no simulated stress ranges above 10^8 cycles, as the trilinear curve becomes horizontal. In other words, the structure can handle an infinite number of cycles with such small stress ranges. Even though it is not visible in Fig. 6.4, around 70% of the cycles in the analysis ended up in this category.

6.3.3 Wind Field Modeling

The wind field is modeled similar to the joint PDF described in Section 5.3.2. Preferably, detailed measurements should be performed on-site for different sections along the bridge. The Weibull parameters should then be fitted to these measurements. Naturally, this is difficult before the bridge is raised. In this analysis, a PDF fitted to measurements at a nearby lighthouse Slåtterøy was used. The Norwegian Public Roads Administration suggested a 3-parameter Weibull distribution to describe the wind field [50], where a location factor θ was added to Eq. (2.32)

$$f(U) = \frac{k(U-\theta)^{k-1}}{c^k} \exp\left[-\left(\frac{U-\theta}{c}\right)^k\right] \tag{6.1}$$

where

$$k = 1.937, \quad c = 8.915, \quad \theta = -0.961 \tag{6.2}$$

These measurements are valid for a height of 10.0m, while the Langenuen bridge is 76.6m above

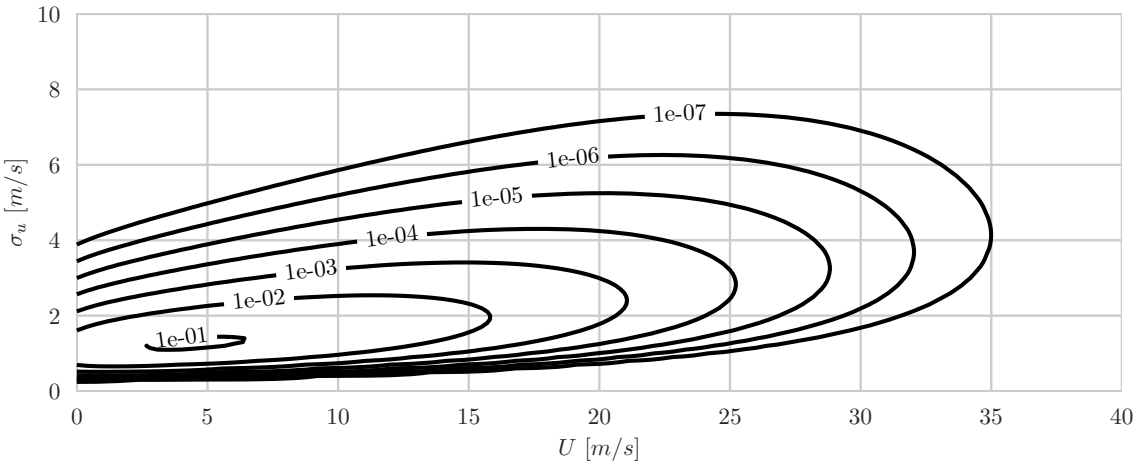

Fig. 6.5: Contour plot of the joint PDF for the mean wind velocity and the standard deviation of the turbulence along-wind for the Langenuen bridge.

sea level. Normally, the parameters should be scaled according to a vertical profile, e.g. the power law [51]. However, performing this vertical extrapolation yields stronger winds than what is ob-

tained from measurements at the North Sea [52], which is unrealistic. It was assumed that the terrain effects and the missing vertical extrapolation cancel each other out. Fig. 6.5 visualizes the joint PDF by utilizing Eq. (5.12). The standard deviation of the turbulence σ_u and mean wind velocity U were used to identify the turbulence intensities I_u and I_w. According to the amendment of N400 [53], the turbulence intensity I_w is given by $I_w = 1/2I_u$, where I_u is defined by Eq. (2.36).

6.3.4 Buffeting Response

The buffeting response calculations of the Langenuen bridge were performed in the frequency domain using a multimode approach. The axial displacement in the spanwise direction x of the girder was disregarded. Hence, the global displacement vector could be represented as the sum of the mean $\bar{\boldsymbol{r}}(x)$ and fluctuating part $\boldsymbol{r}(x,t)$. Considering only the time-varying fluctuating parts of the wind load, Eq. (2.27) is reduced to

$$\boldsymbol{q}(x,t) = \boldsymbol{B}_q \boldsymbol{v}(x,t) + \boldsymbol{C}_{ae}\dot{\boldsymbol{r}}(x,t) + \boldsymbol{K}_{ae}\boldsymbol{r}(x,t) \tag{6.3}$$

where $\boldsymbol{v}(x,t)$ is defined by Eq. (2.26), and $\dot{\boldsymbol{r}}(x,t)$ represents the time derivative of $\boldsymbol{r}(x,t)$ defined by Eq. (2.25). The Davenport admittance function $A(f)$ was included since higher frequency wind tends to lack correlation in the wind fluctuations along the bridge [54]. The buffeting load, including the admittance function, reads

$$\boldsymbol{B}_q = \frac{1}{2}\rho U B A(f) \begin{bmatrix} 2\frac{D}{B}\bar{C}_D & \frac{D}{B}C'_D - \bar{C}_L \\ 2\bar{C}_L & C'_L + \frac{D}{B}\bar{C}_D \\ 2B\bar{C}_M & BC'_M \end{bmatrix} \tag{6.4}$$

where A(f) is defined according to Davenport's formula [55]

$$A(f) = \frac{2}{(7f)^2}(7f - 1 + exp(-7f)) \tag{6.5}$$

Introducing generalized coordinates, along with the wind load from Eq. (6.3) gives the generalized modal EOM of the bridge

$$\tilde{\boldsymbol{M}}_0\ddot{\boldsymbol{\eta}}(t) + (\tilde{\boldsymbol{C}}_0 - \tilde{\boldsymbol{C}}_{ae})\dot{\boldsymbol{\eta}}(t) + (\tilde{\boldsymbol{K}}_0 - \tilde{\boldsymbol{K}}_{ae})\boldsymbol{\eta}(t) = \tilde{\boldsymbol{Q}}(t) \tag{6.6}$$

Here, $(\cdot)_0$ indicates that the properties are referred to still air conditions and $(\cdot)_{ae}$ refers to the aerodynamic behaviour. The generalized still air mass matrix $\tilde{\boldsymbol{M}}_0$, damping $\tilde{\boldsymbol{C}}_0$ and stiffness $\tilde{\boldsymbol{K}}_0$ are defined by Eq. (2.6) to Eq. (2.8). The mass normalized mode shapes $\boldsymbol{\Phi}(x)$ were obtained by solving the so-called eigenvalue problem in the Abaqus analysis of the bridge. As a result, the generalized mass matrix becomes $\tilde{\boldsymbol{M}}_0 = \boldsymbol{I}_{N_{mod}}$. The generalized buffeting load $\tilde{\boldsymbol{Q}}(t)$, aerodynamic

damping $\tilde{\boldsymbol{C}}_{ae}$ and stiffness $\tilde{\boldsymbol{K}}_{ae}$ were obtained by utilizing the relation from Eq. (2.9), which gives

$$\tilde{\boldsymbol{Q}}(t) = \int_{L_{exp}} \boldsymbol{\Phi}(x)^T \boldsymbol{B}_q(x) \boldsymbol{v}(x,t) dx \tag{6.7}$$

$$\tilde{\boldsymbol{C}}_{ae} = \int_{L_{exp}} \boldsymbol{\Phi}(x)^T \boldsymbol{K}_{ae} \boldsymbol{\Phi}(x) dx \tag{6.8}$$

$$\tilde{\boldsymbol{K}}_{ae} = \int_{L_{exp}} \boldsymbol{\Phi}(x)^T \boldsymbol{C}_{ae} \boldsymbol{\Phi}(x) dx \tag{6.9}$$

where L_{exp} is the flow-exposed part of the structure. Numerical values of the dynamic coefficients are shown in Table 6.4.

$\zeta[-]$	$\bar{C}_D[-]$	$\bar{C}'_D[-]$	$\bar{C}_L[-]$	$\bar{C}'_L[-]$	$\bar{C}_M[-]$	$\bar{C}'_M[-]$
0.005	0.60	0.00	−0.03	0.06	0.04	0.02

Table 6.4: Dynamic coefficients used in the analyses.

Assuming that the wind field is stationary and homogeneous, the correlation function of the generalized load $\boldsymbol{R}_{\tilde{Q}\tilde{Q}}(\tau)$ can be established from Eq. (2.10). Applying Fourier transform gives raise to the cross-spectral density matrix of the buffeting load

$$\boldsymbol{G}_{\tilde{Q}\tilde{Q}}(f) = \iint_{L_{exp}} \boldsymbol{\Phi}(x_1)^T \boldsymbol{B_q}(x_1) \boldsymbol{G}_V(f, \Delta x) \boldsymbol{B_q}(x_2)^T \boldsymbol{\Phi}(x_2) dx_1 dx_2 \tag{6.10}$$

where $\boldsymbol{G}_V(f, \Delta x)$ is the one sided cross-spectral density matrix defined by Eq. (2.38). In the current analysis, the off diagonal terms of the cross-spectral density matrix were assumed negligible. Table 6.5 gives the input parameters used to evaluate the the diagonal terms $\boldsymbol{G}_{uu}(f, \Delta x)$ and $\boldsymbol{G}_{ww}(f, \Delta x)$, which were calculated according to Eq. (2.39) in combination with the spectrum recommendation from N400, further described by Eq. (2.40) and Eq. (2.41). The integral length scales, according to N400, are given by ${}^xL_u = 100(76/10)^{0.3} = 184m$ and ${}^xL_w = (1/12)^xL_u = 15.3m$. The integral length scales, decay coefficients $C_{iy}, i \in \{u, w\}$, and the spectrum parameters $A_i, i \in \{u, w\}$ were assumed to be constant.

$\rho\ [kg/m^3]$	${}^xL_u\ [m]$	${}^xL_w\ [m]$	$A_u\ [-]$	$A_w\ [-]$	$C_{uy}\ [-]$	$C_{wy}\ [-]$
1.25	184	15.3	6.80	9.40	10.0	6.50

Table 6.5: Wind parameters according to N400.

The cross-spectral density matrix of the generalized modal coordinates η can be expressed by

$$\boldsymbol{G}_{\eta\eta}(\omega) = \overline{\tilde{\boldsymbol{H}}}(\omega) \boldsymbol{G}_{\tilde{Q}\tilde{Q}}(\omega) \tilde{\boldsymbol{H}}(\omega)^T \tag{6.11}$$

where $\boldsymbol{G}_{\tilde{Q}\tilde{Q}}(\omega)$ was obtained by utilizing the relation $\boldsymbol{G}_{\tilde{Q}\tilde{Q}}(\omega) = (1/2\pi)\boldsymbol{G}_{\tilde{Q}\tilde{Q}}(f)$ from Eq. (6.10). The frequency response matrix $\tilde{\boldsymbol{H}}(\omega)$ of the EOM is given by

$$\tilde{\boldsymbol{H}}(\omega) = \left[-\omega^2\tilde{\boldsymbol{M}} + i\omega(\tilde{\boldsymbol{C}} - \tilde{\boldsymbol{C}}_{ae}) + (\tilde{\boldsymbol{K}} - \tilde{\boldsymbol{K}}_{ae})\right]^{-1} \tag{6.12}$$

From the Abaqus model, it was possible to extract the section force mode shapes $\boldsymbol{\Phi}_F$ of interest. Considering the section forces $SF_1(x), SM_1(x)$ and $SM_2(x)$ described by Fig. 6.2, the symmetric response spectral density matrix for the selected section forces $\boldsymbol{G}_{FF}(\omega)$ was obtained directly by

$$\boldsymbol{G}_{FF}(\omega) = \boldsymbol{\Phi}_F(x)\boldsymbol{G}_{\eta\eta}(\omega)\boldsymbol{\Phi}_F(x)^T = \begin{bmatrix} G_{SF_1,SF_1} & G_{SF_1,SM_1} & G_{SF_1,SM_2} \\ G_{SM_1,SF_1} & G_{SM_1,SM_1} & G_{SM_1,SM_2} \\ G_{SM_2,SF_1} & G_{SM_2,SM_1} & G_{SM_2,SM_2} \end{bmatrix} \tag{6.13}$$

The stress spectrum $\boldsymbol{G}_{\sigma\sigma}(\omega)$ at an arbitrary spanwise position x can be obtained by applying a transfer function $\boldsymbol{T}$

$$\boldsymbol{G}_{\sigma\sigma}(\omega) = \boldsymbol{T}\boldsymbol{G}_{FF}(\omega)\boldsymbol{T}^T, \quad \boldsymbol{T} = \begin{bmatrix} \frac{1}{A} & \frac{z'}{I_{y'}} & \frac{-y'}{I_{z'}} \end{bmatrix} \tag{6.14}$$

where the area A, moment of inertia $I_{i'}, i \in \{y, z\}$ and the location of the detail (y', z') define the transfer function $\boldsymbol{T}$. The transfer function is based on beam theory, where the girder is considered to behave like a beam with coinciding shear-, mass- and area-center. Realizations of stress spectrums for section $A1$, $A3$ and $A5$ for detail $D1$ and $D2$ are illustrated in Fig. 6.6. Appendix C presents the stress spectrums for each investigated section along the bridge girder.

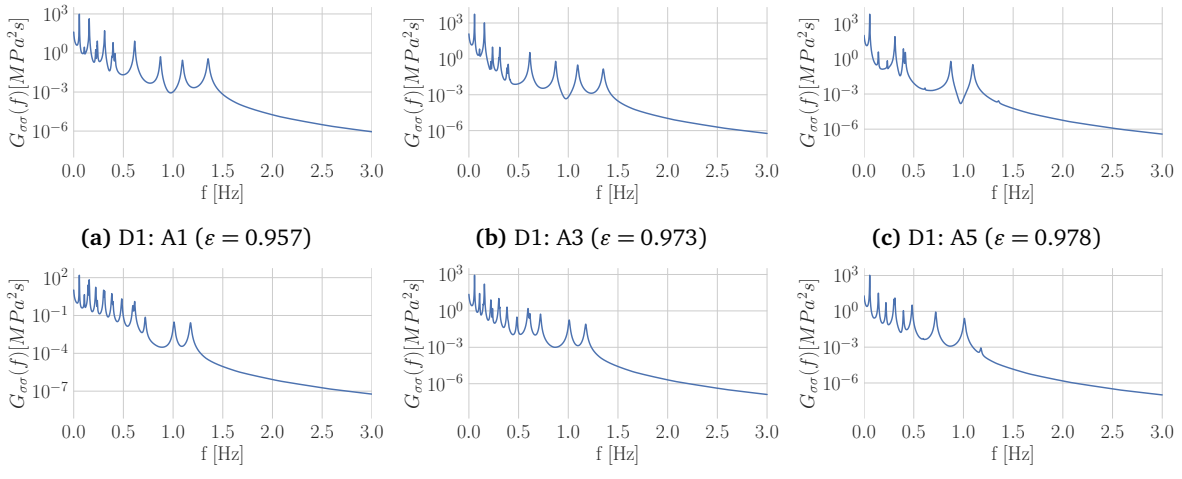

(a) D1: A1 ($\varepsilon = 0.957$) **(b)** D1: A3 ($\varepsilon = 0.973$) **(c)** D1: A5 ($\varepsilon = 0.978$)

(d) D2: A1 ($\varepsilon = 0.867$) **(e)** D2: A3 ($\varepsilon = 0.962$) **(f)** D2: A5 ($\varepsilon = 0.966$)

Fig. 6.6: Stress spectrums at three sections along the bridge girder for detail $D1$ and $D2$ with mean wind $U = 16.0m/s$ and standard deviation of the turbulence $\sigma_u = 3.00m/s$.

A realization of a $10min$ stress history from location $A3$ at the bridge girder confirms the wide-banded process. Fig. 6.7 shows a chaotic stress history which is obtained by a MC simulation of

the wide-banded stress spectrum from Fig. 6.6b.

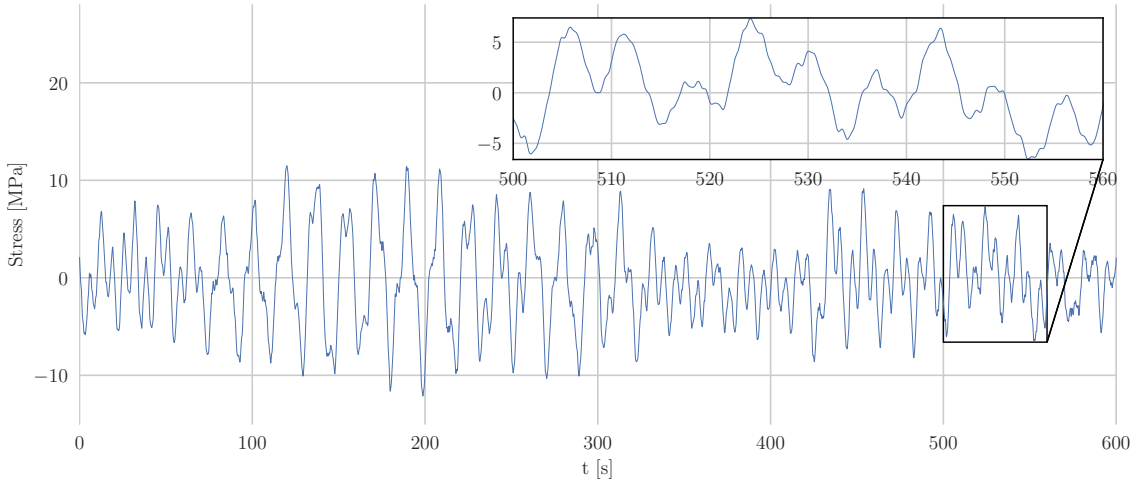

Fig. 6.7: Stress simulation from location A3, detail $D1$.

6.3.5 Significant Modes

The Abaqus model was needed to extract the displacement and force modes for the Langenuen bridge. The displacement modes were used to create the cross-spectral density matrix of the buffeting load and the aerodynamic stiffness $\tilde{\boldsymbol{K}}_{ae}$ and damping $\tilde{\boldsymbol{C}}_{ae}$. The force modes were then utilized to find the section forces at a specified location in the bridge. The girder model consists of 305 beam elements, and the fatigue analysis in this thesis was performed on nine elements distributed along the span of the bridge. We should include a sufficient amount of modes to achieve convergence of the expected life of the bridge. By including all 100 modes in this Abaqus model, the analysis became very computationally costly. To reduce computational complexity, it was of interest to only include the modes that contributed significantly to the rate of FDA for the elements analyzed. Test analyses of the bridge with a few selected modes showed that certain high-frequency modes contributed significantly to the rate of FDA and should not be neglected.

To ensure that all significant modes were included, a test was performed by running the analysis for every mode in the Abaqus model (1 - 100). For every mode, the fatigue damage was calculated for a given wind velocity ($U = 16.0m/s$) and standard deviation of the turbulence component along-wind ($\sigma_u = 3.00m/s$), multiplied by its probability of occurrence. The calculated values are only a fraction of the final rate of FDA but is a simple way of comparing the contribution from each mode. The heat map in Fig. 6.8 illustrates the fatigue damage contribution from mode 1 to 100 along the x-axis and for the nine selected elements along the y-axis. By running this analysis, 16 modes exceeded the chosen fatigue damage criterion of 10^{-20} in any of the elements for detail $D1$.

These mode shapes are plotted in the Appendix B in lateral-, vertical- and torsional-direction. Most modes that were excluded in this analysis are cable modes, where the girder is almost unaffected. The exact same analysis gave 17 significant modes for detail $D2$, many of which are common for the two details. The heat map for detail $D2$ is shown in Appendix D.

It is clear that both low- and high-frequency modes contributed to the rate of FDA, even when a Davenport admittance function was included. By performing such a mode-by-mode comparison, the aerodynamic coupling effect between the modes was neglected. The coupling effect is most prominent for higher wind velocities [56], while wind velocities below $25m/s$ are usually most damaging with respect to fatigue. The joint PDF in Fig. 6.5 shows that strong winds above $25m/s$ are considerably rarer than winds below $25m/s$ at the Langenuen bridge. Even though these stronger winds will cause more fatigue damage than weaker winds, their low probability of occurrence makes them less critical to the rate of FDA overall.

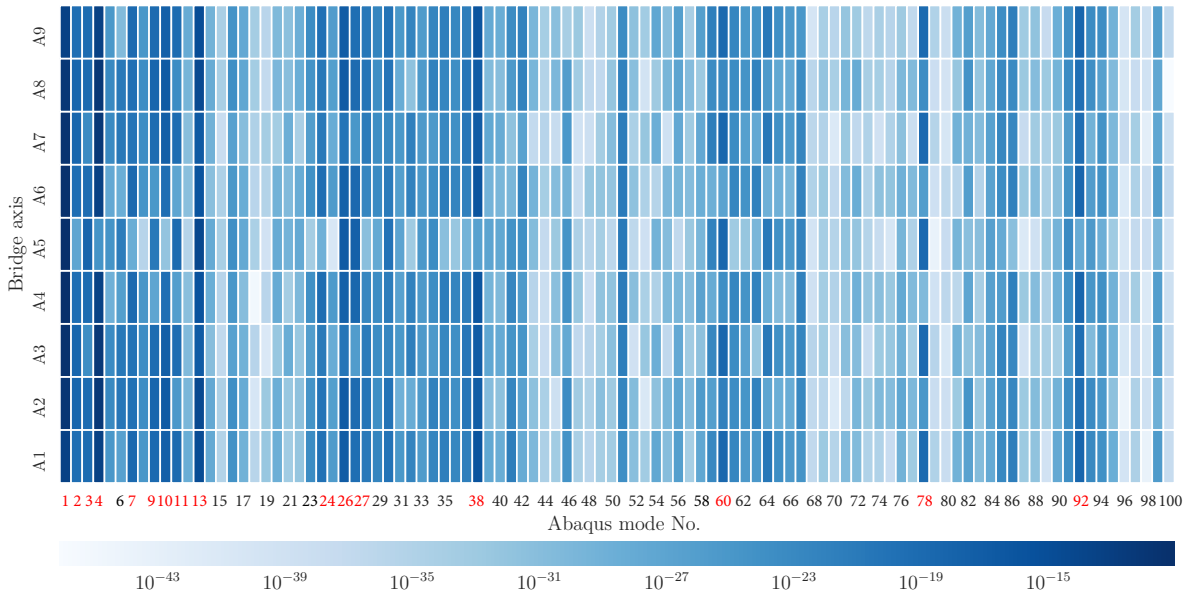

Fig. 6.8: Fatigue contribution for detail $D1$ from mode 1 - 100. Mode numbers with red highlighting exceed the fatigue damage criterion of 10^{-20}.

6.3.6 Fatigue Damage Evaluation

When the choices regarding SN-curve, which modes to include and design details have been made, the output in the analysis described in Section 6.3.4 will be a stress spectrum. From this spectrum, the procedure to find the rate of FDA is almost identical to what was described in Section 5.3.3-5.3.4. Algorithm 1 is valid for both the shear frame and the Langenuen bridge. Some important differences between the Langenuen bridge and the shear frame, such as the joint PDF between U and σ_u and different SN-curves, caused the shapes of the surrogate models to differ from each

other. The same learning function was used as the one defined in Eq. (5.13), but some of the parameters were changed to fit the Langenuen bridge and its complexity. The length scales were set to 2.0 in U-direction and 0.6 in σ_u-direction, primarily to decrease the density of points and achieve convergence with less training data. In addition, the n-parameter in the learning function was set to 0.05 and the termination criterion was equal to 5‰. Fig. 6.9 shows the first nine iterations of the sequential updating approach for the Langenuen bridge. In the last iteration in Fig. 6.9, the shape of the surrogate model becomes visible, and it is clear that the increased winds around Langenuen shift the surrogate model towards higher wind velocities compared to the shear frame example.

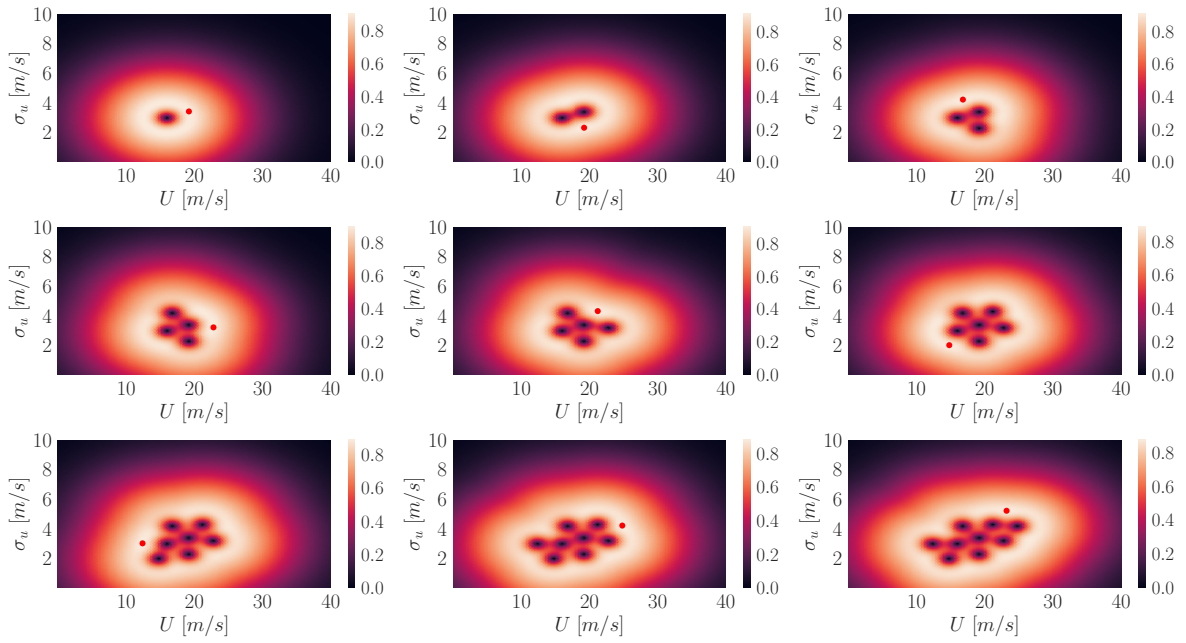

Fig. 6.9: The learning function is visualized for the first nine iterations at the Langenuen bridge. The maximum value and next point is marked as a red dot.

The rate of FDA was obtained by a numerical integration of the surrogate model over the mean wind velocity U and the standard deviation of the turbulence σ_u according to Eq. (5.14). Fig. 6.10 shows two surrogate models obtained by the RF-method at location A2 for detail $D1$. In total, there are 144 such surrogate models, one for every method at every element and detail. The surrogate models are very similar in shape but are separated by scaling. The values of the training data set corresponding to detail D1 are considerably higher, resulting in a larger rate of FDA than detail D2.

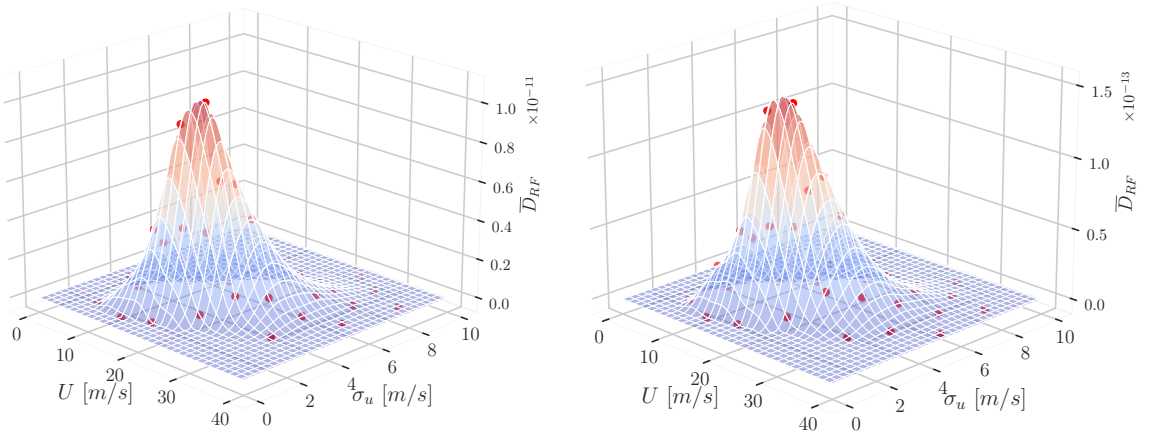

(a) Training data set of 35 points for detail D1

(b) Training data set of 36 points for detail D2

Fig. 6.10: Surrogate models of the RF-method at location A2.

6.3.7 Accuracy and Computational Complexity

The process of finding the stress spectrum for a given point in the surrogate model can be time-consuming. The size of the training data set will affect the accuracy of the surrogate model and the computational complexity. This balancing between accuracy and complexity can be adjusted with the length scales, n-parameter and termination criterion as discussed in Section 5.3.6-5.3.7. The length scale was changed from 0.2 to 0.6 in σ_u-direction to fit the surrogate models of the Langenuen bridge. Visually, there are some differences between the surrogate models but not enough to justify such an increase. We mainly increased the length scale to make the algorithm more efficient by reducing the training data. The surrogate models are easy to inspect for apparent errors, but minor flaws may be challenging to detect. Both a too large termination criterion and insufficient density around the peak tend to underestimate the rate of FDA, consequently providing non-conservative estimations. These non-conservative results are critical for an accurate estimation of the expected life but less important for the comparison in this thesis. Since the same training data set was used for all the methods, the potential error should not cause some methods to estimate higher or lower relative error. The testing of different termination criteria and n-parameters in Table 5.4 are not directly applicable in this analysis because of the difference between the surrogate models and length scales. However, the results can give an indication of the expected error by reducing the training data set to around 40 points. The error relative to the most accurate models was then found to be around 3%. Compared to the simplifications regarding SN-curves and the joint PDF for the wind, 3% error was assumed to be acceptable.

6.4 Results and Discussion Langenuen Bridge

The fatigue life due to buffeting wind loading for detail $D1$ and $D2$ at various sections along the bridge girder are presented in Fig. 6.11, in addition to numerical values in Appendix E. By comparing the expected life of the two details studied, the transverse weld $D1$ between the deck and bulkhead of the bridge girder was the most critical.

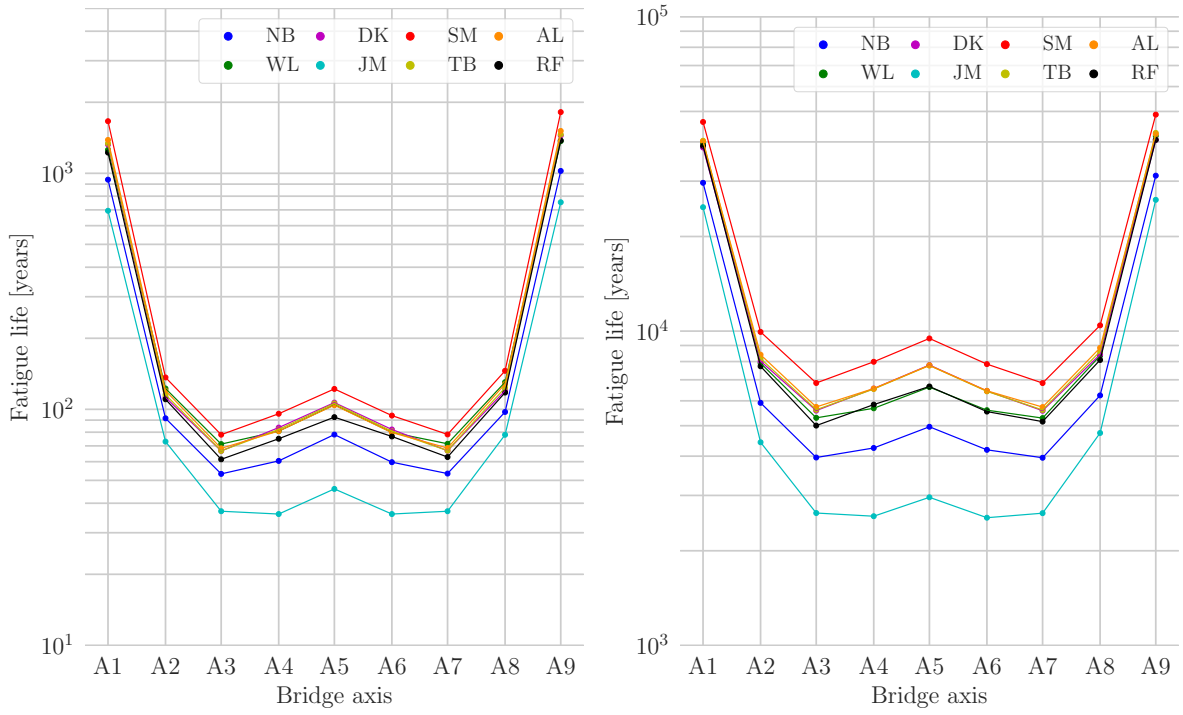

(a) Detail $D1$ **(b)** Detail $D2$

Fig. 6.11: Fatigue life for various calculation methods along the bridge girder.

The stress spectrum might be implemented in various ways into the CF-method JM, which divides the spectrum into two regions. We used the equal-variance rule, i.e. divide the spectrum into two segments with equal variances. Both in the shear frame examples and at the Langenuen bridge, JM overestimates the rate of FDA due to the lack of a bimodal stress spectrum. For that reason, JM is excluded in the following comparison of the CF-methods and the RF-method. The following analyses includes the CF-methods NB, WL, DK, SM, TB and AL. Fig. 6.12-6.13 together with the corresponding numerical values in Table 6.6-6.7, respectively, presents the relative error between the CF-methods and the RF-method.

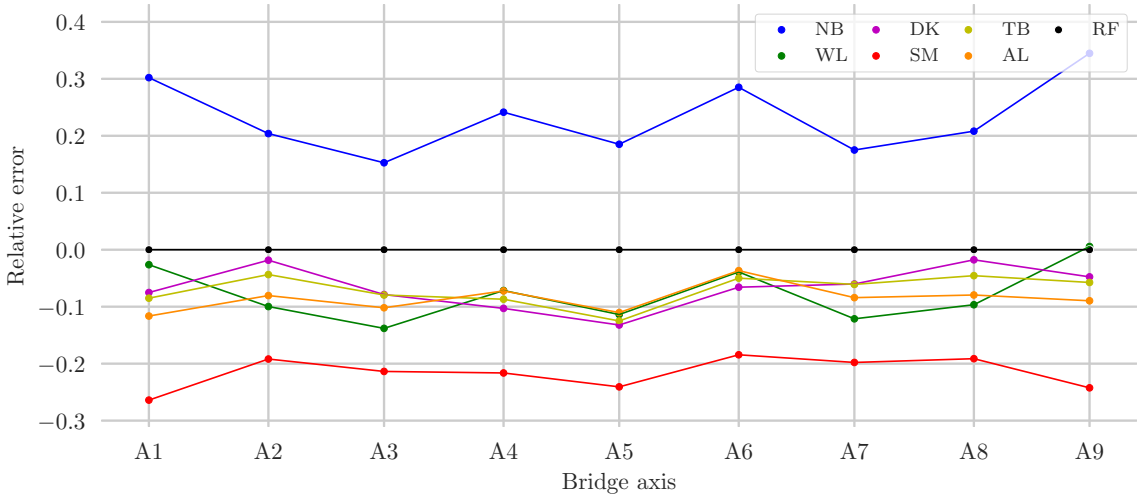

Fig. 6.12: Relative error of the rate of FDA for the CF-methods along the bridge girder, detail $D1$.

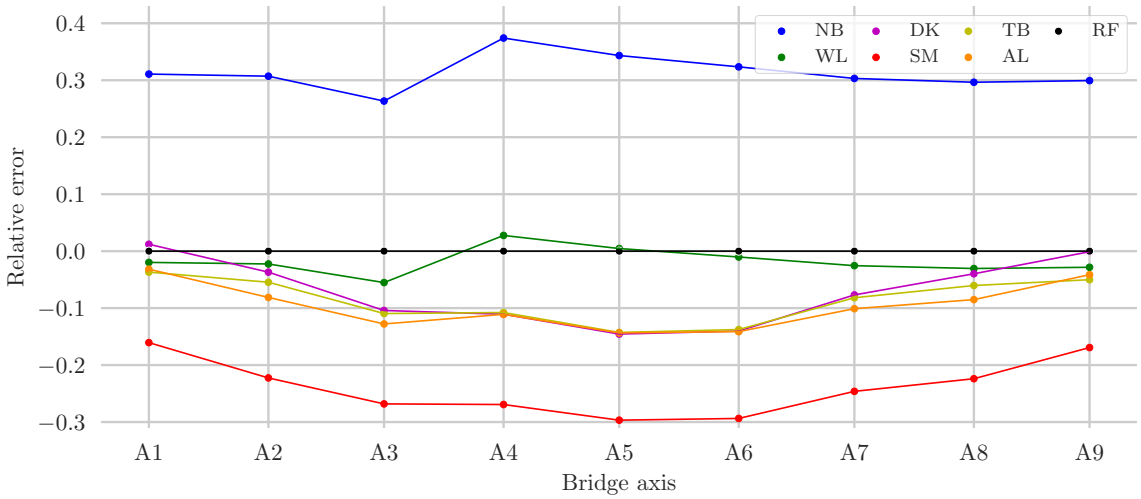

Fig. 6.13: Relative error of the rate of FDA for the CF-methods along the bridge girder, detail $D2$.

Bridge axis	NB	WL	DK	JM	SM	TB	AL
A1	0.302	-0.026	-0.075	0.764	-0.264	-0.085	-0.116
A2	0.204	-0.100	-0.018	0.509	-0.192	-0.044	-0.080
A3	0.153	-0.138	-0.079	0.670	-0.214	-0.079	-0.102
A4	0.241	-0.072	-0.103	1.086	-0.216	-0.087	-0.072
A5	0.185	-0.114	-0.132	1.023	-0.241	-0.125	-0.110
A6	0.285	-0.039	-0.066	1.148	-0.184	-0.050	-0.037
A7	0.175	-0.121	-0.060	0.698	-0.198	-0.061	-0.084
A8	0.208	-0.097	-0.018	0.505	-0.191	-0.046	-0.079
A9	0.345	0.006	-0.048	0.827	-0.242	-0.057	-0.090

Table 6.6: Relative error of the rate of FDA for the CF-methods along the bridge girder, detail $D1$.

Bridge axis	NB	WL	DK	JM	SM	TB	AL
A1	0.311	-0.020	0.012	0.567	-0.161	-0.037	-0.032
A2	0.307	-0.023	-0.037	0.745	-0.223	-0.055	-0.081
A3	0.263	-0.055	-0.104	0.897	-0.268	-0.110	-0.128
A4	0.374	0.028	-0.111	1.266	-0.269	-0.108	-0.111
A5	0.343	0.005	-0.146	1.252	-0.297	-0.143	-0.144
A6	0.324	-0.010	-0.140	1.176	-0.294	-0.138	-0.141
A7	0.303	-0.026	-0.077	0.956	-0.246	-0.082	-0.101
A8	0.296	-0.031	-0.040	0.707	-0.224	-0.060	-0.085
A9	0.299	-0.028	-0.001	0.551	-0.169	-0.050	-0.041

Table 6.7: Relative error of the rate of FDA for the CF-methods along the bridge girder, detail $D2$.

6.4.1 Non-Conservative Estimations

Apart from JM and NB, SM has the highest relative error in Table 6.6 and 6.7. The method also provides non-conservative estimations for all elements analyzed. Similar results were observed in the 3-DOF and 5-DOF shear frame example. Larsen and Lutes tested the SM-method on bimodal spectrums, where the worst-case resulted in an underestimation of 23% [57]. These tests were dependent upon the frequency ratio, describing the relative distance between the two peaks, and the area ratio, defined as the area of peak one divided by the area of peak two. These two parameters are easy to calculate for a bimodal spectrum, but does not make sense for multimode spectrums such as the ones in Fig. 6.6. Nevertheless, this test suggests that a large distance between the peaks can lead to an underestimation of the fatigue damage. In Fig. 6.6, the higher order modes have a very low value compared to the low frequency modes. Still, the distance may be an explanation as to why the SM-method provides non-conservative estimations. It should also be mentioned that the authors originally developed and tested the method on two unimodal and two bimodal sprectrums [14]. They claim good accuracy on bimodal spectrums, but no such spectrums are analyzed in the shear frame or the bridge example.

A low area ratio may also poorly affect the estimations. Again, the area ratio is not easy to calculate for a multimode spectrum, but this suggests that the width and height of the modes can also cause SM to underestimate the estimations. We know that the first mode is very dominant in most stress spectrums for detail $D1$ from Fig. 6.3, but it is not a wide peak. Higher order modes have lower value but are wider as well. The area ratio between high- and low-frequency modes naturally change for every element observed. It is also dependent on which modes are included in the analysis. This implies that the modes selected in Section 6.3.5 can reduce the accuracy of the SM-method, even when contributing little to the rate of FDA.

From the spectral bandwidths given in Fig. 6.6, it becomes clear that the stress spectrums are very wide-banded at most locations along the bridge. Observe that the spectral bandwidth ϵ is

larger than 0.95 for the illustrated spectrums, except in Fig. 6.6d. Comparing these bandwidths to the scatter plot in Fig. 5.16 substantiate the fact that SM provides non-conservative estimations. In the shear frames, where other CF-methods significantly overestimate the rate of FDA, SM underestimates it as the bandwidth parameter ϵ increases. This also corresponds well with the observations from Larsen and Lutes [57]. It does not explain why most other CF-methods also produce non-conservative estimations.

6.4.2 Overall Accuracy

As illustrated in Fig. 6.12-6.13, DK, WL, TB and AL achieve an absolute average relative error about 0.1 for the linear SN-approach. Since the introduction of the closed-form method DK, several comparison studies have found the method to be widely applicable [11, 58–61]. The studies concluded that the DK-method provided some of the most accurate fatigue damage estimations, which coincides with the comparison in our analyses of the shear frames in Chapter 5 and along the girder of the Langenuen bridge. Although DK is a completely empirical approach not supported by a theoretical framework, the small levels of the relative error compared to RF indicate that Dirlik made a proper approach in his development of the empirical corrections to estimate the fatigue damage.

WL is another CF-method that provides fairly accurate rate of FDA-estimations. Similar to DK, the method is created by an empirical approach where various wide-banded processes are simulated. Both DK and WL include four spectral moments in their formula, i.e. M_0, M_1,M_2 and M_4. As the moment gets higher, the contribution of higher stress ranges to the moment increases, which leads to higher rate of FDA. Based on the relative error from Table 6.6-6.7, it seems like this integration benefit both DK and WL. Especially for detail $D2$, where WL produces almost identical rate of FDA estimations as the RF-method with an absolute average error around 0.025.

TB and AL, in addition to the discussed CF-methods SM, WL and DK provide less conservative estimations compared to the NB-method. It is widely accepted that the NB-estimation applied to wide-banded processes overestimates the FDA [34]. Hence, CF-methods i.e. WL, SM, AL and TB, produce a correction factor that reduces the original rate of FDA from NB. With this in mind, the conservative estimations from the NB-method can be useful to estimate an upper bound for the rate of FDA. DK, based on approximating the rainflow stress ranges, achieves similar non-conservative estimations due to a different approach in the fatigue estimations. Overall, the CF-estimations of the rate of FDA for detail $D1$ and $D2$ provide quite accurate results in an engineering perspective.

6.4.3 Small High-Frequency Components

Larsen and Lutes [57] also found that small high-frequency components could cause certain CF-methods to over- or underestimate the fatigue damage. This is a concern as most high-order modes are small compared to low-order modes. When a Davenport admittance is applied, the contribution

towards the rate of FDA is even lower. One could imagine that including a low-contributing mode with high-frequency would only increase the computational complexity, but Larsen and Lutes suggest that the rate of FDA may be over or underestimated as a consequence. A positive aspect of the SM-method is the simplicity of the formula. Other proposed methods use higher order spectral moments, while SM only uses a single spectral moment $M_{2/m}$. According to Larsen and Lutes, this makes the method less prone to overestimate the rate of FDA. Apart from the 1-DOF system in Section 5.4.1, this corresponds well to the results in this thesis.

6.4.4 Accuracy of Rainflow and Miner's Rule

Both in this thesis and in similar analyses [45, 62], the RF-method is treated as an exact solution to test the accuracy of the CF-methods. Even though the algorithm itself is considered the most accurate cycle counting algorithm, there are some uncertainties in the process of calculating the rate of FDA from a stress spectrum. Both in the shear frame example and the Langenuen bridge, 60 MC simulations were performed over a time series of 60 minutes. Even when averaged over that many simulations, minor differences were observed in the fatigue damage. The surrogate model was also affected by these deviances, causing the shape of the model to be rougher than the surrogate models created by the CF-methods. The rate of the FDA did not change drastically because of this roughness. Nevertheless, the expected life could change ±1 % from each simulation. This deviance is not enough to drastically alter the results in Table 6.6 and 6.7, but it should be noted that this is a potential source of error.

After performing a MC simulation and applying the RF-algorithm to count cycles, Miner's rule was utilized to arrive at a rate of FDA. As stated in Section 4.4, Miner's rule is mainly used for its simplicity. The accuracy has proved to provide reasonable approximations for stationary processes [5]. Though it should be noted that Miner's rule is not without flaws, and a disadvantage is that it is not possible to decide if the estimations are conservative or non-conservative. The cumulative damage from Eq. (4.4) is assumed to reach 1.0 before failure occurs. Test estimations have shown that failure can occur on both the conservative and non-conservative side of 1.0 [5]. Another aspect of Miner's rule that has been criticized is that the order of the stress cycles does not matter. A cycle does the same amount of damage when a component is brand new as it does close to failure, which is considered a simplification [13]. Even though the wind loading is assumed stationary in this analysis, it is important be aware of Miner's rule's weaknesses.

6.4.5 Simplifications in the Wind Modeling

The modeling of the wind is important to test the fatigue calculation methods on a realistic stress spectrum. Even though we have devoted much time to model the wind accurately, it is arguably where we have made most simplifications as well because of the sheer complexity. Preferably, full-scale velocity measurements should be obtained, similar to the measurements on the Hardanger

Bridge [25]. Since the Langenuen bridge is not built yet, such an accurate representation is difficult to obtain, and simplifications must be made. For this analysis, the PDF for the mean wind velocity was taken from the nearby lighthouse Slåtterøy. The PDF was not scaled from $10m$ up to the height of the bridge deck and no adjustments were made related to the terrain effects. These were assumed to cancel each other out, which is very difficult to justify without on-site measurements. The lighthouse is located on the coast, where strong winds have little or no obstacles in the terrain. The Langenuen bridge is located nearby but shielded by islands and mountains. The terrain effects should have a significant impact on the PDF for the mean wind velocity. This simplification should not make the comparison in this thesis less valid but greatly affects the expected life of the bridge in years. Due to lack of data, the PDF for the standard deviation of the turbulence component from Hardanger Bridge is re-used for the Langenuen bridge, described by Eq. (2.37). This is another simplification that has an impact on the expected life of the bridge. Because the Hardanger Bridge is located around $100km$ northeast of Langenuen, the parameters in the lognormal distribution are most likely different. The two bridges are not oriented in the same direction either, making it difficult to transfer the parameters from one to the other. Also, the wind direction was here assumed to be perpendicular to the Langenuen bridge at all times. Naturally, this is another simplification that affects the expected life of the bridge. The alternative is to include the effect of a varying wind direction [36], which should further increase the expected life of the bridge.

6.4.6 Trilinear SN-curve

The fitted linear SN-curve in Section 6.3.2 is another impactful simplification affecting the analysis. This linearization is a conservative approach because every stress range corresponds to an equal or lower amount of cycles than a bi- or tri-linear SN-curve. In such a wide-banded process, most stress cycles have ranges below the cut-off limit and will thus correspond to an infinite number of cycles in a trilinear SN-curve. These low stress ranges naturally contribute less than large ranges to the rate of FDA for the linear curve, but since they are abundant, their impact may still be influential. In addition, the linear SN-curve provides conservative estimations for stress ranges above the constant amplitude fatigue limit. There are few such cycles, but they contribute significantly more to the rate of FDA per cycle. To find out how conservative it is to use a linear curve instead of a trilin-

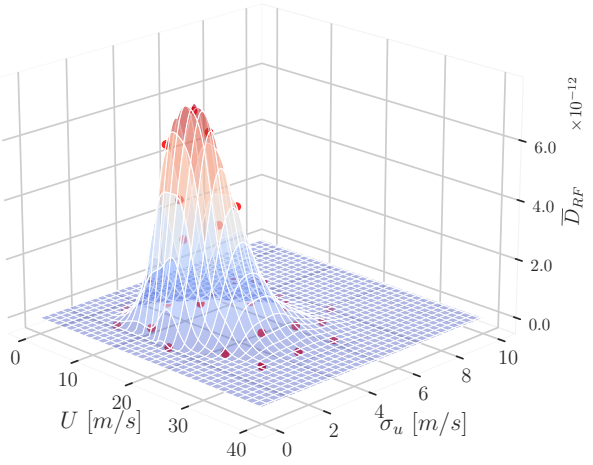

Fig. 6.14: Surrogate model at location A5 of the RF-method using a trilinear SN-curve. The training data set consist of 31 points.

ear curve, we ran the same analysis using the RF-method over all locations in the bridge for both details. The CF-methods presented in this thesis assume a linear SN-curve and can thus not be implemented for a trilinear curve. Fig. 6.14 shows the surrogate model at location A5. The shape of the surrogate model depends on the choice of SN-curve, which is why the length scales had to be adjusted to 1.8 in U-direction and 0.5 in σ_u-direction to account for a slightly rougher surface. The estimated lifetime along the bridge using a trilinear curve is given in Appendix E as RF_{tri}. Observe how the estimated life is around 100% of the RF using a linear SN-curve. Suddenly all the CF-methods provide conservative estimations when compared to RF_{tri}. To accurately estimate the expected life of the bridge, this is a very important aspect. But for the comparison, which is our main goal, we wanted to compare all the CF-methods to the RF-algorithm using the same SN-curves. The RF_{tri} column in Appendix E is thus not intended as a comparison to the CF-methods, but as an indicator of the simplification made with a linear SN-curve.

Chapter 7

Conclusion

The primary goal of this thesis was to compare some of the most popular closed-form methods with the rainflow method for calculating the fatigue damage in buffeting wind loading, using a sequential updating approach with Gaussian process regression. After theory was presented for the relevant topics, the full procedure to calculate the fatigue damage accumulation was explained, along with a test of the various methods on simple shear frames. Finally, the same procedure was applied to test the methods on two details for different sections along the Langenuen bridge.

Using closed-form methods for calculating fatigue damage under buffeting wind loading can reduce the complexity of the calculations. A sufficiently long time series can also be difficult to obtain, often making closed-form methods the best alternative. The methods should ideally provide consistent output across different types of spectrums and slopes of SN-curves. Furthermore, the methods should give a low relative error compared to a time domain approach, such as the widely accepted rainflow algorithm combined with Miner's rule.

The sequential updating approach proved to be an efficient computational tool to calculate the rate of fatigue damage accumulation. This way, the training data set can be generated such that it is an optimal fit for the shape of the surrogate model. The surrogate models were highly dependent on the parameters of the chosen learning function. These parameters should be fitted for each analysis based on analytic complexity and required accuracy. For a two-dimensional Gaussian process regression, the surrogate models can be visually inspected for flaws, reducing the risk of errors.

By analyzing different shear frames, it was possible to study the accuracy of different closed-form estimations of fatigue damage for various stress spectrums. The methods proposed by Dirlik along with Tovo and Benasciutti gave the most consistent results overall, tested for the SN-slopes $m = 3, 4, 5$ and 6. Especially for a spectral bandwidth in the range $\varepsilon \in [0.4, 0.7]$, these two methods gave accurate estimations of the rate of fatigue damage accumulation. Observations indicate that the relative error tends to increase along with a higher m-value, which corresponds to a more gentle slope of the linear SN-curve. This phenomenon is most visible for the narrow band method along with the Jiao and Moan method, which in general results in too conservative estimations for all stress spectrums. By separating the shear frame analyses into two groups, including and excluding background response, respectively, a non-conservative trend was observed for the analyses excluding background response. Especially for spectral bandwidth above 0.8, the closed-

form methods proposed by Wirching and Light, Tovo and Benasciutti, Dirlik and the methods $\alpha_{0.75}$ and single-moment had a tendency to underestimate the fatigue damage. Once we included the background response, the associated stress spectrums became closer to real structures exposed for natural loads, and single-moment turned out to be the only closed-form method that provided non-conservative results.

Closed-form methods tested on a finite element model of the Langenuen bridge in buffeting wind loading using a sequential updating approach gave quite accurate estimations for the rate of fatigue damage accumulation. The drawback of the closed-form estimations was the non-conservative results for the investigated details along the Langenuen bridge, except for the estimations by the narrow band method and the method proposed by Jiao and Moan. Although the narrow band method was too conservative, as expected, the method provided consistent and conservative estimations along the bridge girder. The conservative estimations from the narrow band method can be useful to estimate an upper bound for the rate of fatigue damage estimations. The single-moment method provided the most non-conservative results among the methods for all sections along the bridge girder. Wirching and Light, Tovo and Benasciutti, Dirlik and $\alpha_{0.75}$ gave acceptable estimations within an absolute error around 10% for detail $D1$ and $D2$. The method proposed by Wirching and Light provided accurate estimations for the Langenuen bridge but was inconsistent due to unpredictable volatility in the shear frame analyses.

Overall, Dirlik along with Tovo and Benascutti gave the best estimated rate of fatigue damage accumulation for the analyses of the shear frames. These two methods were also among the most consistent on the stress spectrums from the Langenuen bridge. However, due to the unpredictable non-conservative results, they should be used with care.

7.1 Further Work

Fatigue damage due to buffeting wind loading is a field of research that becomes more important when more complex structures arise. Building upon this thesis, the following topics might be interesting for further work.

- Expand the analysis to include more than two variables (U and σ_u). E.g. add σ_w, A_u, A_w, K_u and K_w for a more realistic wind field.
- Include a probability distribution for the wind direction on the bridge.
- Implement other closed-form methods to estimate the fatigue damage. E.g. the method proposed by Z. Gao and T. Moan which utilize a trimodal spectral formulation and a two-slope SN-curve or the method proposed by Zhao-Baker.
- More detailed modeling of the cross section of the suspension bridge in Abaqus. E.g. a shell model of the girder.
- Include fatigue damage due to traffic load in the calculations of the fatigue damage at the bridge. The fatigue damage can be studied independently and in combination with buffeting wind loading.
- Propose a new closed-form method based on realistic stress-spectrums from the suspension bridge.

Bibliography

[1] *The E39 Coastal Highway Route*, 2020. [Online]. Available: https://www.vegvesen.no/en/roads/Roads+and+bridges/Road+projects/e39coastalhighwayroute (visited on 26/04/2021).

[2] *Aluminiumbru over langenuen kan bli en realitet*, 2019. [Online]. Available: https://www.vegvesen.no/vegprosjekter/ferjefriE39/nyhetsarkiv/aluminiumbru-over-langenuen-kan-bli-en-realitet (visited on 26/04/2021).

[3] M. V. Dombu and M. Gjelstad, 'Parametric modelling of a suspension bridge with an aluminium girder,' M.S. thesis, NTNU, 2019.

[4] W. Schütz, 'A history of fatigue,' *Engineering Fracture Mechanics*, vol. 54, no. 2, pp. 263–300, 1996, ISSN: 0013-7944. DOI: https://doi.org/10.1016/0013-7944(95)00178-6.

[5] P. Wirsching, T. Paez and K. Oritz, *Random Vibrations: Theory and Practice*. Springer, 2010, pp. 266–288, ISBN: 9783642136597.

[6] M. Gu, Y. Xu, L. Chen and H. Xiang, 'Fatigue life estimation of steel girder of yangpu cable-stayed bridge due to buffeting,' *Journal of Wind Engineering and Industrial Aerodynamics*, vol. 80, no. 3, pp. 383–400, 1999, ISSN: 0167-6105. DOI: https://doi.org/10.1016/S0167-6105(98)00209-8.

[7] A. Naess and T. Moan, *Stochastic Dynamics of Marine Structures*. Cambridge University Press, 2012, ISBN: 9781316089163.

[8] Y. Xu, T. Liu and W. Zhang, 'Buffeting-induced fatigue damage assessment of a long suspension bridge,' *International Journal of Fatigue*, vol. 31, no. 3, pp. 575–586, 2009, ISSN: 0142-1123. DOI: https://doi.org/10.1016/j.ijfatigue.2008.03.031.

[9] I. Lotsberg, *Fatigue Design of Marine Structures*. Cambridge University Press, 2016, ISBN: 78-1-107-12133-1.

[10] J. D. Holmes, *Wind Loading of Structures*. Taylor Francis, 2007, ISBN: 978-0415409469.

[11] D. Benasciutti and R. Tovo, 'Spectral methods for lifetime prediction under wide-band stationary random processes,' *International Journal of Fatigue*, vol. 27, no. 8, pp. 867–877, 2005. DOI: https://doi.org/10.1016/j.ijfatigue.2004.10.007.

[12] G. Jiao and T. Moan, 'Probabilistic analysis of fatigue due to gaussian load processes,' *Probabilistic Engineering Mechanics*, vol. 5, no. 2, pp. 76–83, 1990, ISSN: 0266-8920. DOI: https://doi.org/10.1016/0266-8920(90)90010-H.

[13] T. Dirlik, 'Application of computer in fatigue analysis,' Ph.D. dissertation, University of Warwick, Jan. 1985.

[14] L. Lutes and C. Larsen, 'An improved spectral method for variable amplitude fatigue prediction,' *Journal of Structural Engineering*, vol. 116, pp. 1149–1164, Apr. 1990. DOI: 10.1061/(ASCE)0733-9445(1990)116:4(1149).

[15] T. M. Lystad, A. Fenerci and O. Øiseth, 'Full long-term extreme structural response with sequential gaussian process surrogate modeling,' *Structural Safety*, Submitted for publication.

[16] O. Gramstad, C. Agrell, E. Bitner-Gregersen, B. Guo, E. Ruth and E. Vanem, 'Sequential sampling method using gaussian process regression for estimating extreme structural response,' *Marine Structures*, vol. 72, p. 102 780, 2020, ISSN: 0951-8339. DOI: https://doi.org/10.1016/j.marstruc.2020.102780.

[17] D. K. Bang and E. Ekern, 'Aerodynamic stability of a suspension bridge with an aluminum girder,' M.S. thesis, NTNU, 2020.

[18] Dr.techn. Olav Olsen, '"langenuen suspension bridge-aluminum bridge girder alternative",' no. Revision 0, June 2020.

[19] E. Strømmen, *Theory of Bridge Aerodynamics*. Springer, 2010, ISBN: 9783642136597.

[20] D. E. Newland, *An Introduction to Random Vibrations, Spectral and Wavelet Analysis*. Dover Publications Inc., 2005, ISBN: 9780486442747.

[21] C. Ranieri and G. Fabbrocino, *Operational Modal Analysis*. Springer, 2014, ISBN: 978-1-4939-0766-3.

[22] O. Øiseth, A. Rönnquist and R. Sigbjörnsson, 'Simplified prediction of wind-induced response and stability limit of slender long-span suspension bridges, based on modified quasi-steady theory: A case study,' *Journal of Wind Engineering and Industrial Aerodynamics*, vol. 98, no. 12, pp. 730–741, 2010, ISSN: 0167-6105. DOI: https://doi.org/10.1016/j.jweia.2010.06.009.

[23] S. Ali, S.-M. Lee and C.-M. Jang, 'Statistical analysis of wind characteristics using weibull and rayleigh distributions in deokjeok-do island – incheon, south korea,' *Renewable Energy*, vol. 123, pp. 652–663, 2018, ISSN: 0960-1481. DOI: https://doi.org/10.1016/j.renene.2018.02.087.

[24] Y. Tamura and A. Kareem, *Advanced Structural Wind Engineering*. Springer, 2013, ISBN: 978-4-431-54337-4.

[25] A. Fenerci and O. Øiseth, 'Site-specific data-driven probabilistic wind field modeling for the wind-induced response prediction of cable-supported bridges,' *Journal of Wind Engineering and Industrial Aerodynamics*, vol. 181, pp. 161–179, 2018, ISSN: 0167-6105. DOI: https://doi.org/10.1016/j.jweia.2018.09.002.

[26] The Norwegian Public Roads Administration, *Håndbok N400 - Bruprosjektering*, 2015.

[27] E. Simiu, *Wind effects on structures : fundamentals and applications to design 3rd ed.* Wiley, 1996, ISBN: 0471121576.

[28] C. E. Rasmussen and C. K. I. Williams, *Gaussian Processes for Machine Learning*. Massachusetts Institute of Technology, 2006, ISBN: 026218253X.

[29] *sklearn.gaussian_process.kernels.RBF*, Accessed: 2021-04-12. [Online]. Available: https://scikit-learn.org/stable/modules/generated/sklearn.gaussian_process.kernels.RBF.html?highlight=rbf#sklearn.gaussian_process.kernels.RBF.

[30] *sklearn.gaussian_process.kernels.Matern*, Accessed: 2021-04-12. [Online]. Available: https://scikit-learn.org/stable/modules/generated/sklearn.gaussian_process.kernels.Matern.html?highlight=matern#sklearn.gaussian_process.kernels.Matern.

[31] P. K. Larsen, *Dimensjonering av stålkonstruksjoner*. Fagbokforlaget, 2015, ISBN: 9788251922852.

[32] N. E. Dowling, *Mechanical Behaviorof Materials*. Pearson Education Limited, 2013, pp. 334–866, ISBN: 978-0-273-76455-7.

[33] C. E. Larsen and T. Irvine, 'A review of spectral methods for variable amplitude fatigue prediction and new results,' *Procedia Engineering*, vol. 101, pp. 243–250, 2015, 3rd International Conference on Material and Component Performance under Variable Amplitude Loading, VAL 2015, ISSN: 1877-7058. DOI: https://doi.org/10.1016/j.proeng.2015.02.034.

[34] D. Benasciutti, 'Fatigue analysis of random loadings,' Ph.D. dissertation, University of Ferrara, Italy, Mar. 2004.

[35] L. Lutes, M. Corazao, S.-l. Hu and J. Zimmerman, 'Stochastic fatigue damage accumulation,' *Journal of Structural Engineering*, vol. 110, pp. 2585–2601, Nov. 1984. DOI: 10.1061/(ASCE)0733-9445(1984)110:11(2585).

[36] J. Holmes, 'Fatigue life under along-wind loading — closed-form solutions,' *Engineering Structures*, vol. 24, no. 1, pp. 109–114, 2002, ISSN: 0141-0296. DOI: https://doi.org/10.1016/S0141-0296(01)00073-6.

[37] A. Powell, 'On the fatigue failure of structures due to vibrations excited by random pressure fields,' *The Journal of the Acoustical Society of America*, vol. 30, no. 12, pp. 1130–1135, 1958. DOI: 10.1121/1.1909481. [Online]. Available: https://doi.org/10.1121/1.1909481.

[38] Standard Norge, *NS-EN 1993-1-9:2005+NA:2010, "Eurocode 3: Design of steel structures - Part 1-9: Fatigue design of steel structures*", 2005.

[39] T. M. Lystad, A. Fenerci and O. Øiseth, 'Buffeting response of long-span bridges considering uncertain turbulence parameters using the environmental contour method,' *Engineering Structures*, vol. 213, p. 110 575, 2020, ISSN: 0141-0296. DOI: https://doi.org/10.1016/j.engstruct.2020.110575.

[40] R. E. Melchers and A. T. Beck, *Structural Reliability Analysis and Prediction*, eng. Newark: John Wiley Sons, Incorporated, 2018, ISBN: 1119265991.

[41] *Python Software Foundation.* Python Language Reference, version 3.8.3. Python Softw Found. [Online]. Available: https://www.python.org/.

[42] T. F. Gunnstein. (2021). 'Fatpack.' Version 0.7.0, [Online]. Available: https://github.com/Gunnstein/fatpack (visited on 24/03/2021).

[43] F. Pedregosa, G. Varoquaux, A. Gramfort, V. Michel, B. Thirion, O. Grisel, M. Blondel, P. Prettenhofer, R. Weiss, V. Dubourg, J. Vanderplas, A. Passos, D. Cournapeau, M. Brucher, M. Perrot and E. Duchesnay, 'Scikit-learn: Machine learning in Python,' *Journal of Machine Learning Research*, vol. 12, pp. 2825–2830, 2011.

[44] M. L. Stein, *Interpolation of Spatial Data*. Springer, 1999, ISBN: 978-1-4612-7166-6.

[45] M. Mršnik, J. Slavič and M. Boltežar, 'Frequency-domain methods for a vibration-fatigue-life estimation – application to real data,' *International Journal of Fatigue*, vol. 47, pp. 8–17, 2013, ISSN: 0142-1123. DOI: https://doi.org/10.1016/j.ijfatigue.2012.07.005.

[46] N. Gimsing and T. Christos, *Cable Supported Bridges*. John Wiley Sons, Ltd, 2012, ISBN: 2011024092.

[47] *Simulia. Abaqus Scripting Reference Guide*, Version 6.14. 2014.

[48] Standard Norge, *NS-EN 1999-1-3:2007+NA:2010, "Eurocode 9: Design of aluminium structures - Part 1-3: Structures susceptible to fatigue*", 2010.

[49] F. Campbell, 'Elements of metallurgy and engineering alloys,' Jan. 2008.

[50] The Norwegian Public Roads Administration, *Vurdering og sammenligning av brukonsepter for kryssing av bjørnafjorden: Oppetid*, 25th Apr. 2016. [Online]. Available: https://www.vegvesen.no/_attachment/1623828/binary/1148214?fast_title=Oppetid+brukonsepter+Bj%5C%C3%5C%B8rnafjorden+versjon+1.0.pdf.

[51] C. G. Justus and A. Mikhail, 'Height variation of wind speed and wind distributions statistics,' *Geophysical Research Letters*, vol. 3, no. 5, pp. 261–264, 1976. DOI: https://doi.org/10.1029/GL003i005p00261.

[52] K. Osamu, T. Rikiji and P. Gelder, 'Dynamic response analysis of onshore wind energy power units during earthquakes and wind,' Jan. 2002.

[53] Vegdirektoratet, *NA-rundskriv 2017/09 - Rettelsesblad til håndbok N400 Bruprosjektering*, 2017.

[54] A. G. Davenport, 'The response of slender, line-like structures to a gusty wind,' *Proceedings of the Institution of Civil Engineers*, vol. 23, pp. 389–408, 3 1962.

[55] G. Diana, S. Stoyanoff, K. Aas-Jakobsen,A. Allsop, M. Andersen, T. Argentini, M. C. Montoya, S. Hernández, J. Á. Jurado, H. Katsuchi, I. Kavrakov, H. Kim, G. Larose, A. Larsen, G. Morgenthal, O. Øiseth, S. Omarini, D. Rocch, M. Svendsen and T. Wu, 'Iabse task group 3.1 benchmark results. part 1: Numerical analysis of a two-degree-of-freedom bridge deck section based on analytical aerodynamics,' *Structural Engineering International*, vol. 30, no. 3, pp. 401–410, 2020. DOI: 10.1080/10168664.2019.1639480. eprint: https://doi.org/10.1080/10168664.2019.1639480. [Online]. Available: https://doi.org/10.1080/10168664.2019.1639480.

[56] X. Chen, M. Matsumoto and A. Kareem, 'Aerodynamic coupling effects on flutter and buffeting of bridges,' *Journal of Engineering Mechanics*, vol. 126, no. 1, 2000. DOI: https://doi.org/10.1061/(ASCE)0733-9399(2000)126:1(17).

[57] C. Larsen and L. Lutes, 'Predicting the fatigue life of offshore structures by the single-moment spectral method,' *Probabilistic Engineering Mechanics*, vol. 6, no. 2, pp. 96–108, 1991, ISSN: 0266-8920. DOI: https://doi.org/10.1016/0266-8920(91)90023-W.

[58] A. Halfpenny, 'A frequency domain approach for fatigue life estimation from finite element analysis,' *International Conference on Damage Assessment of Structures (DAMAS 99) Dublin*, 1999.

[59] A. Halfpenny and F. Kihm, 'Rainflow cycle counting and acoustic fatigue analysis techniques for random loading,' *10th International Conference RASD*, Jul. 2010.

[60] A. Niesłony, M. Růžička, J. Papuga, A. Hodr, M. Balda and J. Svoboda, 'Fatigue life prediction for broad-band multiaxial loading with various psd curve shapes,' *International Journal of Fatigue*, vol. 44, pp. 74–88, 2012, ISSN: 0142-1123. DOI: https://doi.org/10.1016/j.ijfatigue.2012.05.014.

[61] V. Bouyssy, S. Naboishikov and R. Rackwitz, 'Comparison of analytical counting methods for gaussian processes,' *Structural Safety*, vol. 12, no. 1, pp. 35–57, 1993, ISSN: 0167-4730. DOI: https://doi.org/10.1016/0167-4730(93)90017-U.

[62] J. Quigley, Y.-L. Lee and L. Wang, 'Review and assessment of frequency-based fatigue damage models,' *SAE International Journal of Materials and Manufacturing*, vol. 9, Apr. 2016. DOI: 10.4271/2016-01-0369.

Appendix A

Shear Frame: Relative Error in Relation to Spectral Bandwidth

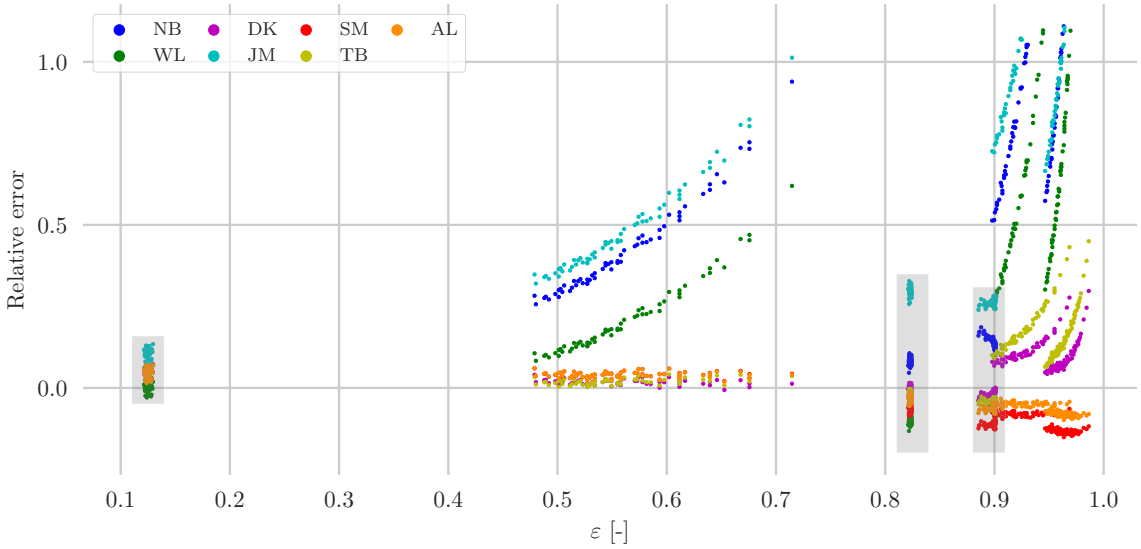

Fig. A.1: Scatter plot of the relative error versus spectral bandwidth for the 95th percentile of points in the training data set for $m = 3$. Gray background highlight analyses excluding background response.

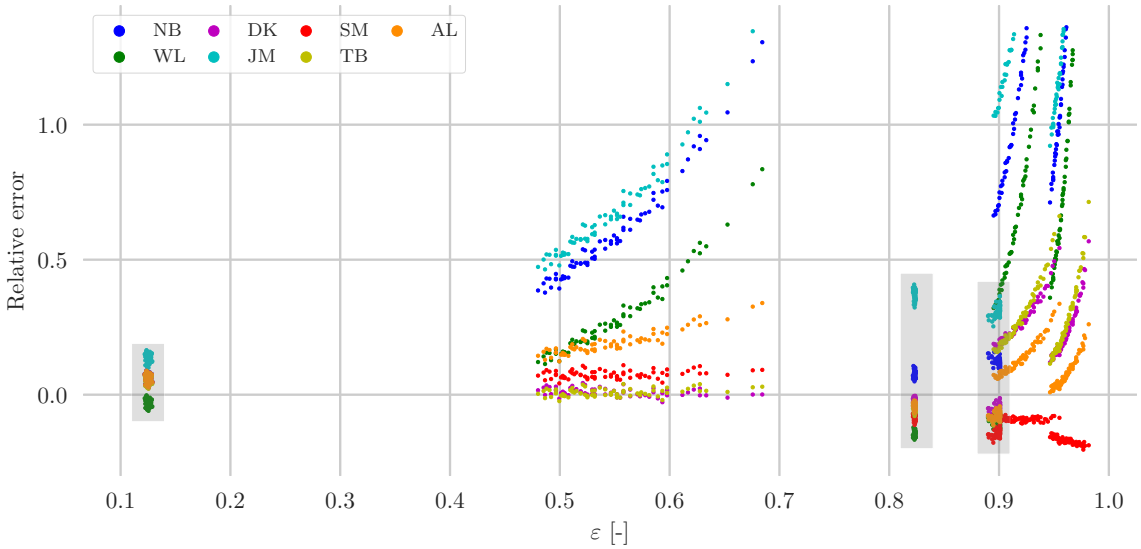

Fig. A.2: Scatter plot of the relative error versus spectral bandwidth for the 95th percentile of points in the training data set for $m = 4$. Gray background highlight analyses excluding background response.

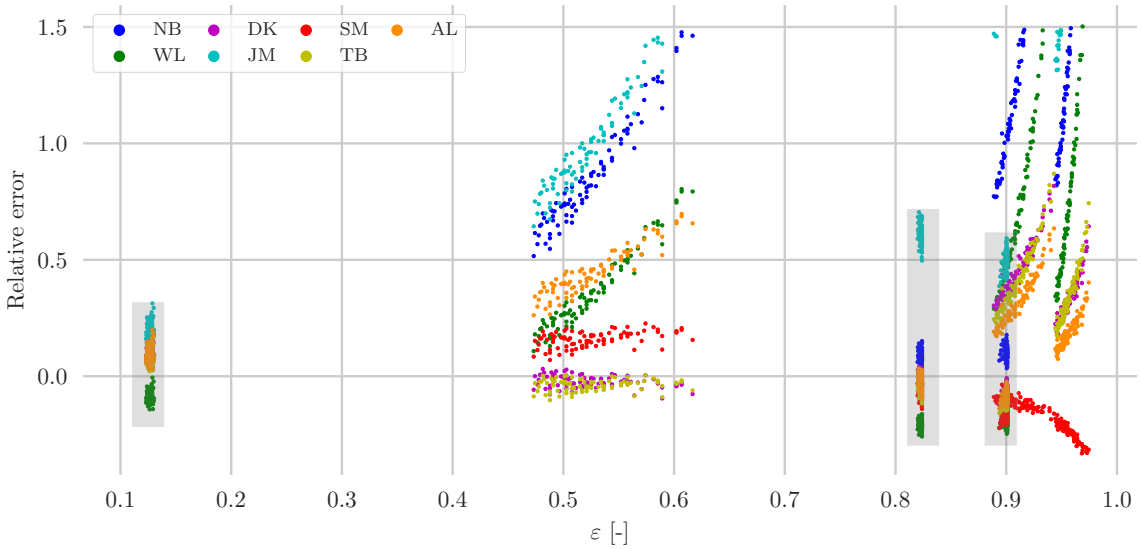

Fig. A.3: Scatter plot of the relative error versus spectral bandwidth for the 95th percentile of points in the training data set for $m = 6$. Gray background highlight analyses excluding background response.

Appendix B

Langenuen Bridge: Selected Modes

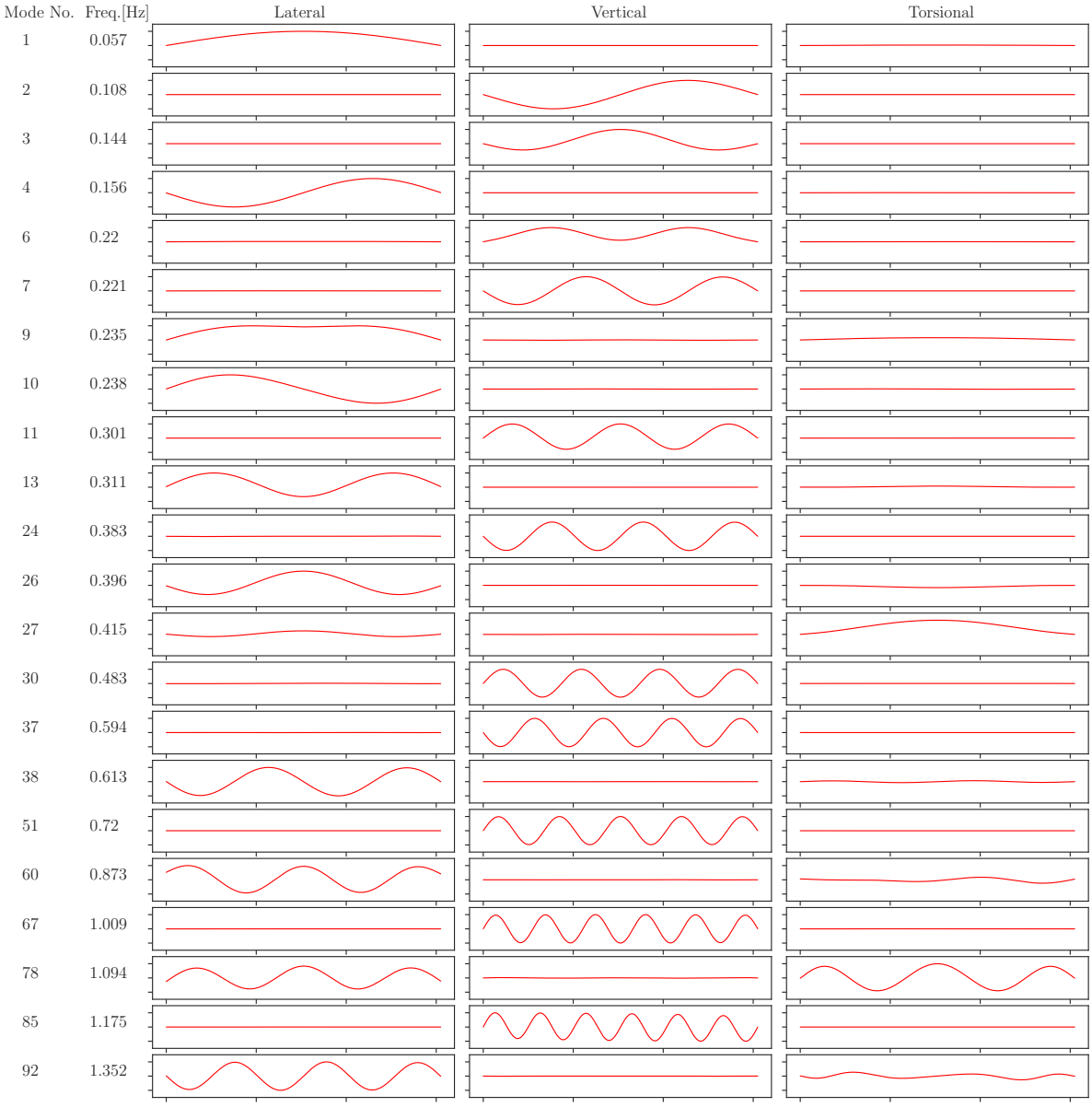

Fig. B.1: Displacement modes from Langenuen Bridge.

Appendix C

Langenuen Bridge: Stress Spectrums

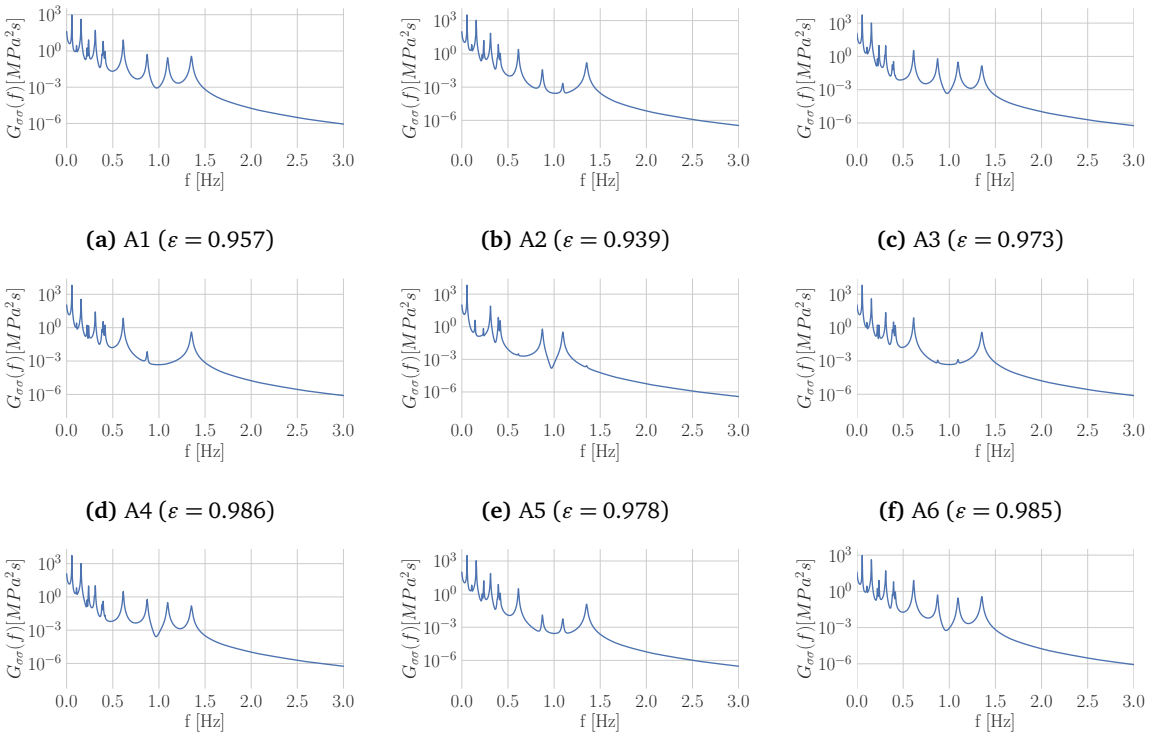

(a) A1 ($\varepsilon = 0.957$) **(b)** A2 ($\varepsilon = 0.939$) **(c)** A3 ($\varepsilon = 0.973$)

(d) A4 ($\varepsilon = 0.986$) **(e)** A5 ($\varepsilon = 0.978$) **(f)** A6 ($\varepsilon = 0.985$)

(g) A7 ($\varepsilon = 0.973$) **(h)** A8 ($\varepsilon = 0.932$) **(i)** A9 ($\varepsilon = 0.958$)

Fig. C.1: Stress spectrums along the bridge girder for detail $D1$ with a mean wind $U = 16.0m/s$ and standard deviation of the turbulence $\sigma_u = 3.00m/s$.

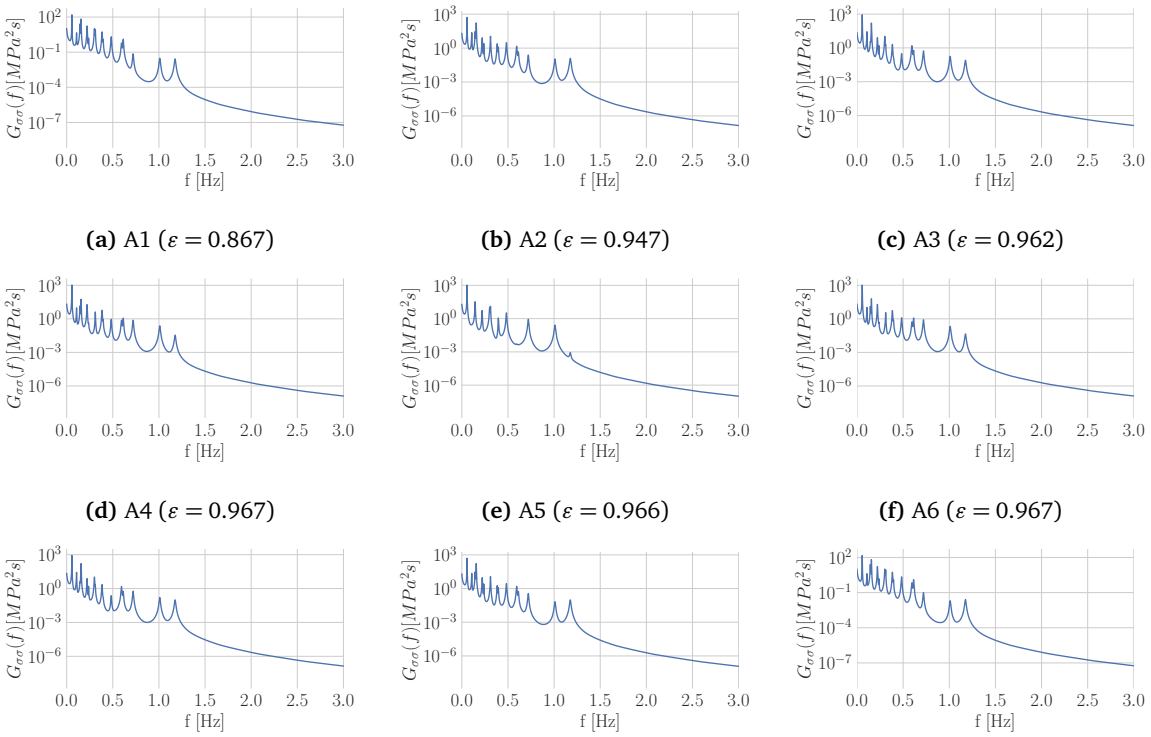

(a) A1 ($\varepsilon = 0.867$) **(b)** A2 ($\varepsilon = 0.947$) **(c)** A3 ($\varepsilon = 0.962$)

(d) A4 ($\varepsilon = 0.967$) **(e)** A5 ($\varepsilon = 0.966$) **(f)** A6 ($\varepsilon = 0.967$)

(g) A7 ($\varepsilon = 0.962$) **(h)** A8 ($\varepsilon = 0.942$) **(i)** A9 ($\varepsilon = 0.863$)

Fig. C.2: Stress spectrums along the bridge girder for detail $D2$ with a mean wind $U = 16.0m/s$ and standard deviation of the turbulence $\sigma_u = 3.00m/s$.

Appendix D

Langenuen Bridge: Fatigue Damage D2

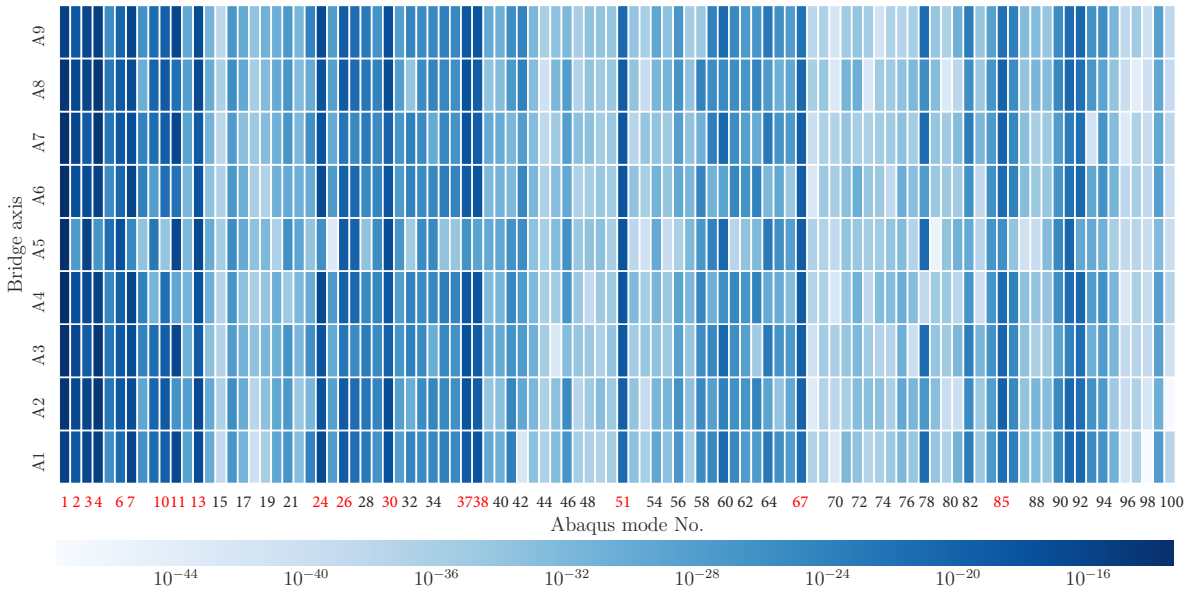

Fig. D.1: Fatigue contribution for detail $D2$ from mode 1 - 100. Mode numbers with red highlighting exceed the fatigue damage criterion of 10^{-20}.

Appendix E

Langenuen Bridge: Fatigue Life

Bridge axis	RF_{tri}	RF	NB	WL	DK	JM	SM	TB	AL
A1	2249	1224	940	1257	1323	694	166	1338	1385
A2	223	110	92	122	112	73	136	115	120
A3	150	61	53	71	67	37	78	67	68
A4	173	75	60	81	84	36	96	82	81
A5	212	93	78	105	107	46	122	106	104
A6	161	77	60	80	82	36	94	81	80
A7	145	63	53	71	67	37	78	67	69
A8	248	118	97	130	120	78	146	123	128
A9	2489	1376	1024	1369	1445	754	1817	1460	1512

Table E.1: Fatigue life for detail $D1$ in years. RF_{tri} and RF correspond to trilinear and fitted linear SN-curve described in Section 6.3.2.

Bridge axis	RF_{tri}	RF	NB	WL	DK	JM	SM	TB	AL
A1	INF	38854	29642	39639	38393	24790	46289	40340	40127
A2	16795	7728	5912	7906	8024	4428	9940	8174	8411
A3	10264	5004	3960	5296	5586	2637	6837	5619	5737
A4	11475	5837	4248	5680	6564	2576	7987	6541	6565
A5	13366	6664	4961	6634	7800	2959	9476	7774	7781
A6	11530	5545	4190	5603	6450	2548	7851	6430	6458
A7	10161	5152	3954	5287	5581	2634	6834	5611	5731
A8	17871	8094	6243	8349	8429	4741	10430	8614	8847
A9	INF	40584	31235	41769	40627	26166	48855	42727	42336

Table E.2: Fatigue life for detail $D2$ in years. RF_{tri} and RF correspond to trilinear and fitted linear SN-curve described in Section 6.3.2.

Estimation of Fatigue Damage due to Buffeting of Suspension Bridges

NTNU

Kunnskap for en bedre verden